

# **DAMAGE MECHANISMS IN HIGH CYCLE FATIGUE**

By  
**David L. Davidson**

**AFOSR FINAL REPORT  
SwRI Project No. 18-8243**

**January 1999**

**19990209 078**

**This research was sponsored by the Air Force Office of Scientific Research  
Electronic and Materials Sciences Directorate  
Under Contract F49620-96-C-0037  
Approved for release; distribution unlimited**



**SOUTHWEST RESEARCH INSTITUTE**  
**SAN ANTONIO**  
**DETROIT**  
**HOUSTON**  
**WASHINGTON, DC**

REPORT DOCUMENTATION PAGE				Form Approved OMB No. 0704-0188	
Public reporting burden for this collection of information is estimated to average 1 hour per response, including the time for reviewing instructions, searching existing data sources, gathering and maintaining the data needed, and completing and reviewing the collection of information. Send comments regarding this burden estimate or any other aspect of this collection of information, including suggestions for reducing this burden, to Washington Headquarters Services, Directorate for Information Operations and Reports, 1215 Jefferson Davis Highway, Suite 1204, Arlington, VA 22202-4302, and to the Office of Management and Budget, Paperwork Reduction Project (0704-0188), Washington, DC 20503.					
1. AGENCY USE ONLY (Leave Blank)		2. REPORT DATE January 29, 1998		3. REPORT TYPE AND DATES COVERED FINAL REPORT — 07/15/96 through 01/31/99	
4. TITLE AND SUBTITLE MECHANISM OF HIGH CYCLE FATIGUE				5. FUNDING NUMBERS F49620-96-C-0037	
6. AUTHOR(S) DAVID L. DAVIDSON					
7. PERFORMING ORGANIZATION NAME(S) AND ADDRESS(ES) SOUTHWEST RESEARCH INSTITUTE 6220 CULEBRA ROAD SAN ANTONIO, TEXAS 78238				8. PERFORMING ORGANIZATION REPORT NUMBER 18-8243 (FORMERLY 06-8243)	
9. SPONSORING/MONITORING AGENCY NAME(S) AND ADDRESS(ES) AFOSR 801 N Randolph Street Mail Room 732 Arlington, VA 22203-1977				10. SPONSORING/MONITORING AGENCY REPORT NUMBER F49620-96-C-0037	
11. SUPPLEMENTARY NOTES					
12a. DISTRIBUTION/AVAILABILITY STATEMENT  APPROVED FOR PUBLIC RELEASE; DISTRIBUTION IS UNLIMITED				12b. DISTRIBUTION CODE	
13. ABSTRACT (Maximum 200 words)  This program was designed to allow interaction between MURI investigators and Southwest Research Institute and to allow SwRI to perform independent research on high cycle fatigue mechanisms. The program goals were met. Two students performed experiments with the SwRI micromechanics facilities. Four manuscripts for publication are included in this report from the independent research effort. The results show (1) that fretting fatigue in the blade-disk attachment is a very difficult damage mechanism to understand and predict, (2) the HCF/LCF interaction has a small effect on fatigue crack growth, and (3) there is still much to be learned about how microstructural variations affect fatigue crack growth mechanisms through Ti-6Al-4V. However, considerable progress was made in this program towards understanding the disk-blade attachment problem.					
14. SUBJECT TERMS				15. NUMBER OF PAGES	
				16. PRICE CODE	
17. SECURITY CLASSIFICATION OF REPORT UNCLASSIFIED	18. SECURITY CLASSIFICATION OF THIS PAGE UNCLASSIFIED	19. SECURITY CLASSIFICATION UNCLASSIFIED	20. LIMITATION OF ABSTRACT  UL		

0 3 FEB 1999

# DAMAGE MECHANISMS IN HIGH CYCLE FATIGUE

By

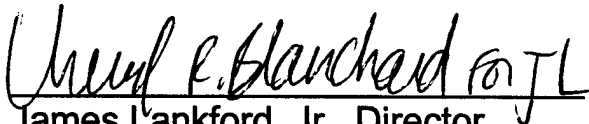
David L. Davidson

AFOSR FINAL REPORT  
SwRI Project No. 18-8243

JANUARY 1999

This research was sponsored by the Air Force Office of Scientific Research  
Electronic and materials Sciences Directorate  
Under Contract F49620-96-C-0037  
Approved for release; distribution unlimited

APPROVED:

  
James Lankford, Jr., Director  
Materials Engineering Department



**SOUTHWEST RESEARCH INSTITUTE**  
SAN ANTONIO HOUSTON  
DETROIT WASHINGTON

DTIC QUALITY INSPECTED 2

# **THE MECHANISMS OF HIGH CYCLE FATIGUE**

## **EXECUTIVE SUMMARY**

This program was designed to achieve several goals: (1) allow access by Multi University Research Initiative (MURI) investigators to the Southwest Research Institute (SwRI) micromechanics research facilities, (2) allow SwRI to perform independent research on high cycle fatigue issues, and (3) to interface with both the MURI and Industry programs on high cycle fatigue.

All the program goals were met. MURI student investigators spent time conducting experiments with the SwRI equipment. The SwRI principal investigator attended MURI meetings and presented results of the independent research program. Significant contact and coordination was maintained with the Industry program.

Results from the SwRI independent research effort were divided into three categories related to: (1) fretting fatigue, (2) fatigue crack growth under high cycle conditions (HCF) with and without the imposition unloading cycles (LCF), and (3) foreign object damage. Four manuscripts for publication have been produced, and are presented in this Final Report, that are related to all but the foreign object damage state.

The results showed (1) that fretting fatigue in the blade-disk attachment is a very difficult damage mechanism to understand and predict, (2) the HCF/LCF interaction has a small effect on fatigue crack growth, and (3) there is still a lot to be learned about the fundamentals of fatigue crack growth through Ti-6Al-4V in vacuum and in air, and the effect of microstructural variations on growth mechanisms.

Note especially the progress made in this program towards understanding the disk-blade attachment problem. A mechanical engineering analysis is presented for determining the loads on the disk caused by engine speed changes and blade resonance conditions. Results are presented for the use of a theoretical model developed at MIT to examine the conditions for growth of a crack found in a fan disk obtained from Kelly Air Force Base. Both are examples of research complementary to that performed under the MURI or the Industry programs that may lead to advances in analysis of the attachment fretting problems.

# **Table of Contents**

## **Executive Summary**

## **Program Overview**

## **Interaction with MURI Program**

Introduction

Summaries of Student Visits to the SwRI Micromechanics Laboratory

Josh Campbell, University of California at Berkeley

Santos Padula, Michigan Technological University

## **SwRI Independent Research Program**

Introduction

Materials Evaluated

Experimental Procedures

## **Results**

Introduction

Growth, Micromechanics, and Fractography of Fatigue Cracks in  
Ti-6Al-4V cycled at 1.5 kHz in Air and Vacuum at Ambient Temperature

Fatigue Crack growth at High R-Ratio in Ti-6Al-4V at 1.5 kHz:  
The Effect of Periodic Removal of Mean Stress

Fatigue Crack Growth in an Aeroengine Disk due to Blade Attachment

Analysis of the Forces in the Disk-Blade Attachment of a Gas Turbine  
Aeroengine

Foreign Object Damage

## **Conclusions**

## **Appendix**

## PROGRAM OVERVIEW

This program was initiated because of inquiries from university investigators who ask SwRI about the feasibility of collaborating on a proposal to the Air Force Multi University Research Initiative on High Cycle Fatigue. Since SwRI was precluded from being funded under this initiative by law, a separate proposal was written for funding so that SwRI could work with the universities.

The objectives of the SwRI program, as stated in the proposal, were:

(1) Work with MURI participating investigators to (a) provide access to the SwRI high frequency cyclic stage for the SEM and displacement measuring equipment (DISMAP), especially to students, and (b) to provide technique development and information on the initiation and growth of fatigue cracks under HCF conditions;

(2) perform research on the growth of cracks under the damage states defined as being relevant to gas turbine engines;

(3) transfer information from the MURI to the Industry program, and from the Industry program to the MURI, as it seemed useful and feasible.

The proposal to AFOSR was written in the autumn of 1995. The program was funded to start in May 1996, to end in May 1998, but extended to Jan. 1999, for better interaction with MURI. The MURI and Industry HCF programs were not initiated until the autumn of 1997, and material was not available through the Industry HCF program until February, 1998.

This program was conducted approximately as envisioned in the proposal. Initial work did not begin as soon as was planned due to technical problems encountered in development of the high frequency SEM stage, but a considerable volume of the research that was planned was conducted. This program was able to assist in providing useful interaction between the Industry Program, with its emphasis on testing, and the MURI, with its emphasis on experimentation and scientific understanding.

# **INTERACTIONS WITH THE MURI PROGRAM**

## **Introduction**

### **Summaries of Student Visits to SwRI Micromechanics Laboratory**

## **INTERACTIONS WITH the MURI PROGRAM**

### **Introduction**

Experimental technique, experimental results, and progress on analyses of HCF problems were shared between SwRI, the MURI program manager, and individual participants. Communications were handled through US mail, e-mail, participation in MURI meetings, and visits by MURI personnel to SwRI. Presentations of results from HCF investigations were made at three conferences by the Principal Investigator.

Much of the information that was shared during the program involved experimental techniques and methods for studying phenomena related to HCF, as well as results from specific experiments. Collaboration on publication of results will be made as is feasible, both with MURI and Industry program investigators.

**Fretting** - As part of trying to understand the fretting problem, several third stage disks from F-100 engines that had experienced disk cracking problems were obtained from Kelly AFB. Under the Industry HCF program, disk-blade attachment surfaces were examined, and several cracks were found. One disk was sectioned metallographically and examined in detail. An analysis of this failure was made using the model of Giannakopoulos, et al., that was done under the MURI program. In one disk obtained from Kelly, several cracked lugs were found and those were sent to Profs. Ritchie at U.C. Berkeley and Milligan at Michigan Tech. for fractographic analysis. One of these specimens was returned to SwRI where additional analysis was performed.

**Students** - One student from the University of California, Berkeley and one student from Michigan Technological University each spent 10 days at SwRI working with our SEM 1.5 KHz loading stage and DISMAP system.

**Meetings** - The Principal Investigator participated in 3 meetings organized by the MURI Program Manager and made presentations in each. Presentations were also made in two symposia on high cycle fatigue at meetings of The Metallurgical Society.



## SUMMARY OF WORK IN THE MICROMECHANICS LABORATORY AT SOUTHWEST RESEARCH INSTITUTE

J. P. Campbell and R.O. Ritchie  
Department of Materials Science and Mineral Engineering  
University of California at Berkeley

### INTRODUCTION

Whereas the bimodal, solution treated and overaged (STOA) microstructural condition has been the focus of the PRDA V program, the MURI, and the high-cycle fatigue program at Southwest Research Institute, a second set of testing has been performed on  $\beta$ -annealed, fully lamellar Ti-6Al-4V in order to investigate the role of microstructure. This microstructural condition was chosen because it is recognized as a viable alternative to the bimodal material for turbine engine components. The fully lamellar microstructure is generally accepted to have better fatigue-crack growth resistance than bimodal structures when large, through-thickness fatigue cracks are cyclically loaded at low mean stress [1,2], e.g., a load ratio of 0.1. However, as the following results illustrate, the fully lamellar microstructure may in fact have inferior fatigue-crack propagation resistance under conditions considered to be more representative of turbine engine high-cycle fatigue, i.e., for small semi-elliptical surface cracks subjected to high mean stresses. Moreover, for the fully lamellar Ti-6Al-4V, a marked sensitivity of fatigue-crack growth rates to the local (near-tip) microstructure makes this microstructural condition highly susceptible to small-crack effects, which could further reduce the fatigue-crack growth resistance.

### MATERIALS AND EXPERIMENTAL METHODS

The  $\beta$ -annealed material, referred to hereafter as the fully lamellar microstructure (**Fig. 1**), was produced by heat treating bimodal Ti-6Al-4V. This starting material is from the same set of forgings used by both the MURI and PRDA V high-cycle fatigue programs (specifically, material was taken from forging 138). Samples were heated to 1005 °C and held for 10 minutes in vacuum ( $\approx 5 \times 10^{-5}$  torr). The samples were then quenched by backfilling the furnace with helium to 40 kPa positive pressure. In this manner, initial cooling rates of  $\sim 100$  °C per minute were achieved. Subsequently, a stabilization treatment was performed at 700 °C for 2 hrs in vacuo followed by a slow furnace cool. The resulting  $\alpha + \beta$

microstructure was fully lamellar, with a colony size of 502  $\mu\text{m}$ ; the center-to-center spacing of the laths was 0.8  $\mu\text{m}$ .

From the heat-treated material, specimens for the SwRI 1.5 kHz fatigue machine were machined, polished, and ion etched. Prior to fatigue-crack growth testing using the 1.5 kHz stage, fatigue precracks were generated in three-point bending at 5 Hz. To facilitate crack formation in the desired location, notches were cut by EDM in the 12.7 mm side of the gauge section; approximate notch dimensions were 1.5 mm by 0.16 mm on the sample surface and 1.5 mm in depth. Precracking was terminated at an initial full-surface crack length ( $2c$ ) of  $\approx 2$  mm. Samples were then transferred to the 1.5 kHz stage and tested at cyclic frequencies,  $\nu$ , ranging from 1.31 to 1.49 kHz in air and vacuum ( $\approx 1 \times 10^{-6}$  torr). Data corresponding to at least the initial 175  $\mu\text{m}$  of growth was discarded due to possible transient effects resulting from the transition from bending to tension. Fatigue crack growth was monitored by *in situ* microscopic observation of the crack at the mean of the loading cycle. The full surface lengths,  $2c$ , for the cracks investigated in the fully lamellar microstructure ranged from 2.4 to 3.6 mm at  $R = 0.8$  in vacuum, 2.5 to 3.2 mm at  $R = 0.8$  in air, and 2.2 to 2.8 mm at  $R \approx 0.6$  in vacuum. For each loading/environment combination, the crack growth thresholds were measured from crack lengths at the lower end of the reported range. At the termination of the test, samples were monotonically overloaded, and fracture surfaces were observed to determine the final shape of the fatigue crack front. The shape of the initial EDM notch employed led to an average  $a/c$  (crack depth to half-surface length) of 1.31. Using this value of  $a/c$ , stress intensities were computed from the solution for semi-elliptical surface cracks by Newman and Raju [3].

## RESULTS AND DISCUSSION

### *Fatigue-crack growth behavior in bimodal and fully lamellar microstructures*

Fatigue-crack growth behavior for the fully lamellar microstructure in air and vacuum at  $R = 0.8$  is compared in Fig. 2 with data previously reported in ref. [4]) for the bimodal Ti-6Al-4V, where the average crack growth increment per cycle,  $da/dN$ , is plotted as a function of the applied stress intensity range,  $\Delta K$ . Reported growth rates are based on the total amount of crack extension measured at both tips of the surface flaw. Actual data are present in **Fig. 2(a)**, and to assist visualization of the relevant trends, scatterbands which envelope some data sets are shown in **Fig.**

**2(b).** The data collected using the 1.5 kHz SEM loading stage shows considerable scatter. This scatter can be attributed in part to the techniques employed for monitoring crack growth. Crack length measurements were made at the sample surface and at approximately one million cycle intervals. Due to the low crack growth rates investigated, crack extension increments as low as 1-2  $\mu\text{m}$  were sometimes observed. Thus, the fatigue-crack growth rates,  $da/dN$ , were computed over distances comparable to, or significantly smaller than, the characteristic microstructural dimensions. The resulting scatter in crack growth rates at a given  $\Delta K$  likely reflects both the sensitivity of local crack growth resistance to the microstructure directly ahead of the tip and the intermittent nature of local crack growth at near-threshold stress intensity ranges. The influence of local microstructure on crack growth resistance will be discussed in more detail below.

In Figure 2, it is apparent that, in both air and vacuum, the bimodal microstructure exhibits fatigue-crack growth resistance superior to that of the fully lamellar material under simulated turbine engine high-cycle fatigue conditions ( $R = 0.8$ ,  $\nu = 1 - 1.5$  kHz). In vacuum, the fully lamellar microstructure exhibits a lower fatigue-crack growth threshold ( $\Delta K_{TH} = 1.8 \text{ MPa}\sqrt{\text{m}}$ , as compared to  $2.7 \text{ MPa}\sqrt{\text{m}}$  in the bimodal material) and faster growth rates in the Paris regime. In air, the disparity in fatigue-crack growth resistance is reduced; the fully lamellar fatigue-crack growth threshold ( $= 2.1 \text{ MPa}\sqrt{\text{m}}$ ) is slightly lower than that of the bimodal material ( $= 2.5 \text{ MPa}\sqrt{\text{m}}$ ); however, in the Paris regime, the fully lamellar and bimodal data sets appear to merge.

The relative fatigue-crack growth resistance observed for fully lamellar and bimodal microstructures at  $R = 0.8$  is in contrast with previously published results on Ti-6Al-4V [1,2], where, at low load ratios ( $R = 0.1$ ) lamellar microstructures have been reported to have superior large-crack fatigue-crack growth resistance. This disparity in the relative crack growth resistance at low and high  $R$  is not surprising, however, as the superior fatigue-crack growth behavior of titanium alloys in the lamellar microstructure at low  $R$  has been attributed to crack deflection, branching, and microcrack formation [5,6], as well as an associated enhancement of fatigue-crack closure [2]. Given this important role of crack closure in the fatigue-crack growth behavior of coarse lamellar microstructures, one would expect the crack growth resistance to degrade at higher load ratios as crack closure is suppressed. These expectations are consistent with the relative fatigue-crack growth resistance at  $R = 0.8$  of bimodal and fully lamellar Ti-6Al-4V, as shown in Figure 2. Furthermore, fatigue-crack growth tests performed on the lamellar

microstructure in vacuum at  $R = 0.6$  to  $0.62$  (Fig. 3) reveal that the crack growth resistance of the fully lamellar material is improved as the mean stress is decreased, with the value of  $\Delta K_{TH}$  increasing to  $3.5 \text{ MPa}\sqrt{\text{m}}$ . In the Paris regime, however, the fatigue-crack growth rates appear to merge with the  $R = 0.8$  data set. This change in fatigue-crack growth resistance as  $R$  is decreased from  $0.8$  to  $0.6$  is completely consistent with the behavior expected when crack closure is enhanced by decreasing load ratio, i.e., the value of  $\Delta K_{TH}$  is increased but the crack growth behavior in the Paris regime is essentially unchanged.

It is also possible that small-crack effects [7-10]\* play a role in the relatively low crack growth resistance observed in the fully lamellar microstructure. The crack lengths investigated were  $\sim 4$  to  $7$  times the average lamellar colony size ( $\sim 502 \text{ }\mu\text{m}$ ). Given that the crack sizes investigated in the fully lamellar microstructure are comparable to the lamellar colony size, that the local (near-tip) microstructure can lead to significant variations in crack growth rates (as discussed below), and that crack closure levels are believed to be significant for large cracks in such coarse lamellar structures, this material is likely susceptible to a small-crack effect. In such cases, a reduced fatigue-crack growth resistance for small flaws may be attributed to an incompletely developed crack-wake-shielding zone (and hence reduced or insignificant extrinsic crack shielding) and to the ability to preferentially sample weak microstructural paths. However, given the current data, it is not possible to decipher if the relatively low crack growth resistance of the lamellar microstructure at  $R = 0.8$  is solely a result of the high load ratio (which would tend to suppress crack closure, analogous to behavior for small cracks), or if the cracks investigated are in fact "small" and the associated small-crack effect plays a role. Based on fatigue-crack growth data obtained for surface flaws of microstructural dimensions up to  $\sim 1 \text{ mm}$  in length in a bimodal microstructure of  $\text{Ti-5.8Al-4.0Sn-3.5Zr-0.7Nb-0.5Mo-0.35Si-0.05C}$  (IMI 834; primary  $\alpha$  and prior  $\beta$  grain sizes of  $19$  and  $60 \text{ }\mu\text{m}$ , respectively), Dowson et al. [11] report that small-crack growth rates are not effected by load ratio for  $R = 0.1$  to  $0.7$ .

---

\*A small crack effect is characterized by a disparity in growth behavior between cracks which are, respectively, small and large relative to the characteristic microstructural dimensions and/or the equilibrium crack-wake shielding-zone length. Specifically, cracks which are "small" may exhibit lower values of  $\Delta K_{TH}$  and, at a given  $\Delta K$ , grow faster than cracks which are "large."

Extrapolation of this finding to the present results, where a load ratio effect is observed when comparing  $R = 0.8$  and  $0.6$  in vacuum, suggests that the crack sizes investigated cannot be considered small. This extrapolation cannot be considered conclusive, however, as the present study focuses on a fully lamellar microstructure.

Although it is uncertain whether the fatigue-crack growth data presented for the fully lamellar microstructure is influenced by small-crack effects, it is highly unlikely that such effects play a role in the data measured for the bimodal Ti-6Al-4V. While the crack lengths reported above for the fully lamellar material are comparable to those investigated in the bimodal material using the 1.5 kHz SEM stage, this microstructure is considerably finer, with primary alpha grains of only  $\sim 8 \mu\text{m}$  in diameter. In this finer structure, crack lengths of 2 mm or more cannot be considered to be microstructurally small and are not likely small relative to the equilibrium crack-wake shielding-zone length. The bimodal data of Boyce et al. [4] was collected using compact tension samples with through-thickness cracks greater than 5 mm in length.

#### *Microstructure/fatigue crack interactions*

*In-situ* SEM observations of fatigue-crack growth revealed the crack path to be significantly influenced by the local microstructure, with the crack showing a strong tendency to propagate roughly perpendicular to the  $\alpha/\beta$  interfaces of the lamellar structure, as shown in **Fig. 4**. This tendency has been previously noted in lamellar  $\alpha+\beta$  Ti alloys and attributed to a preference for crack growth along slip bands [5,6]. Cracks also exhibited a strong tendency to propagate along lamellar colony boundaries. In addition to strongly influencing the direction of crack propagation, the local microstructure was found to have a profound influence on crack growth rates. This behavior is illustrated in **Fig. 5**, where the data previously presented in Figure 3 is shown along with independent growth rates for each tip of the fatigue crack for two loading intervals at  $R = 0.6$  in vacuum (all other reported crack growth data was computed based on the total increment of growth observed at both tips of the semi-elliptical surface cracks). Consideration of the crack growth resistance at each crack tip independently reveals that, at a given  $\Delta K$ , the local microstructure can lead to differences in crack growth rate of up to three orders of magnitude. Such a disparity in local crack growth resistance would likely result in increased scatter, and perhaps even lower crack growth thresholds, for naturally-initiated small cracks contained within only one or two lamellar colonies.

The preferred crack growth paths (along slip bands and colony boundaries) lead to significant deflections of the crack from the nominal mode I path (where the propagation direction is normal to the maximum tensile stress). Fatigue cracks were often observed to arrest following significant deflection, an example of which is shown in **Fig. 6**, where the mode I orientation of the crack would be vertical on the plane of the page. This sample was cycled at  $R = 0.8$  in vacuum. The crack tip is observed to be deflected along a colony boundary, and in fact, arrested very near a second boundary. This tip remained arrested in the configuration shown for  $1.1 \times 10^7$  cycles at  $\Delta K$  of 1.9 to 2.1 MPa $\sqrt{m}$ . This tip began growing again after switching the test environment to lab air and cycling an additional 690,000 cycles.

Lamellar colony boundaries were also observed to represent significant barriers to crack propagation. In **Fig. 7**, a fatigue crack cycled at  $R = 0.8$  in air is observed near a lamellar colony boundary. This crack remained arrested as shown for 1,288,000 cycles at  $\Delta K$  ranging from 1.9 to 2.1 MPa $\sqrt{m}$ . In Figure 7, a shear band emanates from the crack tip and terminates at the colony boundary. This observation suggests that, in fully lamellar material, colony boundaries slow or terminate crack growth by inhibiting near-tip plastic deformation.

While crack deflection and colony boundaries represent significant barriers to crack propagation in the fully lamellar microstructure, crack arrest was also frequently observed to be associated with crack bifurcation, microcracking, and the formation of uncracked ligaments, an example of which is shown in Figure 4 (the mode I propagation direction is vertical). Figure 4 shows the near-tip region for a sample cycled in vacuum at  $R = 0.6$ . The crack has strongly deflected after crossing a colony boundary in order to achieve the preferred propagation path orthogonal to the  $\alpha/\beta$  interface in the lamellar structure. Multiple cracks have formed, and a microcrack is observed ahead of the main crack tip, separated by an uncracked ligament. This end of the surface crack remained arrested as shown for 17 million cycles at  $\Delta K$  from 3.1 to 4.3 MPa $\sqrt{m}$ . After these 17 million cycles, however, a large secondary crack formed slightly ahead of the furthest microcrack tip in Figure 4. Specifically, at a  $\Delta K$  of 4.3 MPa $\sqrt{m}$  ( $R = 0.6$ ), a 309  $\mu m$  increment of growth occurred during one million loading cycles by the formation of this secondary crack. Based on the sudden appearance of this rather large secondary crack and the fact that it was not completely linked with the main crack shown in Figure 4, it would seem that the fatigue crack, while

arrested at the sample surface for  $1.8 \times 10^7$  cycles, was continuing to propagate subsurface. Under this scenario, the apparent sudden formation of a large secondary crack simply resulted as the subsurface crack reached the sample surface.

The above observations regarding the commencement of crack growth at the sample surface following arrest for  $1.8 \times 10^7$  cycles illustrate a potential pitfall in the definition of crack growth thresholds for semi-elliptical surface flaws in the fully lamellar material. Given the range of local fatigue-crack growth resistance exhibited by this microstructure (Figure 5), and the propensity for crack arrest at colony boundaries or due to crack deflection, crack bifurcation, and uncracked ligament formation, it is very plausible that false thresholds may be measured if the sample is not cycled for a sufficient number of cycles at an arrest condition, particularly if crack length is monitored only at the sample surface. As the arrest condition discussed with reference to Figure 4 illustrates, subsurface crack growth may occur even though the crack appears arrested at the surface for tens of millions of cycles.

#### *The effect of environment on fatigue-crack growth behavior*

In terms of the environmental influence on crack growth in the fully lamellar material, the thresholds for fatigue-crack growth,  $\Delta K_{TH}$ , in air and vacuum are nearly identical ( $\Delta K_{TH} = 2.0$  and  $1.8 \text{ MPa}\sqrt{\text{m}}$ , respectively). However, at  $\Delta K$  above threshold, the fully lamellar crack growth rates are one to two orders of magnitude faster in air. The relative fatigue-crack growth resistance in air and vacuum in the fully lamellar microstructure parallels the trends exhibited by the bimodal material, where thresholds in air and vacuum are nearly identical but growth rates are faster in air for  $\Delta K$  above threshold. It is noteworthy, however, that the disparity in growth rates in air and vacuum in the bimodal Ti-6Al-4V appears to be larger than for the fully lamellar microstructure, with growth rates at a given  $\Delta K$  in the bimodal material being up to three orders of magnitude faster in air than in vacuum.

## CONCLUSIONS

Based on a study of the fatigue-crack growth behavior of semi-elliptical surface flaws in a  $\beta$ -annealed, fully lamellar microstructure of Ti-6Al-4V, and comparison with the results for similar testing of an STOA bimodal microstructure of this same alloy, the following conclusions can be made.

1. Under cyclic loading conditions which simulate turbine engine high-cycle fatigue, i.e., high load ratio ( $R = 0.8$ ) and high cyclic loading frequencies ( $\nu \approx 1.5$  kHz), the fully lamellar material appears to offer inferior fatigue-crack growth resistance relative to the bimodal microstructure. In both air and vacuum, the fully lamellar microstructure exhibits a lower crack growth threshold. Furthermore, in vacuum, Paris-regime growth rates in the fully lamellar material are faster than those in the bimodal microstructure. This conclusion must be qualified, however, by noting that the comparison of bimodal and lamellar thresholds may be a comparison of small crack data (in the fully lamellar microstructure) to large-crack data (in the bimodal material). Based on the current results, it is not clear if the fatigue cracks investigated in the lamellar structure should be considered "small" or "large".

2. At high load ratio ( $R = 0.8$ ) in air, although the crack-growth threshold is lower in the fully lamellar microstructure, the growth rates appear to merge with those of the bimodal material in the Paris regime.

3. Analogous to behavior observed in the bimodal material, in air and vacuum the fully lamellar microstructure exhibits nearly equivalent values of  $\Delta K_{TH}$ , but above threshold, growth rates are faster in air. However, this disparity in growth rates between air and vacuum in the Paris regime is not as large in the fully lamellar Ti-6Al-4V as in the bimodal microstructure.

4. In vacuum, there appears to be a significant influence of load ratio in the fully lamellar microstructure, with the crack growth threshold,  $\Delta K_{TH}$ , increasing from 1.8 MPa $\sqrt{m}$  at  $R = 0.8$  to 3.5 MPa $\sqrt{m}$  at  $R = 0.6$ . However, for these load ratios, crack growth rates appear to merge in the Paris regime.

5. The fatigue crack path in the fully lamellar material is strongly influenced by microstructure, with the crack tending to propagate roughly perpendicular to the alpha laths. This leads to significant deflection as the crack grows from colony to colony. Cracks were also observed to deflect along colony boundaries.

6. Colony boundaries were found to represent formidable barriers to crack propagation, with cracks arresting at or near colony boundaries for up to several million cycles. Cracks were also observed to arrest as a result of deflection, crack bifurcation, and uncracked ligament formation.



## REFERENCES

1. Thompson, A.W., J.C. Williams, J.D. Frandsen, and J.C. Chesnutt, "The effect of microstructure on fatigue crack propagation in Ti-6Al-4V", in *Titanium and Titanium Alloys: Scientific and Technological Aspects*, eds. J.C. Williams and A.F. Belov, Plenum Press, p. 691-703 (1982).
2. Halliday, M.D. and C.J. Beevers, "Non-closure of cracks and fatigue crack growth in  $\beta$  heat treated Ti-6Al-4V", *Int. J. Fract.*, **15**, p. R27-R30 (1979).
3. Newman, J.C. and I.S. Raju, "An empirical stress-intensity factor equation for the surface crack", *Eng. Fract. Mech.*, **15**, p. 185-192 (1981).
4. Boyce, B.L., J.P. Campbell, O. Roder, A.W. Thompson, W.W. Milligan, and R.O. Ritchie, "Thresholds for high-cycle fatigue in a turbine engine Ti-6Al-4V alloys", *International Journal of Fatigue*, in press (1999).
5. Lehr, P., "Microscopic features of fracture and crack propagation of titanium alloys", in *Titanium '80, Proceedings of the Fourth International Conference on Titanium*, eds. H. Kimura and O. Izumi, TMS-AIME, Warrendale, PA, Kyoto, Japan, p. 1617-1626 (1981).
6. Eylon, D. and P.J. Bania, "Fatigue cracking characteristic of b-annealed large colony Ti-11 alloy", *Metall. Trans. A*, **9A**, p. 1273-1279 (1978).
7. Ritchie, R.O. and J. Lankford, "Small fatigue cracks: a statement of the problem and potential solutions", *Material Science and Engineering*, **A84**, p. 11-16 (1986).
8. Suresh, S. and R.O. Ritchie, "Propagation of short fatigue cracks", *Int. Metals Rev.*, **29**, p. 445-476 (1984).
9. Miller, K.J., "The short crack problem", *Fatigue Engng. Mater. Struct.*, **5**, p. 223-232 (1982).
10. Lankford, J., "Influence of microstructure in the growth of small fatigue cracks", *Fatigue Engng. Mater. Struct.*, **8**, p. 161-175 (1985).
11. Dowson, A.L., A.C. Hollis, and C.J. Beevers, "The effect of the alpha-phase volume fraction and stress ratio on the fatigue crack growth characteristics of the near-alpha IMI 834 Ti alloy", *International Journal of Fatigue*, **14**, p. 261-170 (1992).

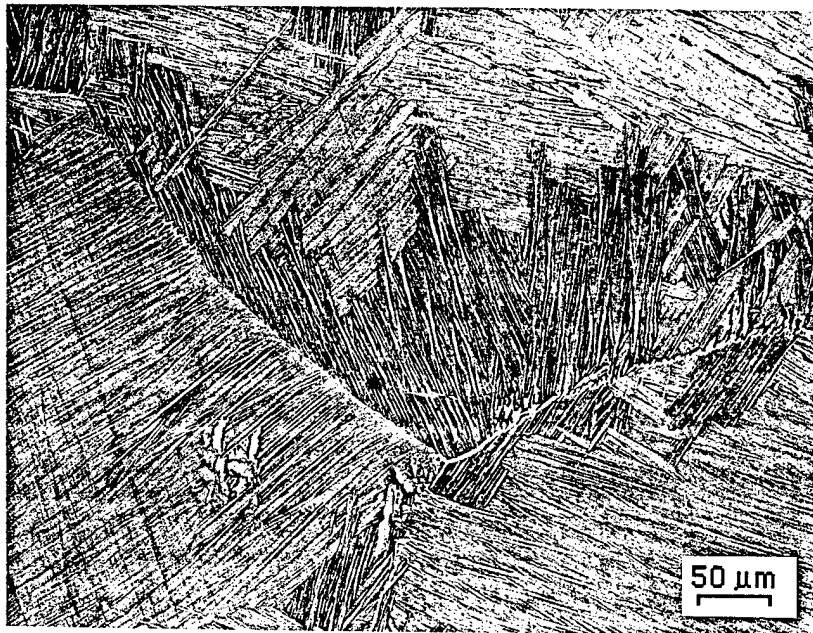


Fig. 1: Optical micrograph of the fully lamellar Ti-6Al-4V.

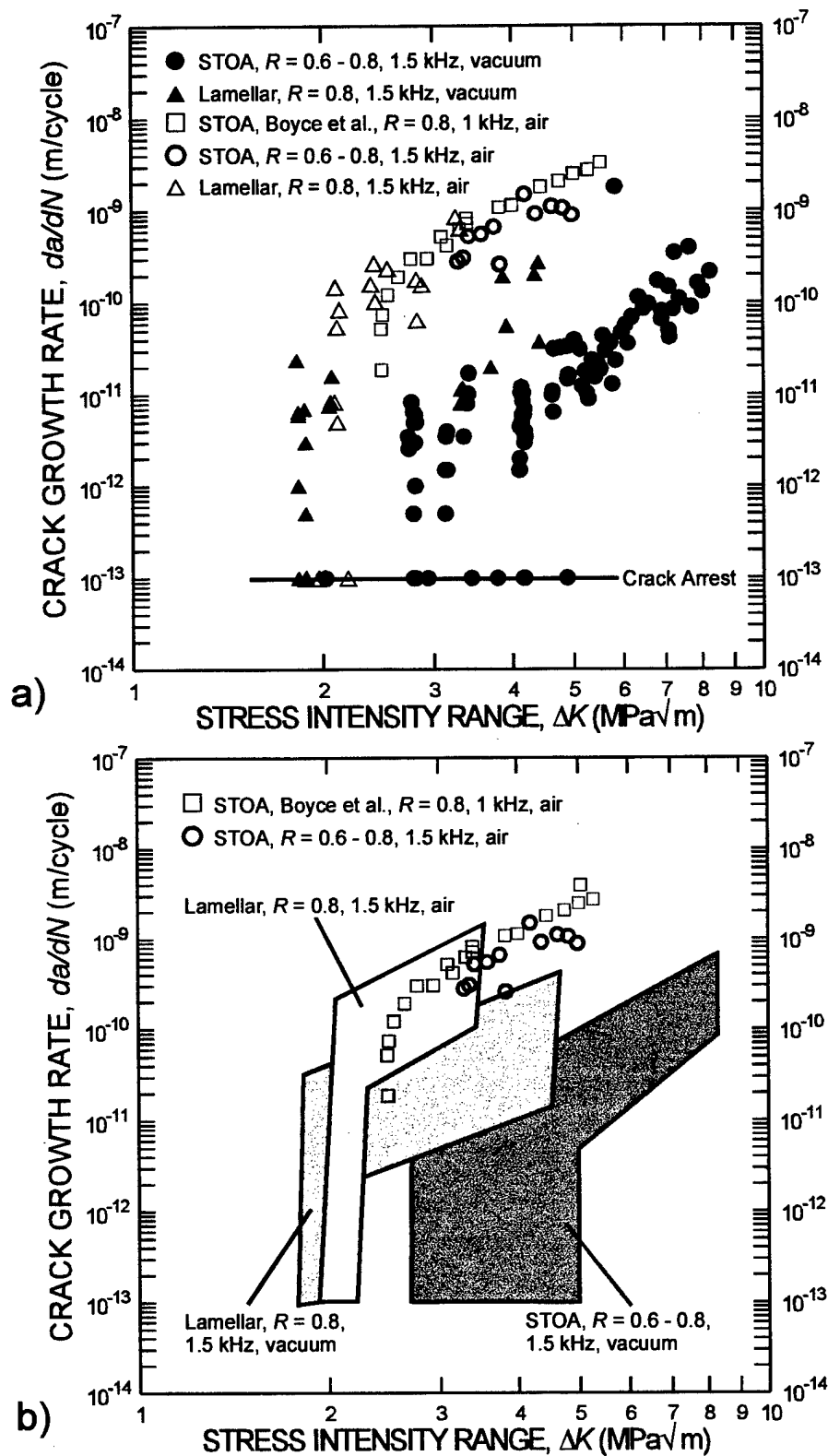


Fig. 2: Fatigue-crack growth rates,  $da/dN$ , as a function of stress intensity range,  $\Delta K$ , are compared for the fully lamellar and bimodal Ti-6Al-4V in vacuum ( $\approx 1 \times 10^{-6}$  torr) and air. (a) Actual data, and (b) envelopes representing the scatter of some data sets.

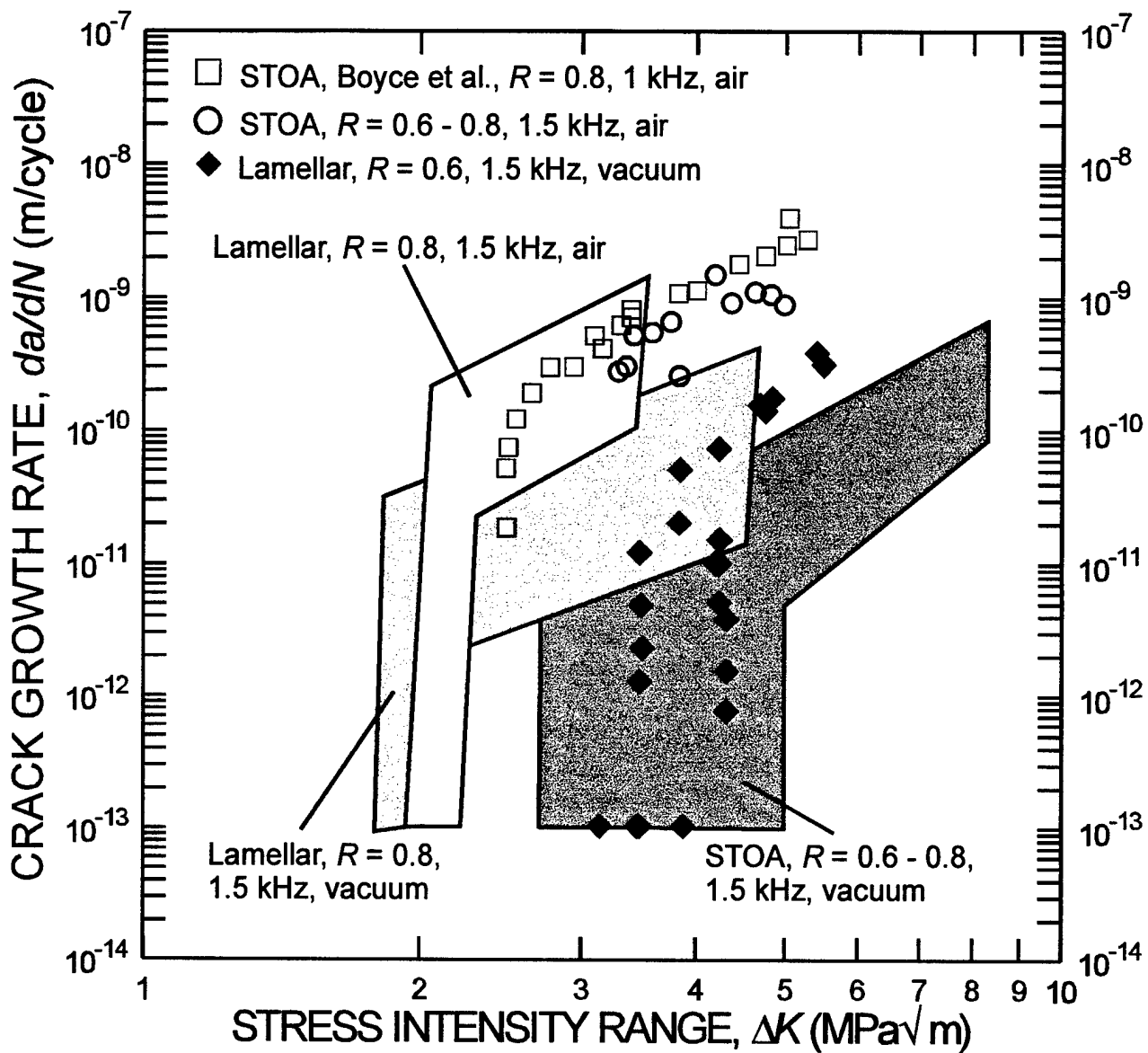


Fig. 3: Fatigue-crack growth rates,  $da/dN$ , as a function of stress intensity range,  $\Delta K$ , for the fully lamellar and bimodal Ti-6Al-4V. Crack growth rates for the fully lamellar microstructure at  $R = 0.6$  to  $0.62$  are compared with the data presented in Figure 2(b).

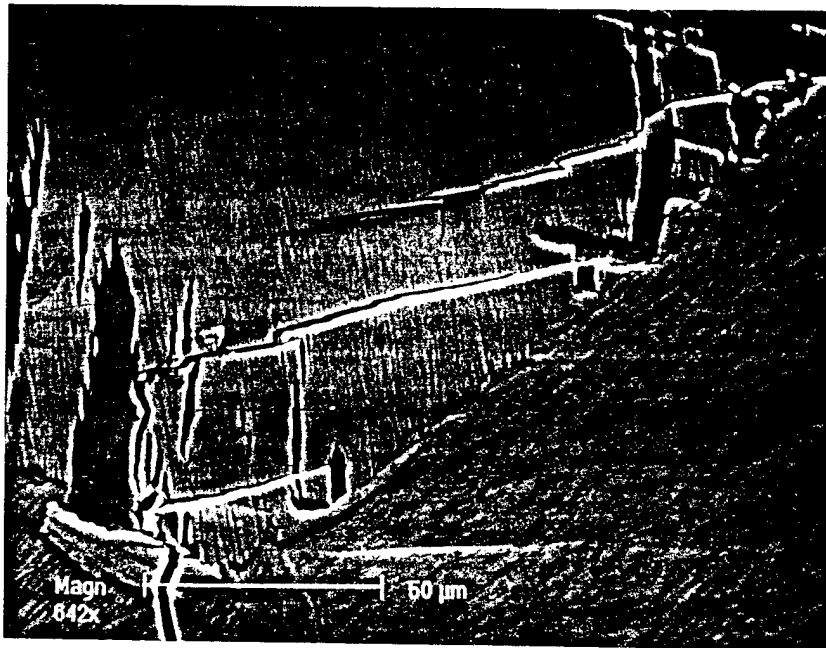


Fig. 4: Scanning electron micrograph of the near-tip region for a fatigue crack in fully lamellar Ti-6Al-4V. Prior cycling was at  $\Delta K = 3.8 \text{ MPa}\sqrt{\text{m}}$ ,  $R = 0.6$  in vacuum. The crack path has deflected significantly from the mode I orientation (vertical on the page) upon crossing a colony boundary. Crack bifurcation and an uncracked ligament are observed. This crack tip remained arrested as shown for 17 million cycles at  $\Delta K$  from 3.1 to 4.3  $\text{MPa}\sqrt{\text{m}}$ .

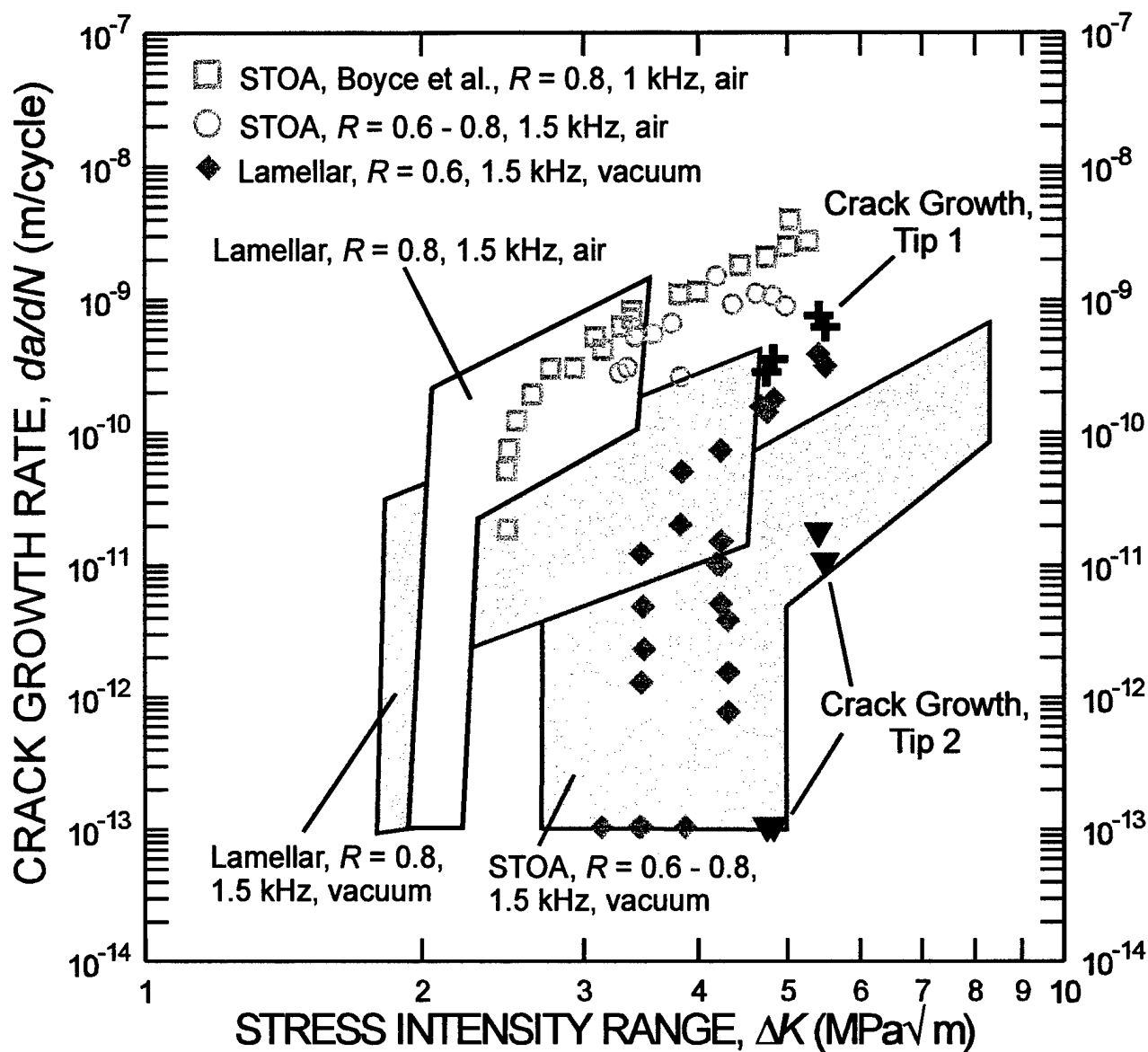


Fig. 5: Fatigue-crack growth rates,  $da/dN$ , as a function of stress intensity range,  $\Delta K$ , for the fully lamellar and bimodal Ti-6Al-4V. Growth rates for each tip of a fatigue crack cycled at  $R = 0.6$  in vacuum are compared with data previously presented in Figure 2(b). A profound influence of local microstructure is observed, with the growth rates at opposite tips of the fatigue crack differing by over three orders of magnitude.

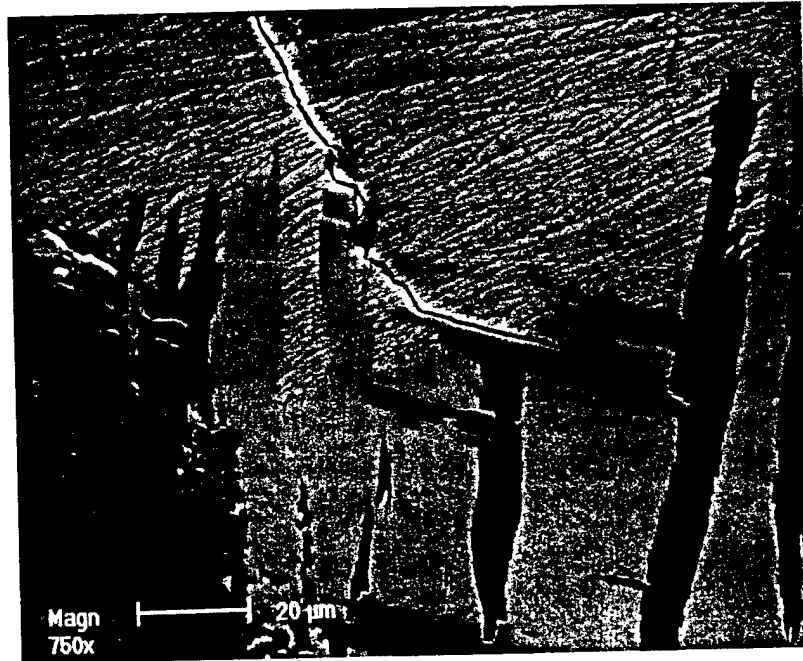


Fig. 6: Scanning electron micrograph showing a crack which, upon encountering a colony boundary, has deflected significantly from the Mode I orientation (vertical on the page). The crack remained arrested in the configuration shown for  $1.1 \times 10^7$  cycles at  $\Delta K$  of 1.9 to 2.1 MPa $\sqrt{m}$ .

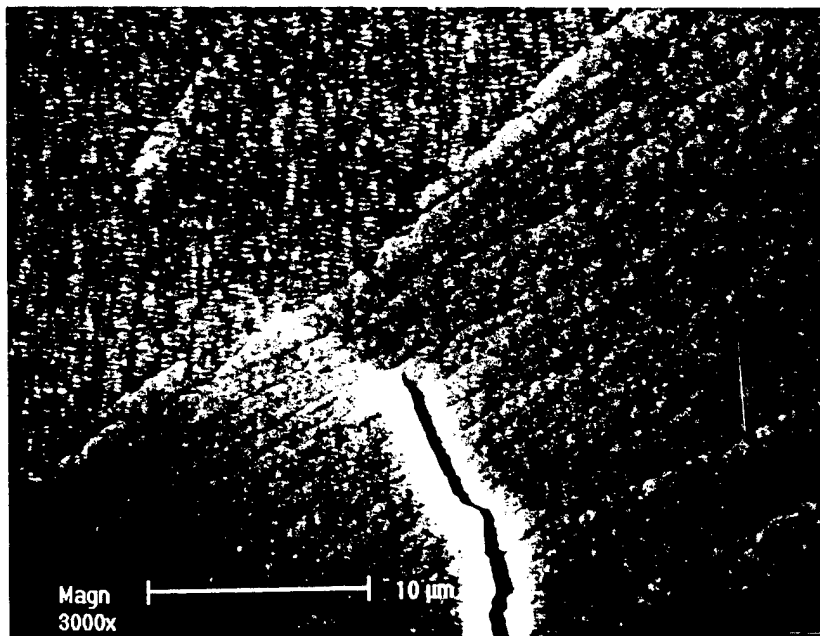


Fig. 7: Scanning electron micrograph showing the tip of a fatigue crack (cycled at  $R = 0.8$  in air) adjacent to a colony boundary. The crack tip remained arrested as shown for  $1.3 \times 10^6$  cycles at  $\Delta K$  ranging from 1.9 to 2.1 MPa $\sqrt{m}$ .

# **SUMMARY OF WORK IN THE MICROMECHANICS LABORATORY AT SOUTHWEST RESEARCH INSTITUTE**

Santos Padula II  
Michigan State University  
Houghton, MI

## **OVERVIEW OF SYSTEM AND WORK**

A number of experiments were intended for the purposes of attaining threshold data for polycrystalline KM4 and single crystal RENE N5. The polycrystalline samples which will be denoted as supersolvus and subsolvus have distinctly differing grain sizes. This difference in grain size is a result of the difference in heat treatment to which the two are subjected. All microstructures consist of  $\gamma'$  precipitates within a  $\gamma$  matrix, the primary difference being the existence of grain boundaries in the polycrystalline samples, as the term implies. Grain size in the polycrystalline specimens is on the order of 50  $\mu\text{m}$  and 6  $\mu\text{m}$  for the supersolvus and subsolvus samples, respectively.

Samples which were provided to SwRI prior to the visit were notched and precracked to an initial flaw size  $\approx 1$  mm.

Threshold studies consisted of running decreasing and increasing  $\Delta K$  tests with a resonant frequency apparatus developed by SwRI research scientists. The high resolution obtained through viewing the crack tip with the scanning electron microscope (SEM) provided ample resolution for measurement of crack extension.

DISMAP (also developed by SwRI research scientists) was also employed to develop strain maps in the vicinity of the crack tip.

## **EXPERIMENTS PERFORMED**

Limited information has been obtained to date on the crack growth behavior of this class of material. Preliminary modeling indicates threshold stress intensities at high R ( $R \approx 0.95$ ) to be in the vicinity of 7.5  $\text{MPa}\sqrt{\text{m}}$  for the polycrystalline KM4. Based on the required specimen geometries and load limitations of the piezoceramic actuators, such a stress intensity was unattainable given the initial flaw sizes. Tests on



the polycrystalline material were therefore run at the maximum stress intensity attainable (5 MPa root meter) for the sole purpose of verifying that this stress intensity was below threshold.

Decreasing  $\Delta K$  and increasing  $\Delta K$  tests were successfully performed on single crystal RENE N5. Data for crack length was collected using measurements made in the SEM. This data was eventually plotted as a function of cycle count whereupon secant method was used to determine the crack growth rate. Photomicrographs were taken at various stages of crack growth in an attempt to learn something about microstructure/crack interaction.

DISMAP was employed at various stages of the test and displacement maps as well as strain maps were generated for regions surrounding the crack tip.

## RESULTS AND DISCUSSION

Threshold data for single crystal RENE N5 preliminarily indicates threshold to be somewhere in the vicinity of 2 MPa $\sqrt{m}$ . Discrepancies between the decreasing  $\Delta K$  and increasing  $\Delta K$  tests are unknown at this time but are believed to be a combination of an underloading effect and possibly a load uncertainty in the system (both of which will be discussed further later). **Fig. 1** shows threshold data for single crystal RENE N5 ( $R = 0.8$ ) obtained at SwRI and subsolvus and supersolvus polycrystalline KM4 ( $R = 0.7$ ) obtained at Michigan Tech in a 1000 Hz servo-hydraulic machine. Of particular interest is the drastic reduction in threshold stress intensity range believed to be associated with the absence of grain boundaries.

Photomicrographs obtained during growth in the single crystal specimen indicate growth along slip bands which extend some 20-30 microns ahead of the crack tip (See **Fig. 2**). Such slip band extension is unlikely in the polycrystalline material due to the existence of the grain boundaries.

Other growth behavior of interest is the apparent crack growth occurring on  $\{100\}$  at low  $\Delta K$ , rather than on  $\{111\}$ . This phenomena coincides with growth behavior observed by Telesman et al. [1] in similar alloys.

Strain maps obtained using DISMAP indicate anisotropic strain distributions around the crack tip which is to be expected. No clear relation between the strain distribution and slip band formation has been obtained as yet.

A preliminary assessment of the plastic zone size was utilized to determine the validity of the measurements. As a first approximation, the standard relationship between plastic zone size, stress intensity and resolved stress was used.

$$2r_p = K^2/(\pi\sigma^2)$$

It is important to note that the plastic zone size estimated is that for the plane stress condition since the data was collected from observations at the free surface. Estimates of the plastic zone size indicate  $2r_p = 43 \mu\text{m}$  and  $2r_p = 25 \mu\text{m}$ , respectively for the conditions shown in Fig. 3. Experimental observations showed slip band extension at the surface some 30-40  $\mu\text{m}$  and 20-30  $\mu\text{m}$  ahead of the crack tip, for the two cases mentioned previously. Experimental observations thus correlate somewhat with isotropic behavior predictions but not with the strain distributions predicted by DISMAP.

#### **POSSIBLE SOURCES OF ERROR IN THRESHOLD MEASUREMENTS**

As was mentioned previously, threshold data obtained for the decreasing  $\Delta K$  portion was not consistent with data obtained for the increasing  $\Delta K$  portion of the crack growth rate curve. Possible sources for this discrepancy may lie in the notion of a large underload effect. Behavior in similar alloys has exhibited signs of crack arrest due to static underloading and long duration cycling below threshold. Data pertaining to the RENE N5 single crystal was obtained over a number of days. Data obtained for the decreasing portion was obtained with minimal time spent in the underloaded condition. Prior to obtaining the increasing  $\Delta K$  data, the sample had been unloaded for a duration of two days.

Other factors which may be suspect are related to the certainty in the loads applied to the specimen. Incipient heating produced thermal drift of the strain signal used to monitor mean load and no peak height analyzer was employed to obtain accurate resolution of load amplitude. Such procedures produce uncertainty in both the stress intensity range and R

ratio for each segment of the test. Thus, the threshold data may not be as anomalous as appears in the figure.

All things being equal, it is believed that the undercooling affect produces the greatest contribution to the scatter observed. This, however, remains to be proved and will most likely be the subject of investigations in the future.

## **REFERENCE**

1. J. Telesman and L.J. Ghosn: NASA TM-100943, June 1988.

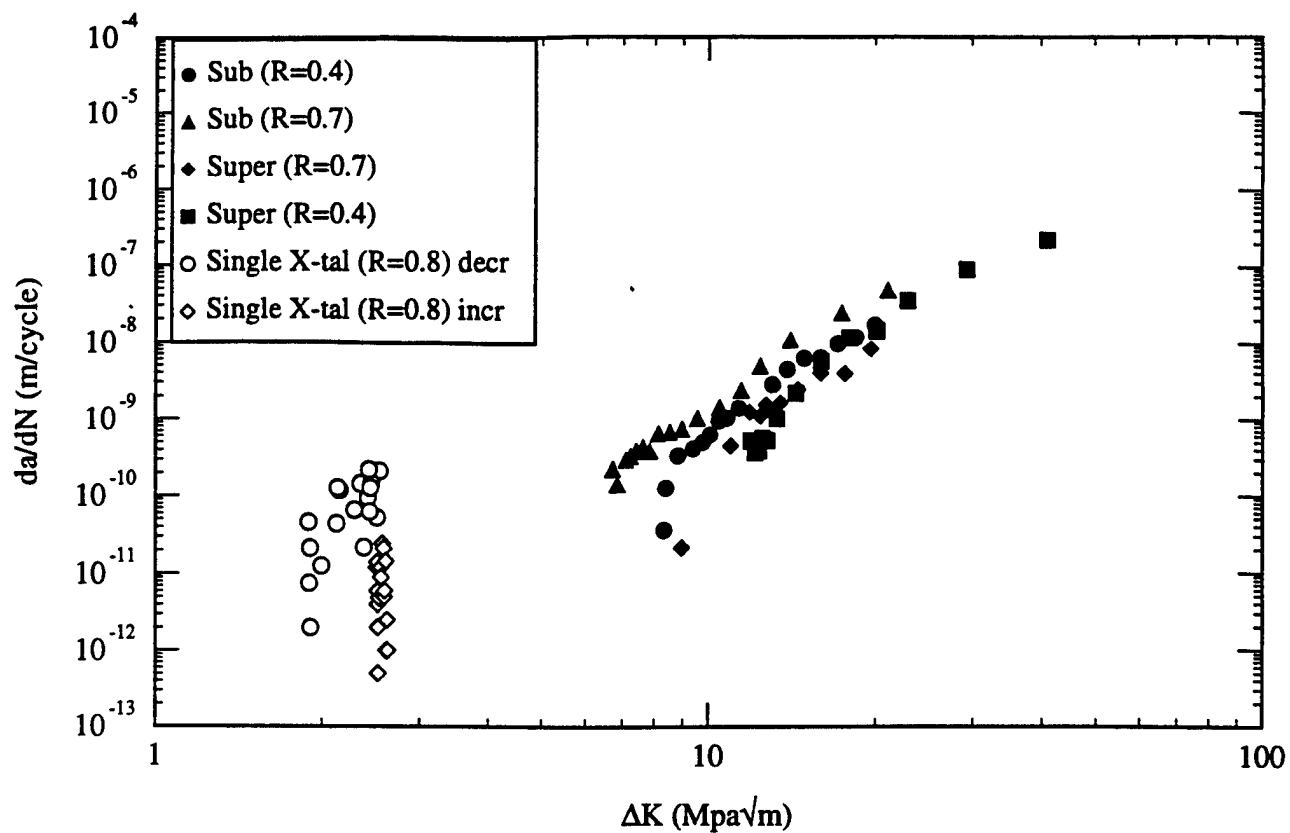


Fig. 1 Crack growth rate data for polycrystalline KM4 and single crystal RENE N5. Reduction in  $\Delta K_{TH}$  appears to be due to R-ratio as well as existence or absence of grain boundaries.

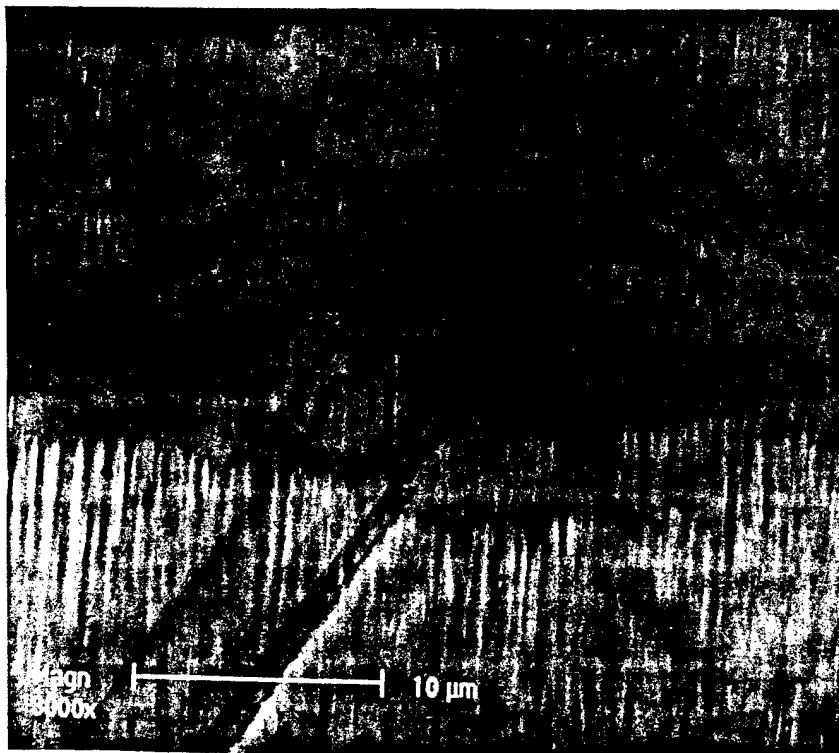


Fig. 2 Crack growth in RENE N5 single crystal. Notice the slip band extension some 20 - 30 μm past the crack tip.

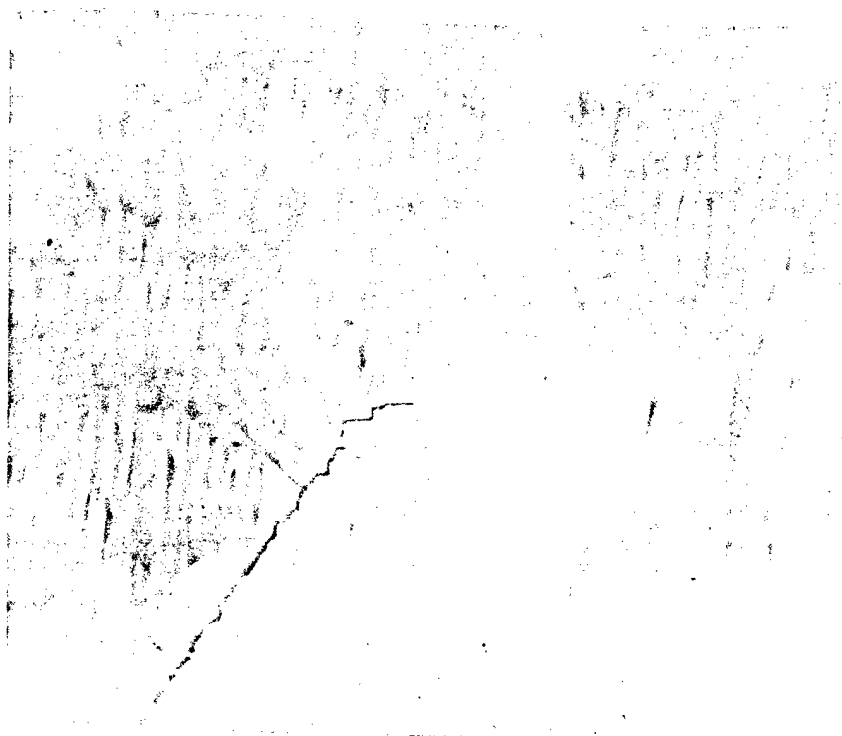


Fig. 3 Crack growth on {100} occurring at low  $\Delta K$ .

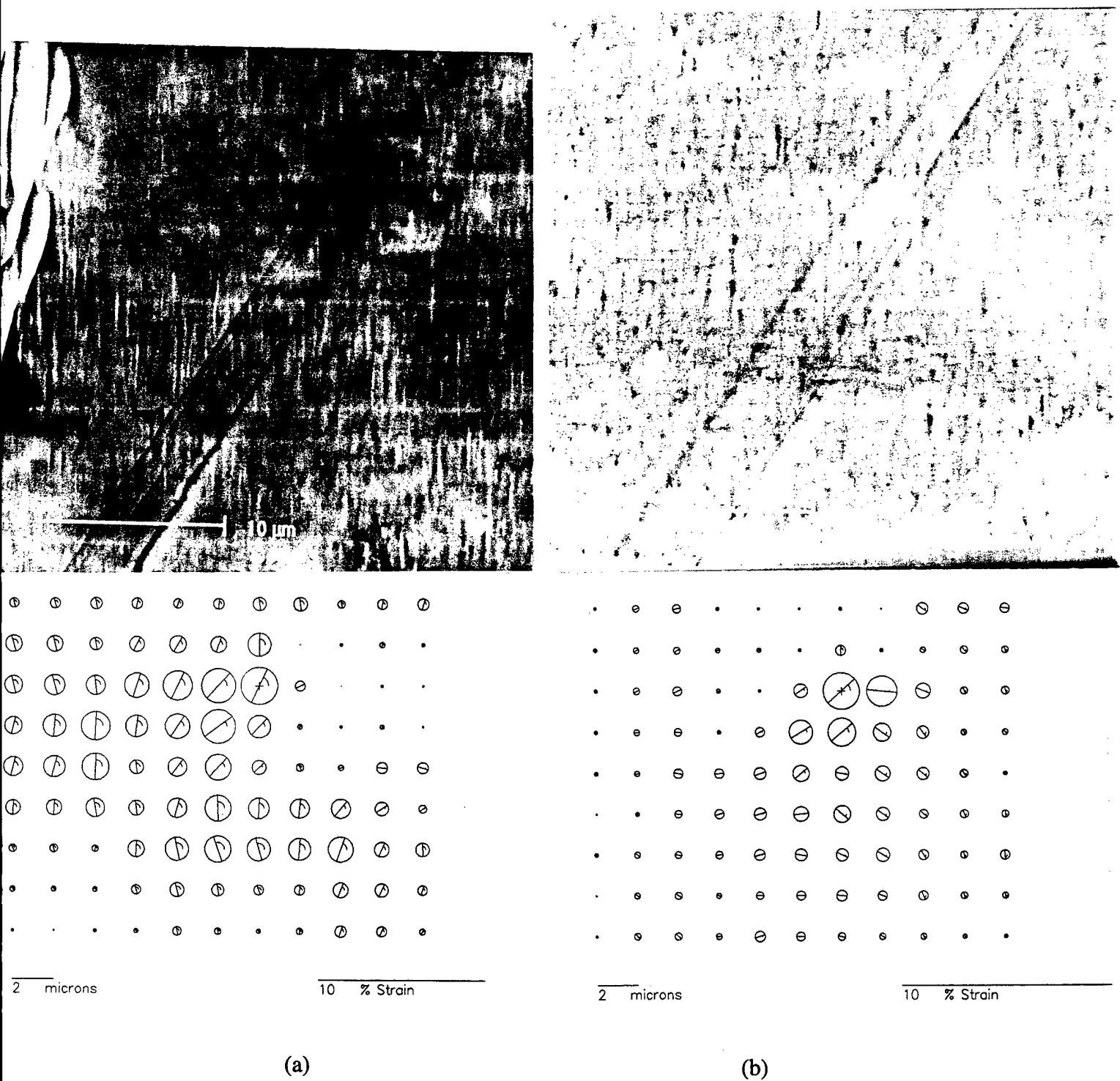


Fig. 4 Experimental observations and strain maps determined by DISMAP. Preliminary calculations predict plastic zone diameters equal to (a) 43  $\mu\text{m}$ , and (b) 25  $\mu\text{m}$ . This result is inconsistent with crack tip strain distribution profiles determined from strains determined by DISMAP.

A preliminary assessment of the plastic zone size was utilized to determine the validity of the measurements. As a first approximation, the standard relationship between plastic zone size, stress intensity and resolved stress was used.

$$2r_p = \frac{K^2}{\pi\sigma^2}$$

It is important to note that the plastic zone size estimated is that for the plane stress condition since the data was collected from observations at the free surface. Estimates of the plastic zone size indicate  $2r_p \approx 43\mu m$  and  $2r_p \approx 25\mu m$ , respectively for the conditions shown in Figure 4. Experimental observations showed slip band extension at the surface some 30-40  $\mu m$  and 20-30  $\mu m$  ahead of the crack tip, for the two cases mentioned previously. Experimental observations thus correlate somewhat with isotropic behavior predictions but not with the strain distributions predicted by DISMAP.

### Possible Sources of Error in Threshold Measurement

As was mentioned previously, threshold data obtained for the decreasing  $\Delta K$  portion was not consistent with data obtained for the increasing  $\Delta K$  portion of the crack growth rate curve. Possible sources for this discrepancy may lie in the notion of a large underload effect. Behavior in similar alloys has exhibited signs of crack arrest due to static underloading and long duration cycling below threshold. Data pertaining to the RENE N5 single crystal was obtained over a number of days. Data obtained for the decreasing portion was obtained with minimal time spent in the underloaded condition. Prior to obtaining the increasing  $\Delta K$  data, the sample had been unloaded for a duration of two days.

Other factors which may be suspect are related to the certainty in the loads applied to the specimen. Incipient heating produced thermal drift of the strain signal used to monitor mean load and no peak height analyzer was employed to obtain accurate resolution of load amplitude. Such procedures produce uncertainty in both the stress intensity range and R-ratio for each segment of the test. Thus, the threshold data may not be as anomalous as appears in the Figure.

All things being equal, it is believed that the undercooling affect produces the greatest contribution to the scatter observed. This, however, remains to be proved and will most likely be the subject of investigations in the future.

### References

1. J. Telesman and L.J. Ghosn: NASA TM-100943, June 1988.

# **SwRI INDEPENDENT RESEARCH PROGRAM**

**Introduction**

**Materials Evaluated**

**Experimental Procedures**



# **SwRI INDEPENDENT RESEARCH PROGRAM**

## **INTRODUCTION**

About 60 % of the program proposed was designed be independent work by SwRI on HCF problems. Because this program was initiated long before either the MURI or the Industry program, it was necessary to obtain materials in advance of all other HCF investigators and begin to develop techniques to study the various HCF damage states that had been identified. Dr. James Hall of Allied Signal, who was to be responsible for procuring material for the Industry and MURI programs, was contacted for advice on obtaining material. Dr Hall suggested that bars of AMS 4928 material be purchased as bar stock from TiMet. He specified heat treatments that would provide microstructures very similar to the forgings that would ultimately be supplied to the HCF program participants. The program began by using material was obtained from TiMet and heat treated according to Dr. Hall's specifications.

## **MATERIALS EVALUATED**

Several materials were evaluated in order to examine the effects of microstructure on fatigue crack growth at the very low rates encountered in the high cycle fatigue region of crack growth. The materials evaluated were all of the composition Ti-6Al-4V.

The Ti-6Al-4V materials evaluated were obtained from three sources: (1) Prior to March, 1998, the material from which specimens were taken was a 19 mm (0.75 inch) diameter extruded bar purchased from TiMet, designated as AMS 4928, that was subsequently heat treated (see below). (2) After about March, 1998, most of the experiments were conducted on specimens cut from pancake forgings supplied by the Industry program in a heat treated condition. Forgings designated as Nos. 138 and 139 were used as material sources. (3) One specimen of Ti-6Al-4V was derived from a HIP container used in the consolidation of mechanically alloyed Nb. This material had a very large grained, transformed beta, fully lamellar microstructure. Laué backscatter x-ray diffraction was used to orient a large grain in this specimen through which the crack was grown.

(1) Alpha-beta microstructure: The 19 mm Ti-6Al-4V AMS 4928 bar stock purchased from TiMet is used as forging stock for gas turbine blades. After receipt, it was heat treated as follows: 1700 deg. F, 1 hr., solution

treatment in argon, air cooled, followed by an anneal at 1300 deg. F in vacuum for 2 hrs., then air cooled. The resulting microstructure is composed of primary alpha grains and transformed beta regions. Primary alpha grains had a distribution of grain sizes centered at 5.6  $\mu\text{m}$ , and ranged in size from 3 to 8  $\mu\text{m}$ . The beta regions occupied a volume fraction of  $0.135 \pm 0.04$ , and were in blocks of about 2  $\mu\text{m}$  square. In transformed beta regions, with alpha and beta laths, the beta laths were about 0.6  $\mu\text{m}$  in width. It has been reported that within the beta regions there are particles of alpha of submicron size. These particles, if present, were not detected during the characterization of this microstructure.

(2) Alpha-beta microstructure: Forging No. 138, received through the Industry HCF program, was purchased from TiMet and forged by Howmet. The microstructure of this material was composed of about 0.12 volume fraction of transformed beta, with alpha grains of approximately 8.2  $\mu\text{m}$  diameter, and transformed beta regions of approximately the same size. Laths of beta within the transformed beta were of approximately 0.4  $\mu\text{m}$  width.

(3) Very large grain size lamellar microstructure: One specimen was derived from a HIP can that was used in the consolidation for some mechanically alloyed Nb. During HIP consolidation, it was heated to 1300 deg. C in Argon, and furnace cooled, resulting in a very large grain structure of lamellar transformed beta. The grains were large enough that they could be oriented using the Laué backscattering technique.

## EXPERIMENTAL PROCEDURE

The experiments described in this report were conducted using the 1.5 kHz machine shown in **Fig. 1**. This device, has been fully described elsewhere [1], is shown placed within the chamber of a Philips scanning electron microscope (SEM) that was used to image specimens under high resolution conditions.

The machine is symmetric about the center of the specimen; thus, only half of the machine will be described. The specimen is seen with two strain gage wires in the center of the machine just beneath one of the reaction frame rods. Static mean stress was applied by hydraulic pressure through the bellows that can be seen on the right. Cyclic loading was applied through a stack of piezoceramic crystals in the load train between the specimen and the end of the reaction frame. A high level of

load transfer was accomplished by tuning the system to operate at resonance, in the range 1.1 to 1.6 kHz for specimens of titanium.

Specimens were designed to be of simple geometry and small enough to minimize material in order to reduce material cost, machining, and specimen preparation. Conversely, the specimen was made large enough to be considered as bulk material. The specimen dimensions are shown in **Fig. 2**. This design also fit the load capacity that was feasible for the 1.5 kHz SEM fatigue machine design.

This program consisted of studying fatigue crack growth under high cycle fatigue conditions. Thus, crack growth rates of less than  $10^{-10}$  m/cycle were of primary interest. No studies of crack initiation were performed. Therefore, the first imperative of the experimental effort was to obtain a crack to study.

After specimens were machined using "low stress procedures" to minimize residual stresses, they were hand polished in the gauge section and then electropolished to remove between 10 and 30  $\mu\text{m}$  of each surface, and the sharp corners were rounded. Cracks were initiated from notches placed in the center of the gauge section by using electric discharge (EDM) or focused ion beam (FIB) machining. EDM notches were larger in size, but were low cost; the FIB notches could be made much smaller, but were expensive to have made. Typical starting notches made by these techniques are shown in **Fig. 3**. The EDM notch depth was made the same as its diameter, and the FIB notch depth was the same as its long dimension. Various notch sizes were tried, and some notches were found to be too small to initiate cracks; in those situations, fatigue cracks initiated from other defects in the specimen. The smallest EDM notch used was about 200  $\mu\text{m}$ , which was based on the EDM equipment capability, and the smallest FIB notch from which a crack was successfully initiated was 35  $\mu\text{m}$ . With both methods for making notches, depth was found to be as important to crack initiation as the dimension perpendicular to the stress direction.

The most successful crack initiation procedure developed was to load notched specimens in 3-point bending at near-yield surface stress levels at the notch using a minimum to maximum load ratio ( $R$ ) = 0.1 until a crack formed. Crack initiation under these conditions usually occurred between  $10^4$  and  $10^5$  cycles at a stress of about half the yield stress, not including the stress concentration. Crack initiation from EDM notches became routine using this procedure, and it was possible to catch cracks of about

50  $\mu\text{m}$  length from the notch. However, crack initiation from the much smaller FIB notches was always much more difficult and only with great care and patience was it possible to initiate and catch cracks from FIB notches while they were still very small in overall dimension including the notch; e.g.  $\approx 50 \mu\text{m}$  long. At this size the cracks were approximately 5 alpha grain diameters in length.

After cracks were initiated in bending in a laboratory fatigue machine, most specimens were ion etched to reveal the microstructure and provide a fine surface texture for stereoimaging work, and a strain gage was applied on the side opposite the notch. Specimens were then inserted into the SEM 1.5 kHz machine for conducting the remainder of the experiment.

## REFERENCES

1. D.L. Davidson, A. Nagy, and T.S. Owen in "High Cycle Fatigue of Structural Materials," W.O. Soboyejo and T.S. Shrivatsan, eds. TMS, Warrendale, PA., 1997, 263-269.

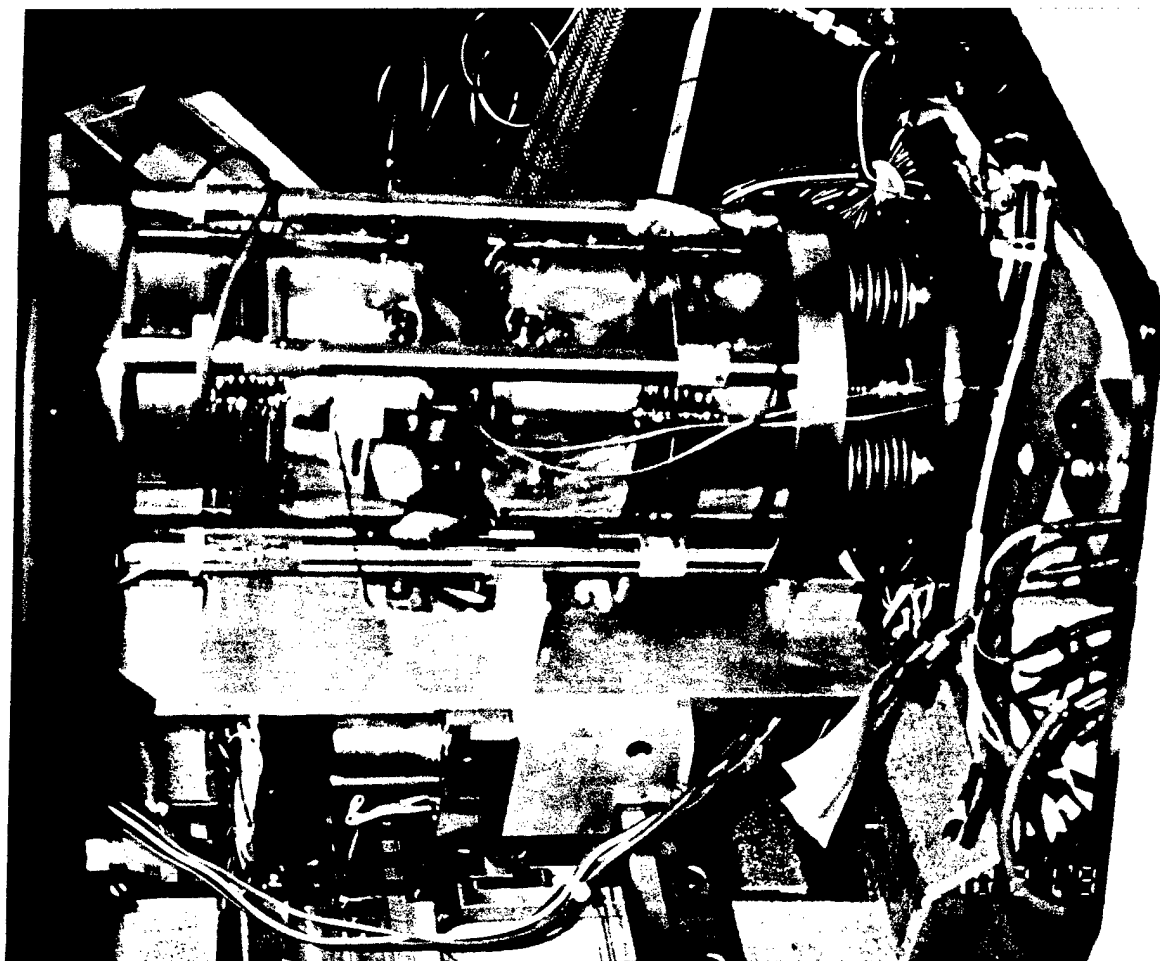


Fig. 1 Fatigue machine that operates at 1.5 kHz within the SEM.

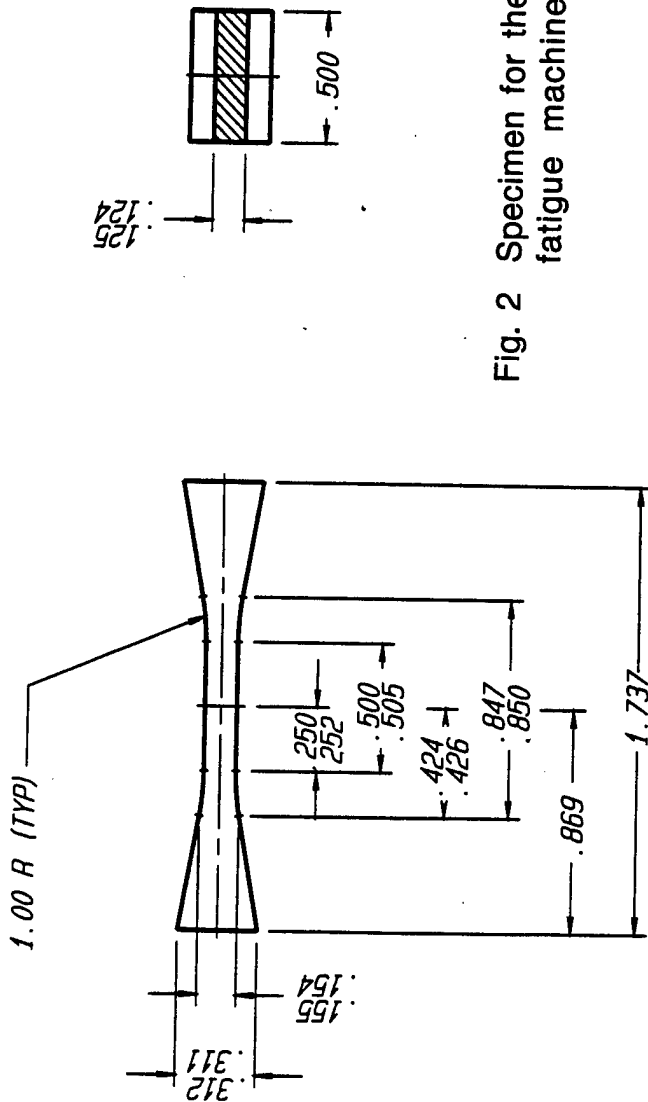


Fig. 2 Specimen for the SwRI 1.5 kHz fatigue machine.

NOTE: DO NOT UNDERCUT RADII; BLEND SMOOTHLY.

LTR		DESCRIPTION		DATE		APPROVED	
FIND NO.		QTY REQ.		CODE IDENT NO.		PART OR IDENTIFYING NO.	
MATERIAL		DECIMALS		FRACTIONS		CONTRACT	
FINISH		2 PLACE		3 PLACE		7-24-1996	
USED ON		± .01		± .003		A. NAGY	
		± .03		± .010			
		± .06		± .015			
		± 0° 30'		± 1° 0'			
		D: 15612KH/SEM/SPC/MCTG					
QTY. REQ.		DRAWING NO.		06-9926-1-5		SHEET	
SCALE		2 = 1					

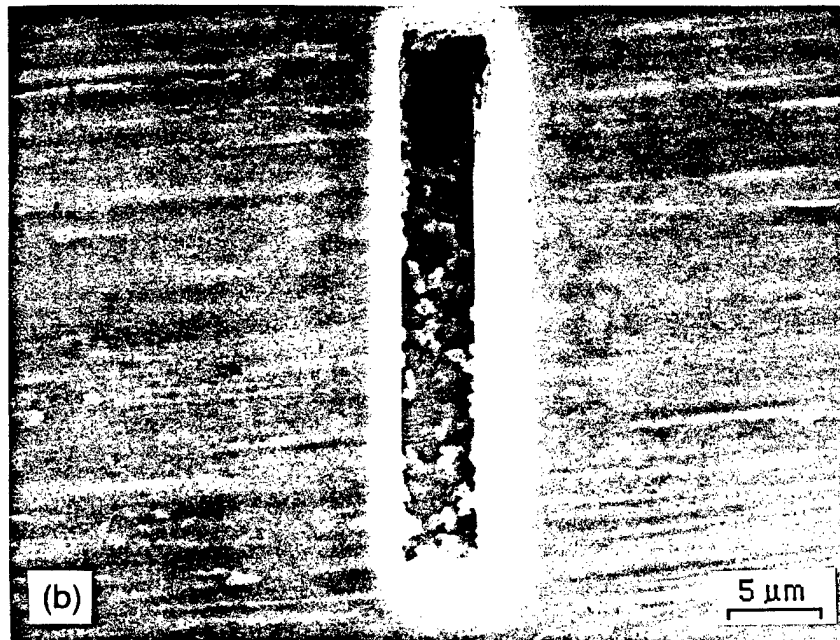
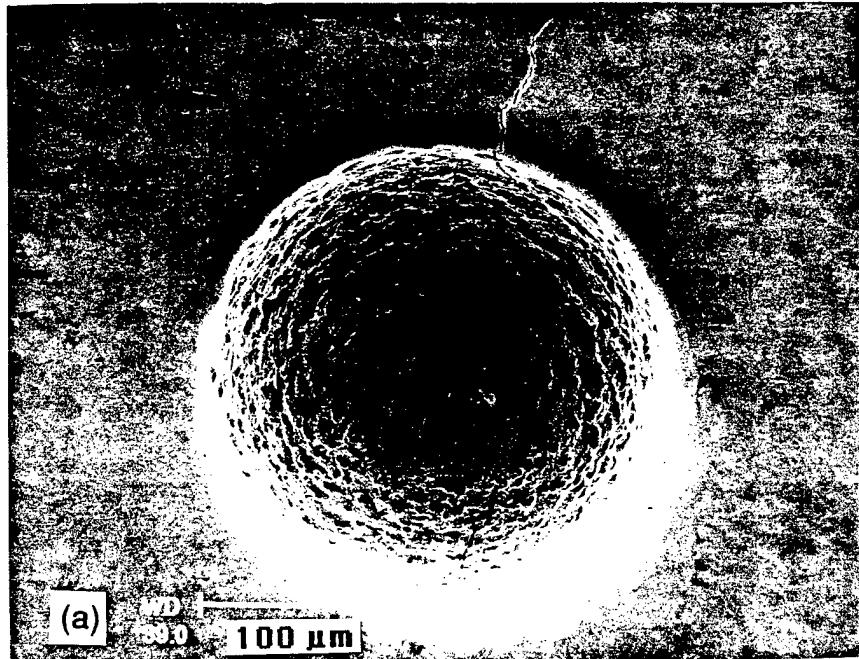


Fig. 3 Notches in Ti-6Al-4V from which fatigue cracks were initiated in 3-point bending: (a) notch made by EDM, and (b) notch made by FIB.

## **RESULTS**

### **Introduction**

***Growth, Micromechanics, and Fractography of Fatigue Cracks in Ti-6Al-4V Cycled at 1.5 kHz in Air and Vacuum at Ambient Temperature***

***Fatigue Crack Growth at High R-Ratio in Ti-6Al-4V at 1.5 kHz:  
The Effect of Periodic Removal of Mean Stress***

***Fatigue Crack Growth in an Aeroengine Disk Due to Blade  
Attachment***

***Analysis of the Forces in the Disk-Blade Attachment of a Gas  
Turbine Aeroengine***

***Foreign Object Damage***



## RESULTS AND ANALYSIS

### INTRODUCTION

This section gives the results the experiments and analyses in the form of manuscripts that have been or are being prepared for publication. Each manuscript is meant to provide a stand alone description of the materials, experimental and analytical techniques used, and results.

The **Appendix** lists each of the specimens evaluated and gives the essential information for the experiments.

# **GROWTH, MICROMECHANICS, AND FRACTOGRAPHY OF FATIGUE CRACKS IN Ti-6Al-4V CYCLED AT 1.5 kHz IN AIR AND VACUUM AT AMBIENT TEMPERATURE**

D.L. Davidson and J.B. Campbell  
Southwest Research Institute  
San Antonio, TX 78228

## **ABSTRACT**

Fatigue crack growth rates and associated micromechanical characteristics for two microstructural variations of Ti-6Al-4V were measured using a 1.5 kHz loading device that fit within a scanning electron microscopy (SEM). Crack growth rates, studied under high cycle fatigue conditions, ranged between  $10^{-12}$  and  $10^{-9}$  m/cycle at  $0.7 \leq R \leq 0.9$ . Crack opening loads (closure), crack tip opening displacements, and crack tip strains were measured. The effect on crack growth in air versus vacuum was also studied, and was found to have a profound effect on the fatigue crack growth rate (FCGR), except near threshold for fatigue crack growth. SEM fractography was performed on the fracture surfaces produced by these experiments; striations were found for all the conditions studied.

## **INTRODUCTION**

When the stresses in gas turbine engine components are sufficiently low, they are designed to endure gigacycles of loading without failure. If cracks are present, or initiate during the lifetime of the component, then to obtain gigacycle lifetimes, the rates of crack growth must be very low. Components of millimeter size should have crack growth rates of no more than  $\approx 10^{-9}$  mm/cycle during service. The fan part of many aeroengines is made of titanium alloys, and fatigue crack growth in these alloys at very low rates is well known to be sensitive to microstructure. Thus, it is necessary to grow fatigue cracks at very low rates to explore the fatigue failures that might occur in the gigacycle realm, and to vary microstructure to determine the sensitivity of this variable. Conventional laboratory testing machines, which can operate up to 50 Hz, are too slow to obtain the crack growth rates of interest. This paper outlines the techniques used to grow fatigue cracks at 1.5 kHz, and presents the results of crack growth experiments in the gigacycle fatigue realm in air and vacuum for two microstructures of a common titanium alloy used in aeroengine blades and disks.

## DESCRIPTION OF MATERIAL AND EXPERIMENTAL PROCEDURES

Specimens were prepared from Ti-6Al-4V that had received the following thermomechanical processing: (1) a pancake forging, No. 138 purchased from TiMet and forged by Howmet, was subsequently solutionized at 1700F, air cooled, and then annealed in vacuum at 1300F for two hrs., and (2) a thick tubular section that was heated to 1300°C for half an hour and slowly cooled. The specimens were machined to fit a 1.5 kHz cyclic loading stage for the scanning electron microscope (SEM) [1]. The resulting microstructures, shown in **Fig. 1**, consisted of (a) primary alpha grains approximately 8  $\mu\text{m}$  in diameter and regions of beta phase, approximately 12 volume percent, which may have also contained secondary alpha phase. The widths of the beta laths averaged approximately 0.4  $\mu\text{m}$ . The lamellar microstructure, Fig. 1(b), is much more difficult to describe. The sizes of the colonies varied widely, but averaged about 200  $\mu\text{m}$ . The lamellae within each colony also varied widely but averaged approximately 2  $\mu\text{m}$  in width.

To initiate fatigue cracks, notches 200  $\mu\text{m}$  diameter by 200  $\mu\text{m}$  deep were cut into the center of each specimen by electrodischarge machining (EDM). The specimens were precracked in air in three-point bend loading in a laboratory servo-hydraulic machine. Three point loading was used to minimize the volume of specimen material subjected to high stresses. Once cracks were initiated, the specimens were transferred to the SEM loading stage where loads were applied axially at about 1.5 kHz. A Philips XL-40 SEM was used to view the cracks and make measurements of their growth using secondary electron imaging. The growth environment was either the SEM vacuum, usually  $7 \times 10^{-6}$  torr ( $5 \times 10^{-5}$  mbar), or lab air (50% relative humidity) at a pressure greater than 0.1 torr.

Fatigue cracks were grown under mean and cyclic loading conditions so that  $0.5 < R$  (min./max. load)  $< 0.85$ , and  $2 < \Delta K < 9$   $\text{MPa}\sqrt{\text{m}}$ , giving average crack growth rates of between  $10^{-12}$  m/cycle and  $10^{-9}$  m/cycle. These average rates were computed from measured crack growth increments ( $\Delta a$ ) at each end of the crack, divided by  $\Delta N$ , the incremental number of cycles, which was usually 0.5 to 1 million cycles. Stress intensity factors,  $\Delta K$  and  $K_{\text{max}}$ , were computed from specimen geometry, cyclic and maximum loads, total crack length, and the assumption of a roughly semicircular crack shape. Low magnification examination of the broken specimens revealed the assumption of a semicircular crack shape to be valid.

By varying the static load, crack opening load could be measured directly at the crack tip, and the crack tip region was photographed periodically

during the experiment at various load levels under static loads equivalent to the dynamic loads, for measurement of micromechanical parameters. Upon completion of the experiments, the specimens were broken open along the crack plane and mounted for SEM fractographic examination. The fracture surfaces of two alpha beta microstructure specimens were examined, with similar results, and one specimen of the lamellar microstructure was examined.

## RESULTS

Fatigue crack growth rate comparisons with existing data from other investigators was made prior to conducting experiments using unknown conditions. Data are compared in **Fig. 2** for large, through-the-thickness cracks being grown in air. Both the UCB data, taken from [2] and the HRLY data, taken from [3], were generated by cycling at 1 kHz. This comparison confirmed that data taken with the 1.5 kHz resonance machine were valid.

Later in the experimental program, a more complete comparison of data from large cracks was compiled that included data taken at 30 Hz and 20 kHz, in addition to data from several specimens taken using the 1.5 kHz equipment. This comparison, shown in **Fig. 3**, includes values of  $\Delta K_{th}$ , as found by various investigators. The Rockwell data were taken from [4], and the CNAM data from [5]. The agreement in measured  $\Delta K_{th}$  is remarkable, with  $2.35 < \Delta K_{th} < 2.55 \text{ MPa}\sqrt{\text{m}}$ , which is probably well within statistical differences for different specimens tested in the same laboratory. More information on fatigue crack growth near the threshold will be given later.

Environmental influence on fatigue crack growth is shown in **Fig. 4**, which compares SwRI data taken in the vacuum of the SEM, which was about  $1 \times 10^{-6}$  torr, to SwRI data taken in air, and data taken in air at University of California, Berkeley. The differences in crack growth rate between vacuum and air are between  $10^2$  and  $10^3$  m/cycle, and are much larger than anticipated from available data. There is reasonable agreement between the SwRI data and UC Berkeley data [2] taken in air. It was not expected that  $\Delta K_{th}$  would be approximately the same in air and vacuum, given the large difference in crack growth rates that developed as  $\Delta K$  increased.

The implications of these results are that a crack that has initiated in the interior of a component and is growing in vacuum will sharply increase in growth rate when the surface is pierced and the environment changes to air. The mechanism by which water vapor effects fatigue cracks is thought to be the separation of water vapor into  $\text{H}^+$  and  $\text{OH}^-$  at the crack

tip by the catalytic action of newly fractured metal. The  $H^+$  then enters the crack tip process zone, and causes the crack to grow faster than it would in vacuum due to "hydrogen embrittlement." One of the possible causes of increased crack growth is that  $H$  causes the crack growth increment  $\Delta a$  to increase while the number of cycles  $\Delta N$  needed to advance the crack was decreased [6].

Fatigue crack growth near threshold was examined using the data shown in Fig. 4. Those data indicate that crack growth is intermittent at stress intensity factors near the threshold,  $2 < \Delta K < 5 \text{ MPa}\sqrt{\text{m}}$ . The threshold was established by cycling the crack in increments of 1 million cycles with observation of the crack tips after each increment. The result is that within this range of  $\Delta K$ , the crack grew during an increasing fraction of the cyclic increments as  $\Delta K$  increased. The inverse of that trend is shown in Fig. 5, where it is seen that as the  $\Delta K_{th}$  is approached, the fraction of intervals in which the crack did not grow increases to 1, with  $\Delta K_{th}$  defined as no growth in 5 million cycles; therefore  $\Delta K_{th} \geq 2 \text{ MPa}\sqrt{\text{m}}$ . This result indicates that definition of  $\Delta K_{th}$  is arbitrary and depends on how it was made. For example, if  $\Delta K_{th}$  was defined as no growth in 4 million cycles, then  $\Delta K_{th} = 2.45 \text{ MPa}\sqrt{\text{m}}$ . If the crack at  $\Delta K = 2 \text{ MPa}\sqrt{\text{m}}$  were cycled 10 million cycles in increments of 1 million cycles, it is conceivable that crack growth would have occurred during one of those increments, thereby causing the threshold to be perceived as  $\Delta K_{th} = 2 \text{ MPa}\sqrt{\text{m}}$ .

The effect of  $R$  ratio on this characteristic of intermittent crack growth is shown in Fig. 6, which includes some data from the literature for the growth of microstructurally small cracks through a similar titanium alloy [7]. The implication of these data are that the intermittent nature of fatigue crack growth is dependent on both the cyclic interval used in the investigation as well as the  $R$ -ratio, with the transition to crack growth in each increment being spread over a larger range of  $\Delta K$  with decreasing  $R$ -ratio. This indicates that  $\Delta K_{th}$  is the most difficult to determine accurately at low  $R$ .

Microstructural effects on fatigue crack growth for the titanium alloys examined here are shown in Fig. 7. Crack growth rates through the lamellar microstructure in vacuum are as much as 100 times less than those in alpha-beta microstructure in vacuum, while crack growth rates through the lamellar material in air are about the same as for the alpha-beta material in vacuum. Unfortunately, the fully lamellar specimen fractured before  $\Delta K_{th}$  was measured.

Crack tip micromechanics of fatigue cracks growing at high R have not been examined for fatigue cracks growing at high R-ratio, prior to this study. Thus, for the alpha-beta microstructure, several analyses for fatigue cracks growing at  $R = 0.85$  were made to complement those at  $R \approx 0.1$  made previously [6].

Crack opening load was measured, approximately, by determining if the crack was open at mean load. This was accomplished by stereoimaging photographs of the crack tip region made at minimum load (mean load minus half the cyclic load) vs. a photograph made at mean load. At many locations, the crack was found not to be fully open to the tip at mean load, while in other locations, it was. In more than half the locations where opening load was estimated, the crack was not fully open at mean load. It had been generally considered that crack closure does not exist at high R.

Crack opening displacements and strains were measured using DISMAP and stereoimaging. Two analyses are shown in **Figs. 8 and 9**, where at each location, strains were determined for minimum vs. maximum load at  $R = 0.85$ . Plastic zones for the crack tips shown in the figures are approximately circular and about  $2 \mu\text{m}$  in diameter. Less than one alpha grain is sometimes encompassed by the plastic zone of a crack tip.

All these analyses were for cracks growing at high R-ratio in vacuum. A comparison is made with similar micromechanics measurements made at  $R = 0.1$  previously in dry and humid air for Ti-6Al-4V with approximately the same microstructure, and is shown in **Fig. 10**.

Time dependent deformation was not detected in these experiments. The maximum stresses used in this work did not result in creep at these crack tips during a 5 to 30 min. time period. Crack tips were photographed at two times separated by about these times several times during the experiment, and these time-sequence photographs were stereoimaged to determine any changes in crack opening that would have been indicative of creep deformation, but none was found. However, creep was found to occur for cracks in other high mean stress conditions, so those conditions were avoided during  $R \geq 0.8$  experiments. Creep was found, in general, to occur when cracks were small and mean stress was high, as necessitated by experiments at high R. In those cases, high R was avoided until crack lengths had increased.

## **FRACTOGRAPHY**

Fractography from specimens of the alpha-beta microstructure was the main thrust because only one specimen of the lamellar microstructure

was available. In addition, it was necessary to use special techniques to thoroughly investigate these fracture surfaces, so the focus was on this microstructure. Several specimens of the alpha-beta microstructure were examined, so the fractography from this material should be representative.

When cycled in air, the crack growth rates were nominally 1000 times those observed in vacuum. This effect of environment on crack growth has been observed before [8]. The most striking fractographic observations involved the contrast in crack morphology between air and vacuum. Visually, the surface fractured in air appeared to have a dull sheen that was not seen on the surface fractured in vacuum. Low magnification SEM stereology, **Fig. 11**, revealed that the fracture surface produced in air was much flatter than the fracture surface produced in vacuum. This is similar to the observation of Sugano, et al. [9]. The fatigue crack front, for both the precrack in air and the transition from fatigue crack growth in air to overload fracture, appears to be a smooth, well-blended, and semi-circle when viewed stereographically. Stereographic viewing of the fatigue crack front at the transition from vacuum to air shows the crack front in vacuum to be of a jagged, hackle-like nature, when viewed locally. At the macroscopic level, however, the crack front after growth in vacuum maintained a roughly semi-circular shape.

The qualitative differences between crack growth in air and vacuum continue from the visual scale to the ultra-microscopic. The distinct difference in general morphology that becomes apparent as magnification is moderately increased is shown in **Fig. 12**. Fracture surfaces made in both vacuum and air were highly faceted, giving the appearance of having failed by brittle cleavage, and, as reported by Ravichandran [10], the facets appear to be fractured grains of alpha phase. Inspection of the surfaces made in both air and vacuum at intermediate and high magnification, under SEM operating conditions that are normally suitable for visualizing fatigue striations, did not reveal any classic striation structures on facets formed in either air or vacuum.

All of the facets observed, from either air or vacuum crack growth, were marked by river lines of varying degrees of coarseness. The sets of river marks on a particular facet collectively formed a fan-shaped structure, with all marks usually emanating from one edge of the facet, suggesting crack initiation at the edge of the facet. This characteristic is well illustrated in **Fig. 12**, especially for crack growth in air, but may also be seen, **Fig. 13**, for crack growth in vacuum. The origin of the fan may be at a high angle to the general direction of macroscopic crack growth, indicating that local crack growth directions were quite different from the macroscopic direction. Careful inspection has shown that usually the

misalignment from crack growth direction was higher on fracture surfaces made in vacuum than those made in air.

The general surface roughness on individual alpha facets was greater for those formed in air than for those formed in vacuum; steps in the river patterns were deeper and the frequency of large river marks was higher, with a finer, more frequent linear structures characterizing the surfaces between coarse river marks. The faceted planes formed in air appear to be, on average, aligned more in the general plane of the fracture, so that the overall fracture surface is smoother in air than in vacuum, as shown in Fig. 13. The beta phase fracture appearance became much more crystallographic, suggesting a more brittle fracture mechanism. Often, the beta was difficult to distinguish from smaller alpha plates.

For crack growth in vacuum, fracture of the transformed beta phase was dominated by a ductile appearance, as may be seen in Fig. 12. These features were of a generally rounded texture on both a coarse and fine scale. The fine scale texture seems to consist of pebble-like agglomerations, suggestive of inverted dimples. Some regions showed round particles of debris. In areas that are not rounded, linear, ridge-like structures blended into the more rounded fractures. The ridge-like structures, to some degree, resemble dimple ridges, though on a finer scale. Occasionally, the beta appears to have broken by cleavage, with sharp steps apparent on the sides of the exposed phase. Microcracks were found at some alpha-beta interfaces.

It was found to be necessary to use a field emission gun equipped scanning electron microscope to image the very fine features on the alpha facet surfaces. These features could not be seen using a SEM with a LaB<sub>6</sub> gun. Under the highest resolution conditions, striation-like structures (parallel, periodic, linear topographic features) were found on the alpha facets grown in air, **Figs. 14(a) and (b)**, and beta structures, **Fig. 14(c) and (d)**. Alpha facets that had undergone crack growth in vacuum were also striated, as may be seen in **Fig. 15**, although they are much more difficult to discern; compare to Fig. 14(b).

Although the overall fracture surface produced by crack growth in air is smoother than that produced in vacuum, the individual facets produced by crack growth in air were found to be rougher than those produced in vacuum. The striations formed in air appear to have higher vertical dimensions (out of plane relief) than that for striations formed in vacuum; hence, they are easier to resolve by secondary electron imaging. Striation spacing for crack growth in both air and vacuum varies from location to location, but it is estimated to be between 0.030 and 0.050  $\mu\text{m}$ .



During the crack growth experiments that produced the fracture surfaces being examined, it was observed that debris was produced on the specimen surface in the crack wake. Material was seen protruding from the crack in some locations, while other cracks, grown under similar  $\Delta K$  levels and R ratios, produced little or no debris.

Fractography from the fully lamellar microstructure is shown in Fig. 16. Although only one location is shown, the features seen are representative of the fracture surface formed in vacuum. The overall fracture surface was very rough, Fig. 16(a), much more so than for the alpha-beta microstructure. The nearly vertical marks seen in Fig. 16(b) and 16(c) are the edges of lamellae. The nearly horizontal parallel marks, approximately perpendicular to the general direction of crack growth are fatigue striations. Average spacing of the striations, as measured from these photographs, is  $0.23 \pm 0.05 \mu\text{m}$ , although the variation in size and shape is large. Comparison of this spacing with crack growth rates in Fig. 7,  $\approx 10^{-10}$  m/cycle, indicates at least 2500 cycles were required to advance the crack one growth increment.

## DISCUSSION

The comparison between data from large fatigue cracks growing through similar microstructures taken in air at Pratt and Whitney [3], University of California at Berkeley [2], and Southwest Research Institute, all taken at about 1 kHz, is in excellent agreement, Fig. 2. Thus, it is concluded that valid data could be obtained using the resonance equipment.

Under similar cyclic loading conditions ( $\Delta K$ , R ratio and cyclic frequency), the fatigue crack growth rates in air were on the order of  $10^3$  times those observed in vacuum at intermediate levels of  $\Delta K$ . This strong environmental effect, which has been observed many times in titanium alloys is thought to be the result of atmospheric water vapor being dissociated into atomic and molecular hydrogen at the crack tip [6,8], or caused by the rapid oxidation of new crack surface [9] which alters the crack path morphology, or both. Unexpectedly, the threshold for fatigue crack growth seems to be unaffected by the presence of water vapor.

This research has raised questions about just how to define  $\Delta K_{th}$ . It has always been apparent that determining  $\Delta K_{th}$  was dependent on the patience of the investigator, but it has been possible with high frequency loading equipment to examine that issue more quantitatively. The results given in Fig. 5 showed that no growth occurred in 5 million cycles at  $\Delta K = 2 \text{ MPa}\sqrt{\text{m}}$ , and this value was presumed at R = 0.8 to be below  $\Delta K_{th} \approx 2.35$ .

However, under high cycle fatigue conditions, where the lifetime of a component may be a gigacycle, is it sufficient to cycle only 5 million cycles to establish  $\Delta K_{th}$ ? Could the crack begin to grow again after an additional 50 or 100 million cycles? It seems clear enough from Fig. 5 that cycling only for 1 million cycles is insufficient to establish a reliable value of  $\Delta K_{th}$ . There appears to be no way to resolve these questions except to carefully explore crack growth response very near  $\Delta K_{th}$  for an exceedingly large number of cycles.

The effect of R-ratio on the probability of crack growth in the near threshold region is equally interesting, mainly because it indicates that establishing a threshold value may be more sensitive to experimental conditions at low R than at high R.

Considerable additional work is required to establish the reasons for the differences in crack growth rate characteristics between the alpha-beta and fully lamellar microstructures, addressed briefly in the results shown in Fig. 7. The heat treatment used to form the fully lamellar material is closer to equilibrium than the heat treatment used to form the alpha-beta microstructure; thus, the alloying elements are partitioned differently between the two phases, and this factor may lead to differences in the effect of environment on fatigue crack growth. Also, there are differences in crack path, with the fully lamellar structure showing much larger regions of planar crack growth, which must indicate much more crystallographic cracking. This behavior could also be important to the rate of crack advance.

The crack tip micromechanics results obtained at high R compare well to similar information obtained at low R, Fig. 12. Thus, the effects of high R, and lower values of  $\Delta K$ , are consistent with measurements at lower R, but higher  $\Delta K$ . The slope of the maximum shear strain vs. CTOD correlation is about 0.67, which is also consistent with similar results from aluminum alloys [11]. Some differences do exist when comparing the individual crack tip analyses, however. It has been found that CTOD usually is a linear function of the square root of the distance behind the crack tip ( $CTOD \sim C_0\sqrt{d}$ ) at low R, but for the analyses shown at high R, this correlation was not found; thus, CTOD was shown in Figs. 8 - 11 as a function of d, the distance behind the crack tip. This lack of correlation with  $\sqrt{d}$  brings into question the use of  $\Delta K$ , as derived from linear elastic fracture mechanics, as a correlating parameter, although it is unclear just how important this issue may be.

Compared to fatigue cracks growing in aluminum alloys, the level of Mode II crack opening is very low. In the aluminum alloys, the level of Mode II was generally found to exceed that of Mode I in the near-threshold region [11]. This is clearly not the case for the alpha-beta microstructure, where Mode I dominates even very near  $\Delta K_{th}$ . Finally, the size of the plastic zone approximates the size of the alpha plates in the alpha-beta microstructure; thus, the value of  $\Delta K_{th}$  might be expected to depend on the alpha grain size. However, determination of the alpha grain sizes of the materials used in the comparison of Fig. 3 indicated a range of about 5 to 15  $\mu\text{m}$ , while the differences in  $\Delta K_{th}$  are  $\pm 0.1 \text{ MPa}\sqrt{\text{m}}$ . If there is an effect of alpha grain size, it is very small.

What are apparently fatigue striations are visible on both air and vacuum fatigue fracture surfaces, but they can be seen only by high resolution field emission SEM. Striations denote locations where crack advance was arrested. The observed striations are only very slightly elevated above the facet plane, especially in vacuum, indicative of low levels of crack tip deformation, which agrees with the measurements, Figs. 8 and 9, of crack opening displacement and strain. Low topography requires imaging conditions in the SEM that minimize the electron beam-specimen interaction volume, which increases the secondary electrons collected from the near specimen surface. A SEM gun accelerating voltage of 3 keV was used for this high resolution imaging. Most striations observed were on facets and beta laths that were tilted from the SEM beam towards the secondary electron detectors. The tilt angle was not over  $\approx 30^\circ$  for the facets viewed, so the foreshortening error in striation spacing measurements, but measurements was probably small.

For a growth rate of  $10^{-12} \text{ m/cycles}$ , 1  $\mu\text{m}$  of crack growth requires  $10^6$  cycles. At 50 nm per striation, there are 20 striations in 1  $\mu\text{m}$  of growth. This means that under vacuum conditions, it takes on average 40,000 cycles to produce one striation. Under the same conditions of  $R$  and  $\Delta K$ , crack growth in air is about 1000 times faster; thus, it takes 40 cycles to produce one striation. Clearly, in vacuum, the crack is not making one striation per loading cycle, and it is also doubtful that the crack is making one striation per loading cycle in air.

For fatigue crack growth rates of  $\approx 10^{-12} \text{ m/cycle}$ , the plastic zone size was determined to be roughly circular, and about 2  $\mu\text{m}$  in diameter, which is about 100 times larger than the observed striation spacing. Approximately  $2 \times 10^6$  cycles were needed for the crack to traverse a 2  $\mu\text{m}$  plastic zone. The volume of material in the plastic zone would, therefore, experience about  $2 \times 10^6$  cycles of loading.

The shapes of the plastic zones were not elongated in the direction of cracking, which means that dislocations are moving on multiple planes in about equal proportions. Transmission electron microscopy (TEM) of material near the fracture surface of this alloy has shown that the microstructure is altered by the relatively large strains in the plastic zone as the crack grows [12-14]. Dislocation arrays and subgrains are formed in the near tip process zone, as they are in aluminum alloys [11]. But, because of the small plastic zone size, subcell formation is extremely localized near the fracture plane. Even though there is relatively homogeneous dislocation motion forming the plastic zone, the cracking of alpha grains is planar on a micrometer scale. However, on the nanometer scale, the fracture surface is not planar, as evidenced by striation formation and river lines. The crack path, which is usually on or near the basal plane for titanium alloys [15, 16], but sometimes near the prismatic plane [15] could be through subgrain boundaries because they are regions of high dislocation density [11]; however, there could also be other mechanisms of striation formation. The available TEM is insufficient to accurately know the size of the subcells formed during fatigue, so additional research is required to make any positive connection between subcell size and striation spacing. It is doubtful if the surfaces that bound striations, such as seen in Figs. 5 and 6, are simply along specific crystallographic planes because of their very rounded appearance.

## CONCLUSIONS

All the conclusions given are for the alpha-beta microstructure, except where the lamellar microstructure is specified.

1. Fatigue crack growth rates in air  $R \geq 0.7$  below  $10^{-9}$  m/cycle appear to be frequency independent  $30 \text{ Hz} < \text{frequency} < 20 \text{ kHz}$ .
2. Fatigue crack growth in air is about 1000 faster than in vacuum, except near  $\Delta K_{th}$  where they are about the same.
3. Exact determination of  $\Delta K_{th}$  may depend critically on the patience of the investigator.
3. For fully lamellar microstructure, fatigue crack growth rates are  $\approx 100$  times lower than for the alpha-beta microstructure.
4. Crack tip opening displacements and strains measured at  $R = 0.85$  are consistent with  $R = 0.1$  measurements.

5. Fracture surfaces formed in air were macroscopically smoother than those formed in vacuum, but the microscopic features were the opposite.
6. The roughness of alpha grain facets formed in vacuum were smoother than those formed in air.
7. Fans of lines (rivers) were found on alpha facets formed in both air and vacuum. The origin of the fans was at the edges of alpha grains. In vacuum, the origins of the fans were often at large angles to the direction of crack growth, while for growth in air, the origins were closer to the direction of crack growth.
8. Fatigue striations were detected on alpha fracture facets formed in both air and vacuum, but the topographic features were higher on the air-formed surfaces. Striations were formed between river lines.
9. The range of striation periodicity was measured as 30 to 50 nm from alpha facets formed in both air and vacuum.
10. Plastic zone sizes of the fatigue cracks that grew in vacuum were approximately circular with a diameter of about 2  $\mu\text{m}$ , which is smaller than the alpha grain size of 5 - 8  $\mu\text{m}$ . For a crack growth rate of  $\approx 10^{-12}$  m/cycle, an average of 40,000 cycles were required to form one striation.
11. Fatigue crack advance in vacuum through the fully lamellar microstructure required at least 2500 cycles.

## ACKNOWLEDGEMENTS

This research was funded by Air Force Office of Scientific Research under contract F49620-96-C-0037. Interactions with investigators for the MURI program on High Cycle Fatigue has greatly enhanced these results. The help of Dr. R. Wanhill in obtaining references is appreciated. We are grateful for the frequent interactions with Andy Nagy and Dr. T. Owen, designers of the 1.5 kHz SEM fatigue machine. We appreciate the assistance of Julie Henkener and Louis Hulse of NASA Johnson Space Center who made available their field-emission SEM.

## REFERENCES

1. D.L. Davidson, A. Nagy, and T.S. Owen in *High Cycle Fatigue of Structural Materials* W.O. Soboyejo and T.S. Shrivatsan, eds. TMS, Warrendale, PA., 1997, 263-269.

2. R.O. Ritchie, D.L. Davidson, B.L. Boyce, J.P. Campbell, and O. Roder "High - cycle fatigue of Ti-6Al-4V" Fatigue and Fracture of Engineering Materials, (in review) Aug. 1998.
3. S.W. Hopkins, C.A. Rau, G.R. Leverant, and A. Yuen in *Fatigue Crack Growth Under Spectrum Loads ASTM STP 595*, Am. Soc. for Testing and Mater., Philadelphia, PA, 1976, pp. 125-141.
4. Thompson, A.W., J.C. Williams, J.D. Frandsen, and J.C. Chesnutt, "The effect of microstructure on fatigue crack propagation in Ti-6Al-4V", in *Titanium and Titanium Alloys: Scientific and Technological Aspects*, eds. J.C. Williams and A.F. Belov, Plenum Press, p. 691-703 (1982).
5. C. Bathias, K. El Alami, and T.Y. Wu, Eng. Fract. Mech., 1997, v. 56, pp. 255-267.
6. D.L. Davidson and J. Lankford "Fatigue crack growth mechanics for Ti-6Al-4V in vacuum and humid air" Met. Trans. A, 1984, 15A, pp. 1931-1940.
7. A.L. Dowson, A.C. Hollis, and C.J. Beevers, Int. J. Fatigue, 1992, 14, pp. 261-270.
8. P.E. Irving and C.J. Beevers, Met. Trans., 1974, v.5, 391-398.
9. M. Sugano, S. Kaano, and T. Satake, Acta metall., 1989, v. 37, pp. 1811-1820.
10. K.S. Ravichandran, Scripta. Metall. et Mater., 1990, v. 24, pp. 1275-1280.
11. D.L. Davidson and J. Lankford, Int. Mat. Rev., 1992, 37, 45-76.
12. J.C. Grosskreutz and G.G. Shaw, Acta metall., 1972, v. 20, 523-528.
13. R.J.H. Wanhill and H. Doker "Vacuum Fatigue Fracture in Titanium Alloy Plate" 1977, NLR MP 78002, National Aerospace Laboratory, The Netherlands.
14. S. Dubey, A.B.O. Soboyejo, and W.O. Soboyejo, Acta mater., 1997, v. 45, 2777-2787.
15. D. Shechtman and D. Eylon, Met. Trans. A, 1978, v. 9A, 1018-1020.
16. D.L. Davidson and D. Eylon, Met. Trans. A, 1980, 11A, 837-843.



Fig. 1(a) Ti-6Al-4V forged and heat treated to give an equiaxed alpha-beta microstructure.

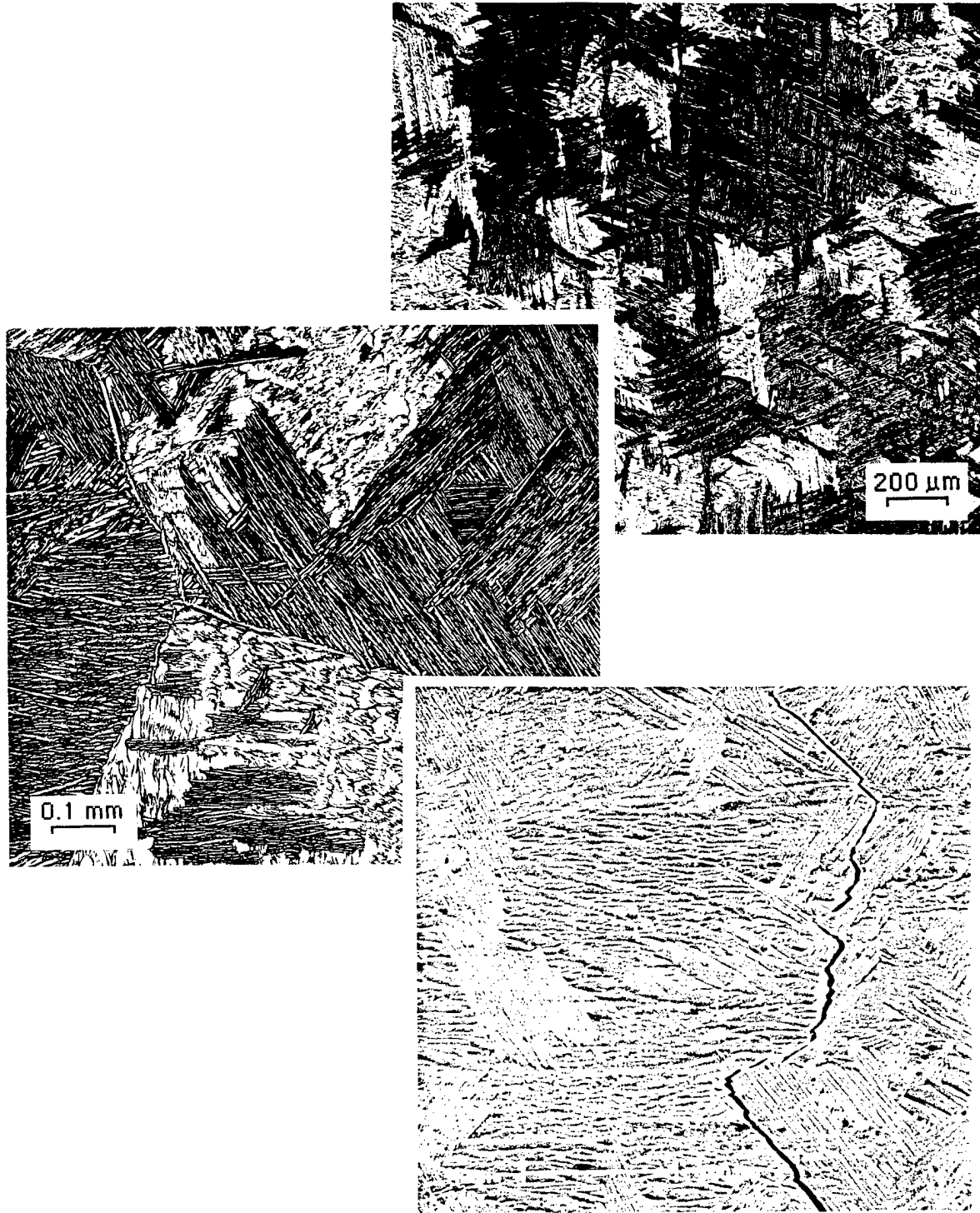
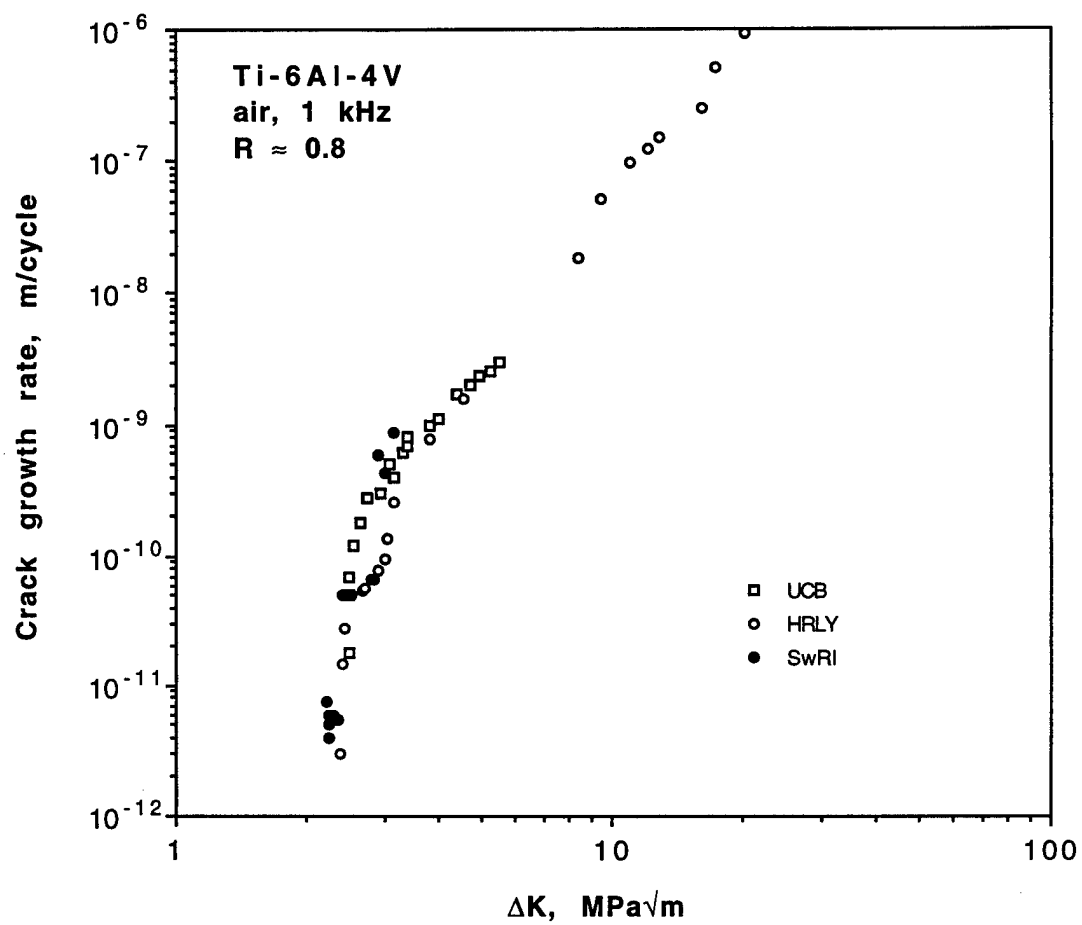


Fig. 1(b) Ti-6Al-4V slowly cooled to give a fully lamellar microstructure.





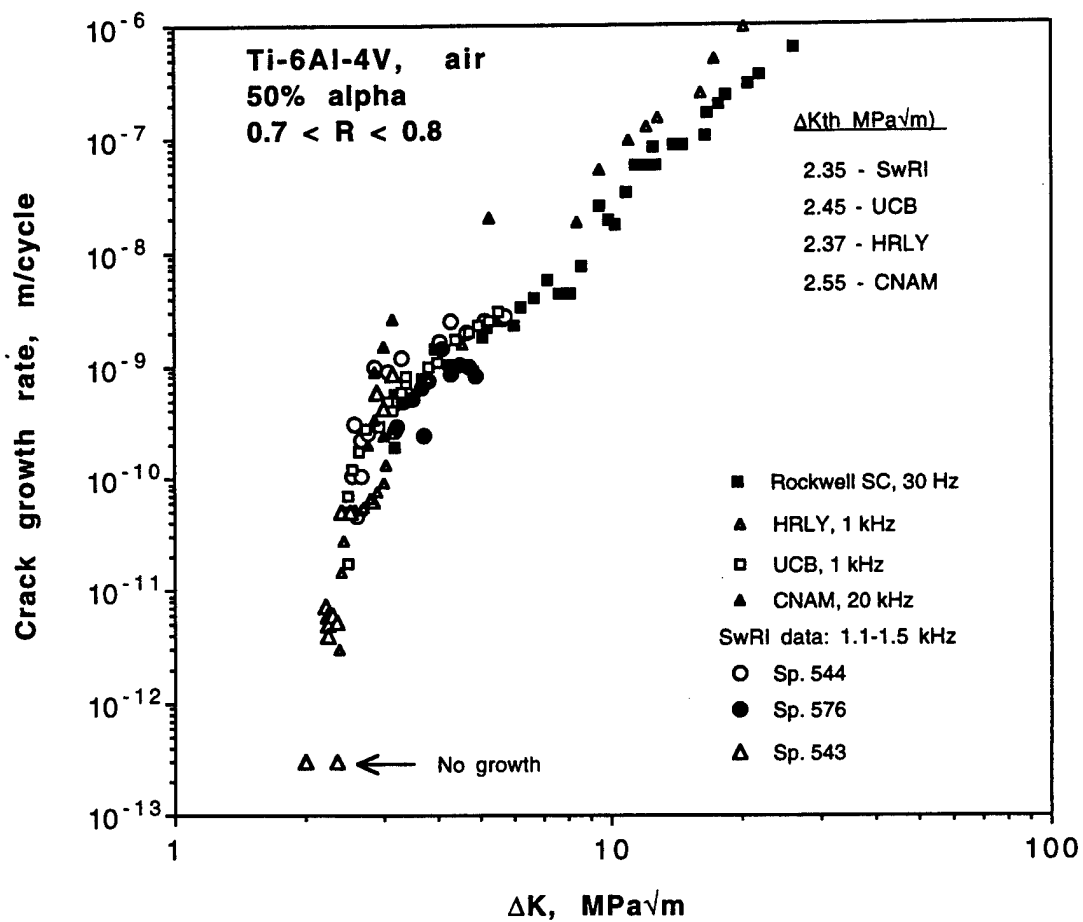


Fig. 3 Comparison of large crack growth rate data at various cyclic rates and derived values of  $\Delta K_{th}$ .

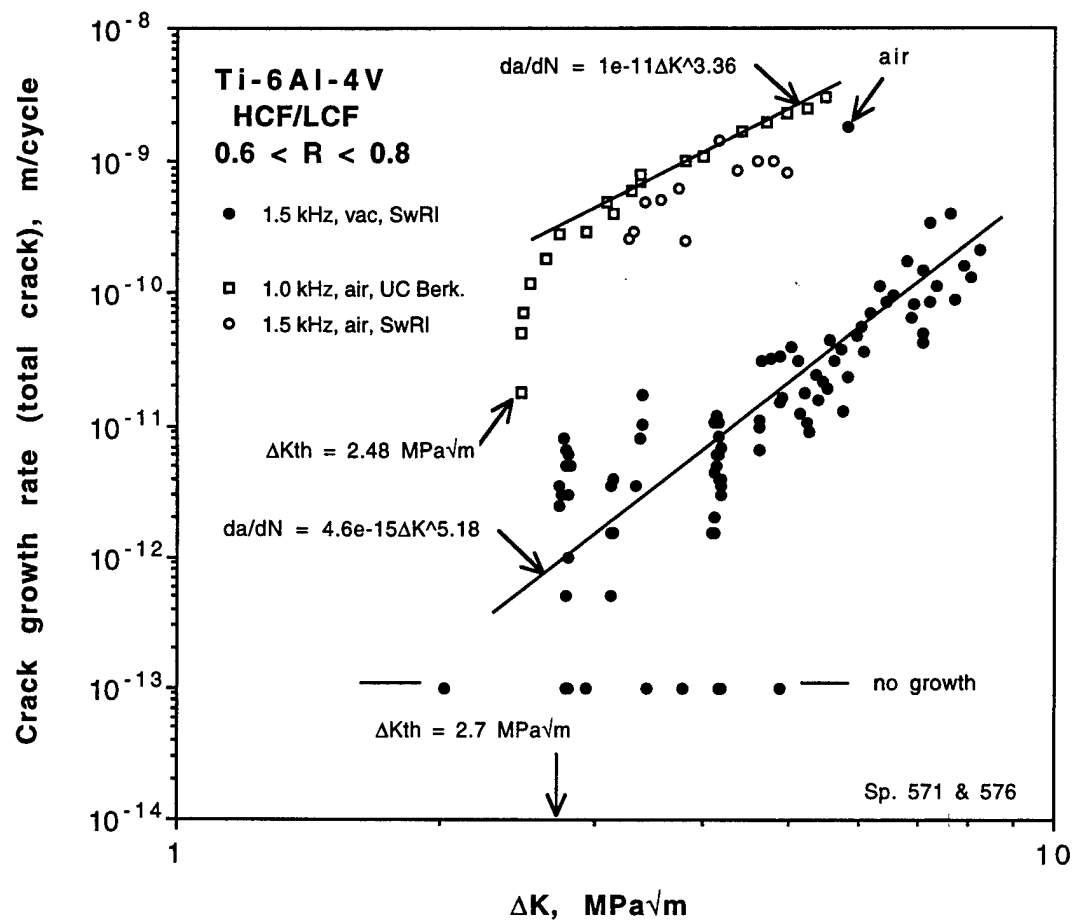


Fig. 4 Effects of environment on fatigue crack growth rates.

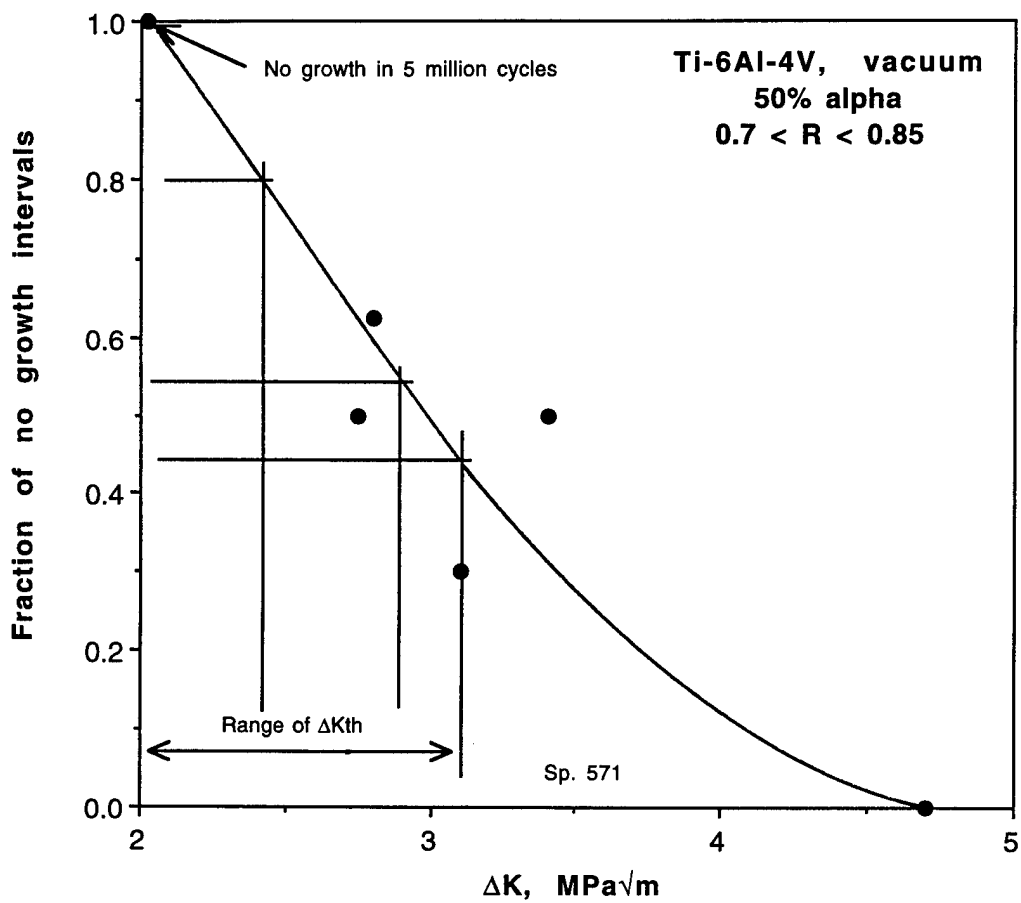


Fig. 5 Fatigue crack growth near the threshold,

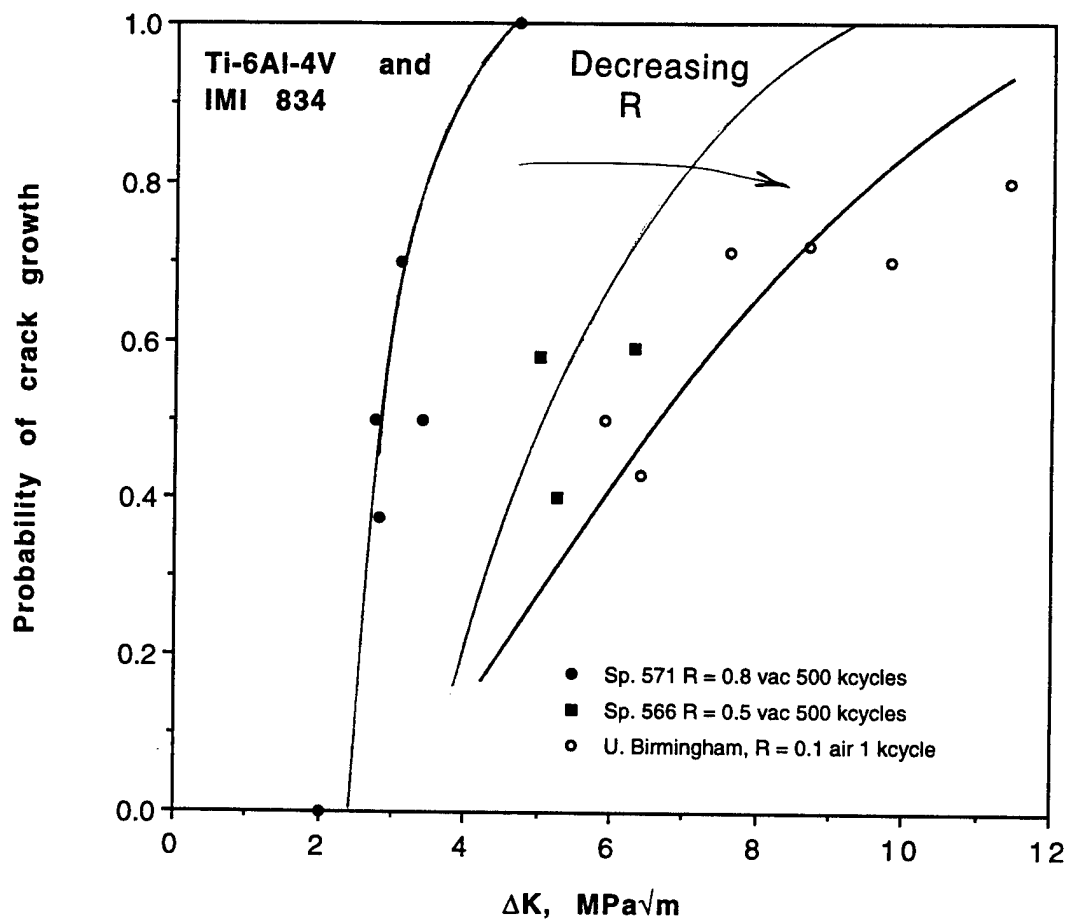


Fig. 6 The effect of R ratio on intermittent crack growth.

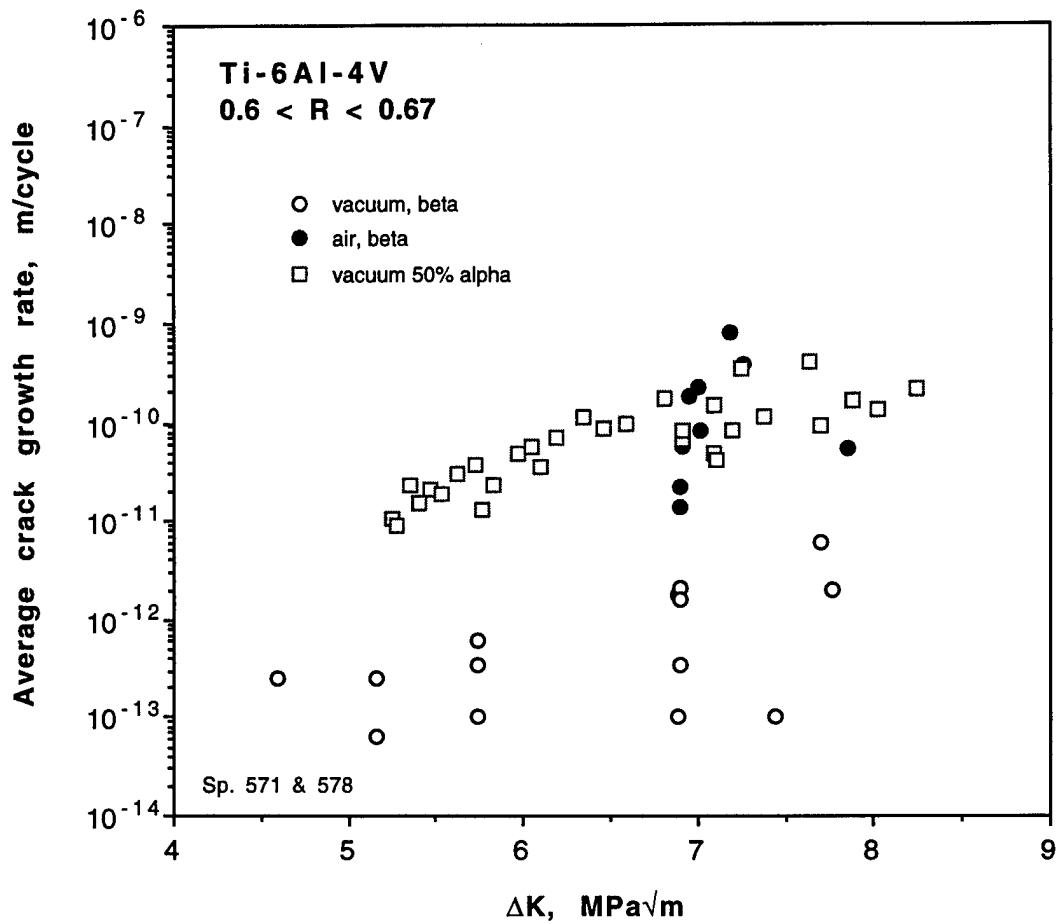


Fig. 7 Crack growth rates through the fully lamellar microstructure to growth rates through the alpha-beta microstructure.

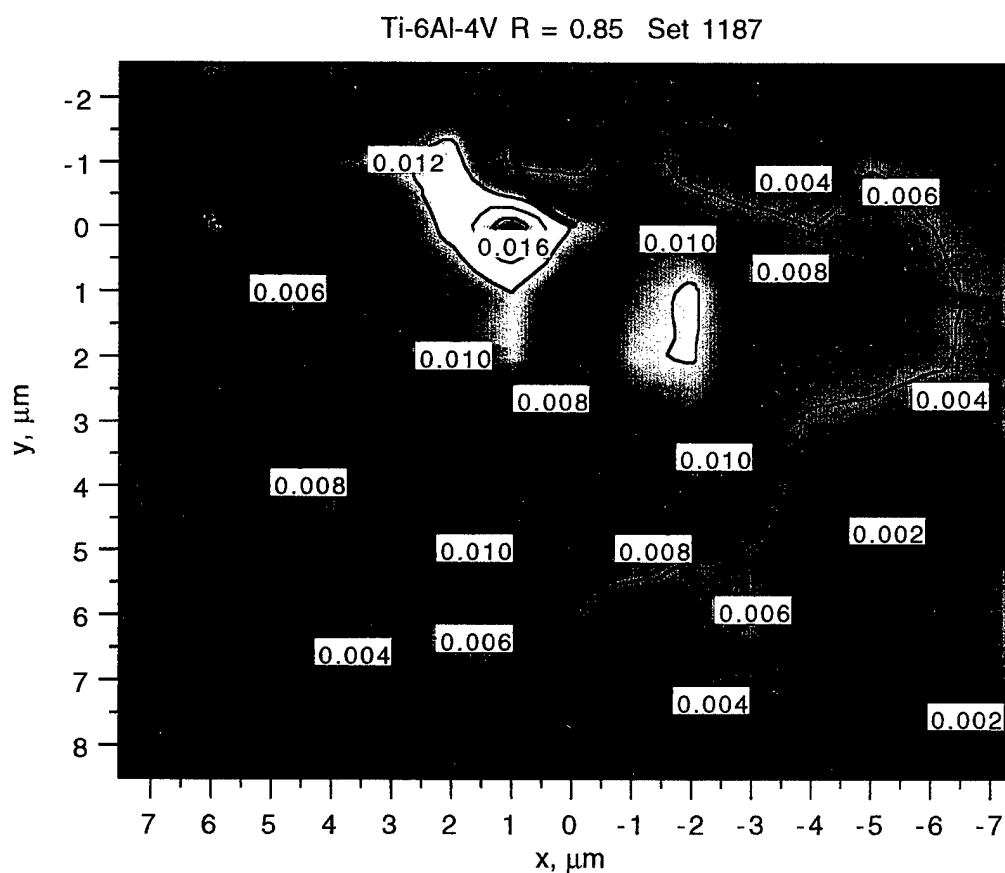
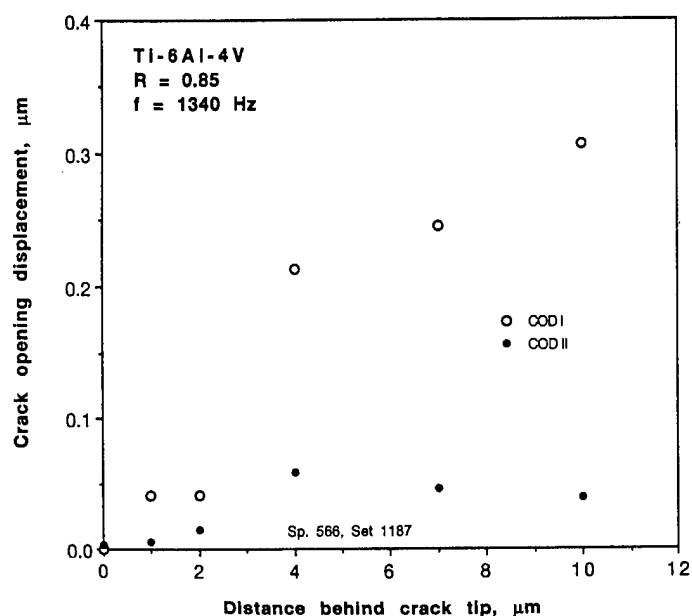
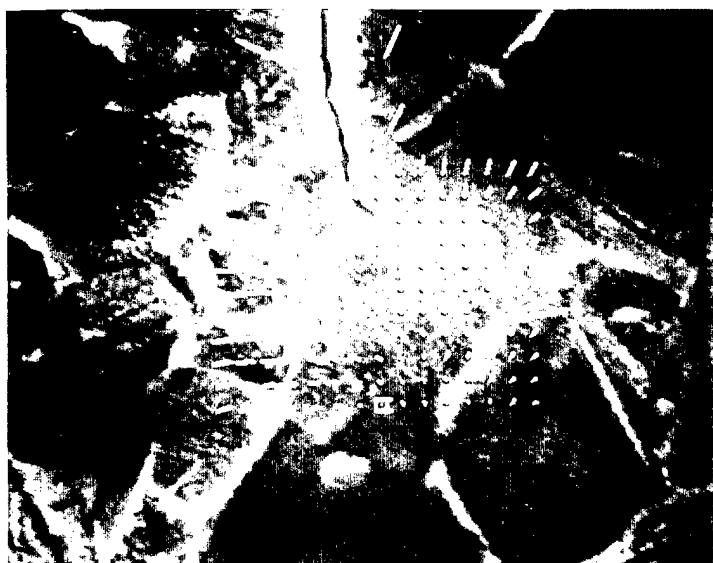


Fig. 8 Micromechanics analysis for a crack growing at  $\Delta K = 2.16 \text{ MPa}\sqrt{\text{m}}$ , crack growth rate  $= 10^{-11} \text{ m/cycle}$  in vacuum. Displacements were measured each  $1 \mu\text{m}$  and are 10x actual value. Modes I and II COD and the distribution of maximum shear strain are shown. The crack tip plastic zone crosses an alpha grain boundary. Crack growth under steady state conditions.

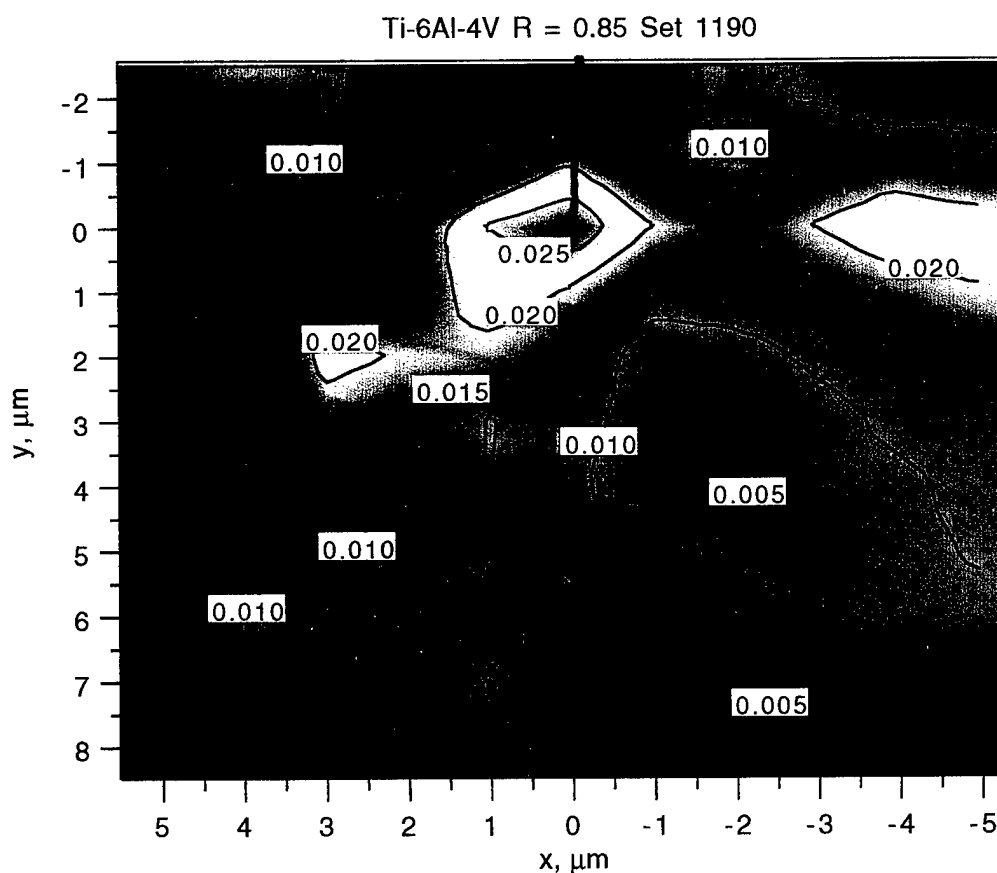
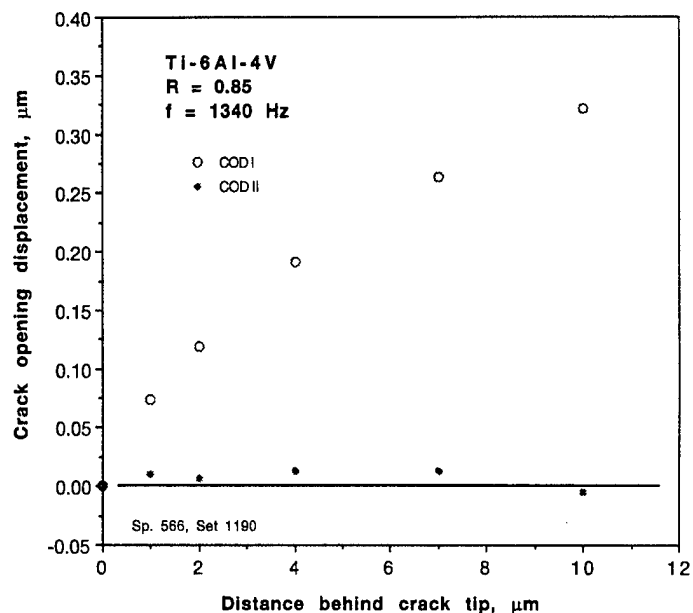


Fig. 9 Micromechanics analysis for a crack growing at  $\Delta K = 2.25 \text{ MPa}\sqrt{\text{m}}$ , crack growth rate =  $2 \times 10^{-11} \text{ m/cycle}$  in vacuum. Displacements were measured each  $1 \mu\text{m}$  and are  $15\times$  actual value. Modes I and II COD and the distribution of maximum shear strain are shown. The crack tip plastic zone is almost entirely within one alpha grain.



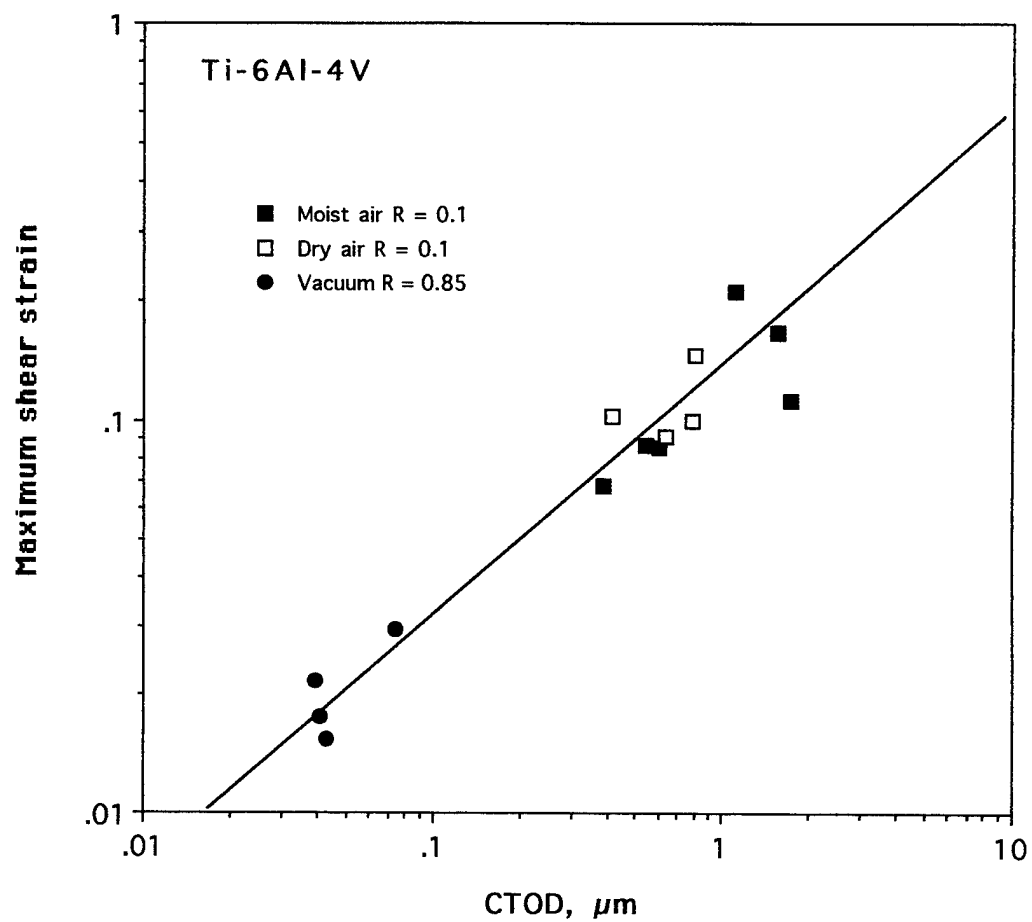


Fig. 10 Comparison of the correlation between crack tip opening displacement and crack tip maximum shear strain with previous measurements at low  $R$ .

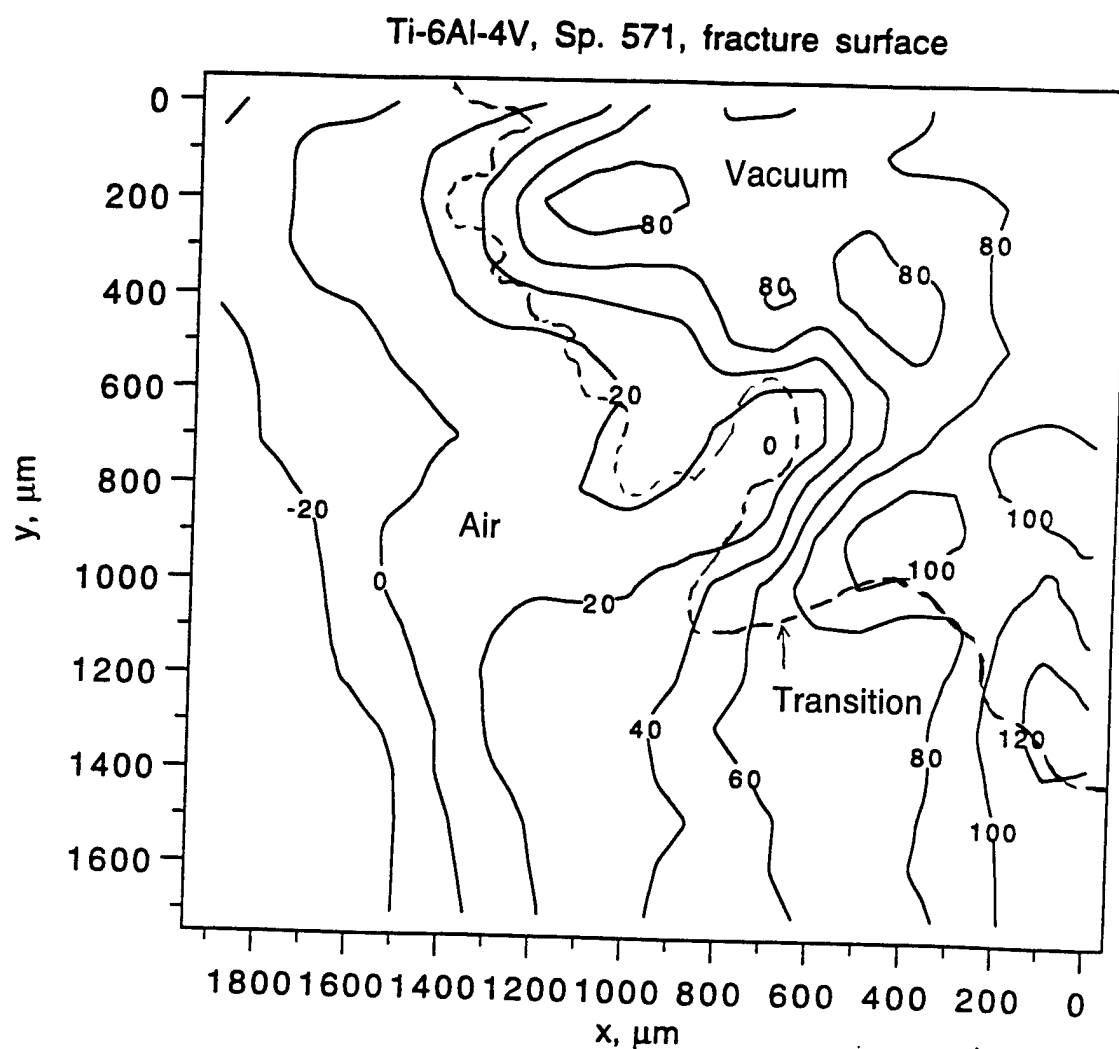
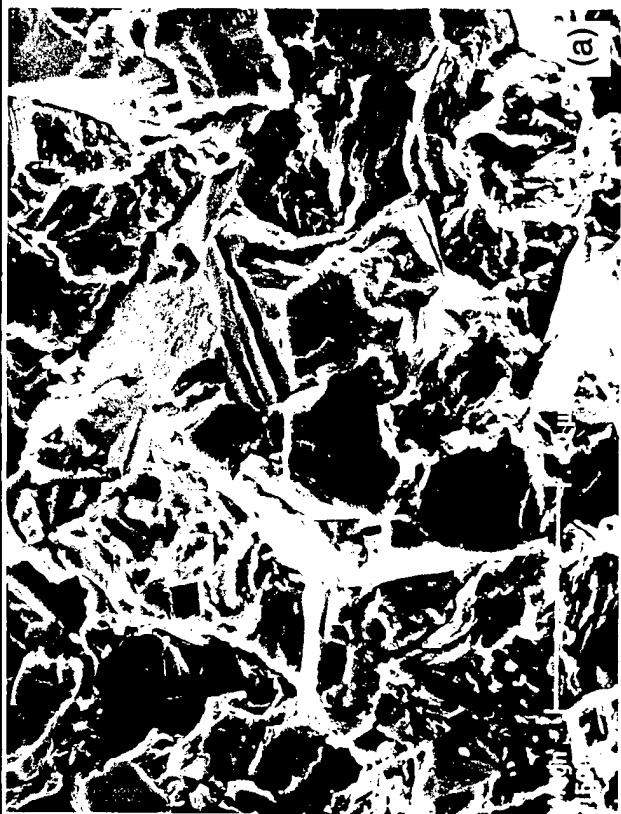


Fig. 11 Contour map of a major portion of the the fracture surface of one specimen grown under high cycle fatigue conditions. The transition from growth in vacuum to that in air is shown. The fracture surface from crack growth in vacuum is rougher than that from growth in air.



Crack growth direction



Fig. 12 Comparison of fracture surfaces produced by fatigue crack growth in (a,b) vacuum and (c,d) air. (a,b)  $\Delta K = 5.5 \text{ MPa}\sqrt{\text{m}}$ ,  $da/dN = 2 \times 10^{-11} \text{ m/cycle}$ . (c,d)  $\Delta K = 6.0 \text{ MPa}\sqrt{\text{m}}$ ,  $da/dN = 2 \times 10^{-9} \text{ m/cycle}$ . The flat facets are fractures of alpha titanium grains. Fracture of the transformed beta regions is much less planar.



Vacuum:  $\Delta K = 5.5 \text{ MPa}\sqrt{\text{m}}$   
 $da/dN \approx 2 \times 10^{-11} \text{ m/cycle}$

Crack growth direction →

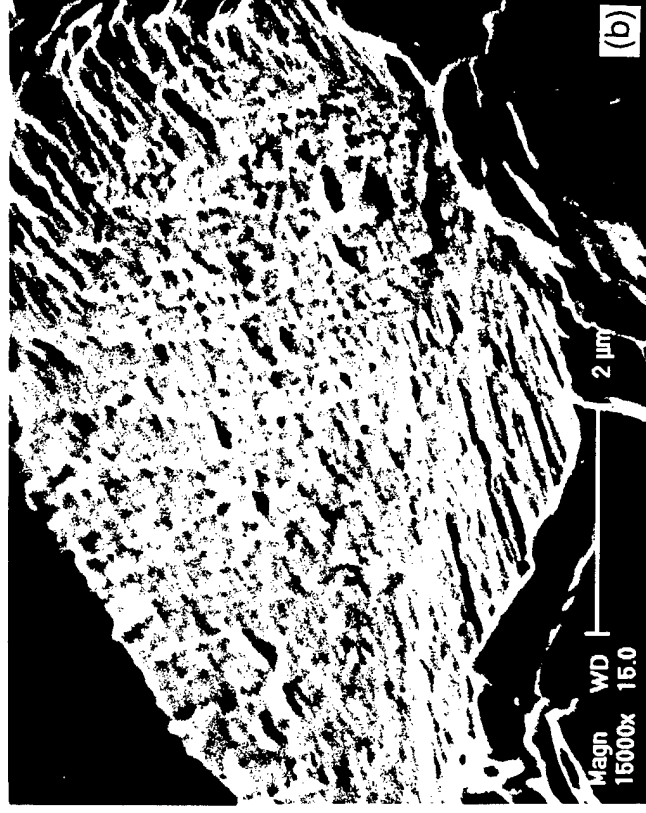


Fig. 13 Fracture of alpha grains produced by fatigue crack growth in (a) vacuum showing river lines similar to those (b) made by crack growth in air. The features in vacuum have much less topography and are harder to detect. (a) Vacuum:  $\Delta K = 5.5 \text{ MPa}\sqrt{\text{m}}$ ,  $da/dN = 2 \times 10^{-11} \text{ m/cycle}$ . (b) Air:  $\Delta K = 6.0 \text{ MPa}\sqrt{\text{m}}$ ,  $da/dN = 2 \times 10^{-9} \text{ m/cycle}$ .

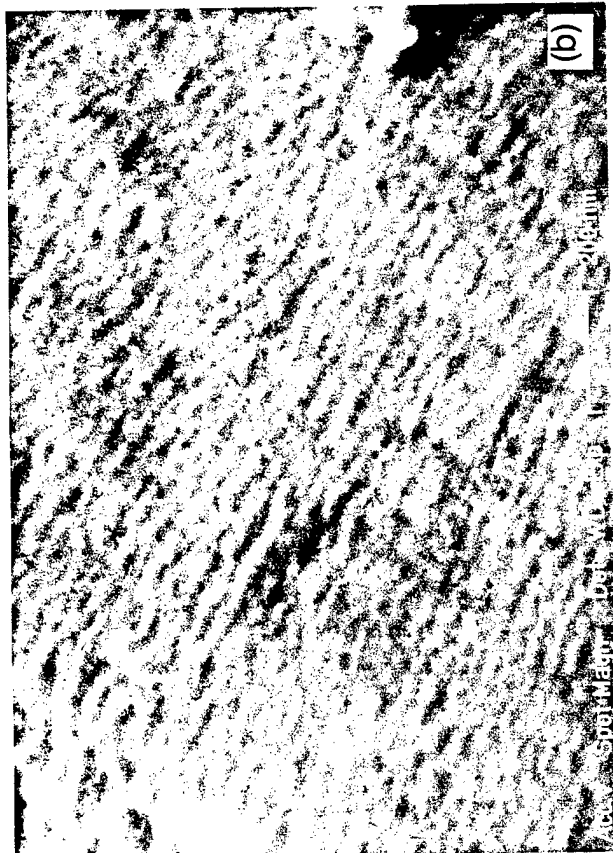


Fig. 14 Fatigue crack growth in air: (a) and (b) show striations formed on an alpha facet, while (c,d) show striations in a region of beta.



Fig. 15 Faint striations found on an alpha facet grown in vacuum. Magnification is the same as Fig. 16(b) for comparison.

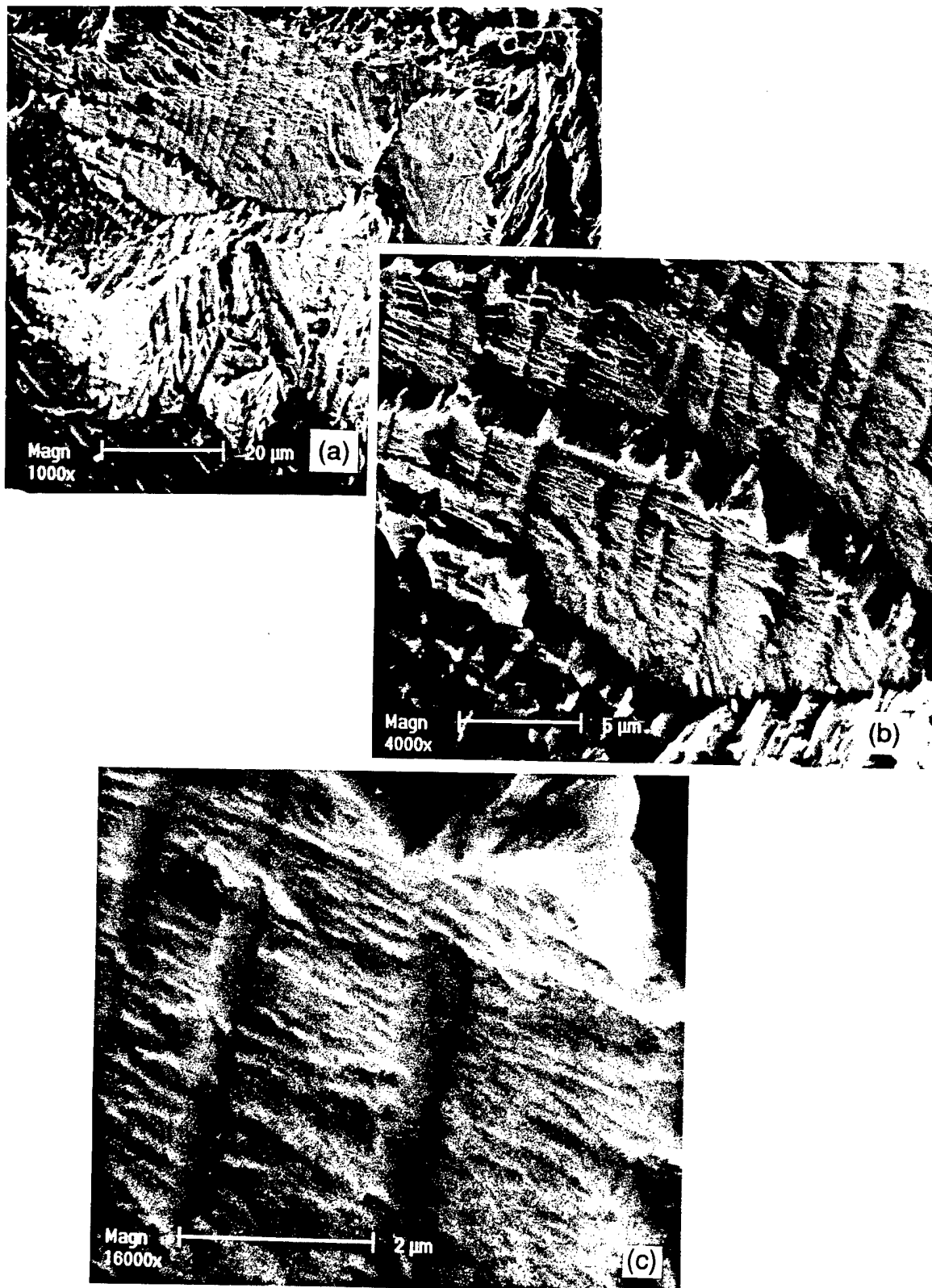


Fig. 16 Fractography from fully lamellar Ti-6Al-4V grown in vacuum at  $10^{-10}$  m/cycle. Crack growth direction was from bottom to top. (a) Overall fracture surface is very rough. (b) The edges of the lamellar structure are easily seen. (c) Fatigue striations parallel to the crack growth direction.

# **FATIGUE CRACK GROWTH AT HIGH R-RATIO IN Ti-6Al-4V at 1.5 kHz: THE EFFECT OF PERIODIC REMOVAL OF MEAN STRESS**

David L. Davidson  
Southwest Research Institute  
San Antonio, TX 78228

## **Abstract**

Fatigue cracks were grown under high mean stress at  $\approx 1.5$  kHz at rates of  $10^{-10}$  to  $10^{-12}$  m/cycle within the scanning electron microscope in vacuum. Periodically, mean stress was removed, then reapplied, and the effect on subsequent crack growth rate was measured. This process has been called HCF/LCF interaction. Detailed crack tip micromechanics analyses were made of these load interactions. The only HCF/LCF effect detected was less than a factor of ten change in crack growth rate, in agreement with expectations from the micromechanics analysis, and previous experimental results in air.

## **Introduction**

The components of gas turbine engines operate at high mean stresses due to the centrifugal loads caused by high rotational speeds. The turbine blades also have vibratory stresses that are superimposed on the mean stresses. Any fatigue problems that are experienced by turbine blades are driven by the vibratory stresses, but fatigue phenomena are also well known to depend strongly on mean stress effects. The mean stress in a jet engine blade increases when the engine is started and the aircraft takes off, maneuvers, and lands, and then decreases to zero while the engine is turned off. The question is "what is the effect of changes in mean stress on fatigue phenomena caused by vibratory stresses."

The experiments described in this paper were designed to determine what effect periodic removal of mean stress has on fatigue cracks that are growing under low vibratory stress amplitudes (low  $\Delta K$ ) at high R ratio (high mean stress).



## Material

The material used was forged and heat treated Ti-6Al-4V giving a microstructure similar to that shown in the ASM Handbook of microstructures [1], #2729, which consists of equiaxed shaped alpha grains approximately 6  $\mu\text{m}$  in diameter. The alpha grains (hcp) are mainly separated by discontinuous sheets of beta (bcc); beta is also found in the triple point regions. Estimates of the volume fraction of beta range from 5 to 15%.

## Experimental Procedure

A unique loading stage that fits within the scanning electron microscope (SEM) was used to grow the fatigue cracks, and all cracks were grown in the vacuum of the SEM, about  $10^{-7}$  torr. The high resolution and depth field of the SEM allowed accurate crack length measurement and photographs of the crack tip region to be made. The loading stage allowed application of tensile vibratory loads at about 1.5 kHz. Mean tensile load was applied by a hydraulic system. This device has been described in more detail previously [2].

Fatigue cracks were initiated at notches and grown to lengths beyond the influence of the notch. As the crack lengthened, cyclic and static loads were incrementally lowered until crack growth rates were in the  $10^{-10}$  to  $10^{-12}$  m/cycle range, for  $R$  (= minimum load/maximum load) ratios of 0.6 to 0.85, by the time the crack was 2 to 3 mm long. Cracks were found by fractography to have nearly semicircular shapes at all crack lengths up to back face penetration. The values of  $\Delta K$  (cyclic stress intensity factor) for cracks growing under these conditions are in the 2 - 6  $\text{MPa}\sqrt{\text{m}}$  range.

After obtaining low and steady crack growth rate, the mean stress was periodically removed. This is often considered to be the imposition of "low cycle fatigue (LCF). Intervals of cyclic loading of either  $10^5$  or  $10^6$  cycles were used between each unload (UL) or LCF event. The condition of no load was maintained for about 5 min. before returning to the previous mean load and continuation of cyclic loading. From experiments with this protocol, the effect of periodic decreases in mean load on crack growth rates could be determined. Because surface cracks were being observed, measurements were obtained from each end of the crack, labeled End A and End B.

The micromechanics of this periodic unloading process were examined by performing detailed analyses of the response of the material surrounding the crack tip that resulted from changes in the mean and cyclic loads. The hydraulic system was used to impose the maximum and minimum cyclic loads, and vary the mean loads. Photographs of the crack tip region were made at each step in the loading sequence. The DISMAP system [3] was used to measure material response, i.e., the displacements, resulting from load changes, and from displacements, axial and shear strains were computed. After the imposition of a mean load decrease, the previous mean cyclic loads were again imposed, and the crack growth rate, crack opening load, and crack tip micromechanics were again determined to see what changes occurred with subsequent growth of the crack.

## Results

Because of the large number of analyses required for each examination of an unloading sequence, only a few complete analyses were made. Each analysis resulted in a similar material response at the crack tip, but, there were some differences between results, presumably caused by slight variations in local microstructure, as well as differences caused by the fatigue process [4].

Part of a crack length vs. number of loading cycles record from one of the experiments is shown in Fig. 1. Derived average crack growth rates in the steady state growth period before and during LCF cycling are shown in the figure, as are the locations of detailed analyses.

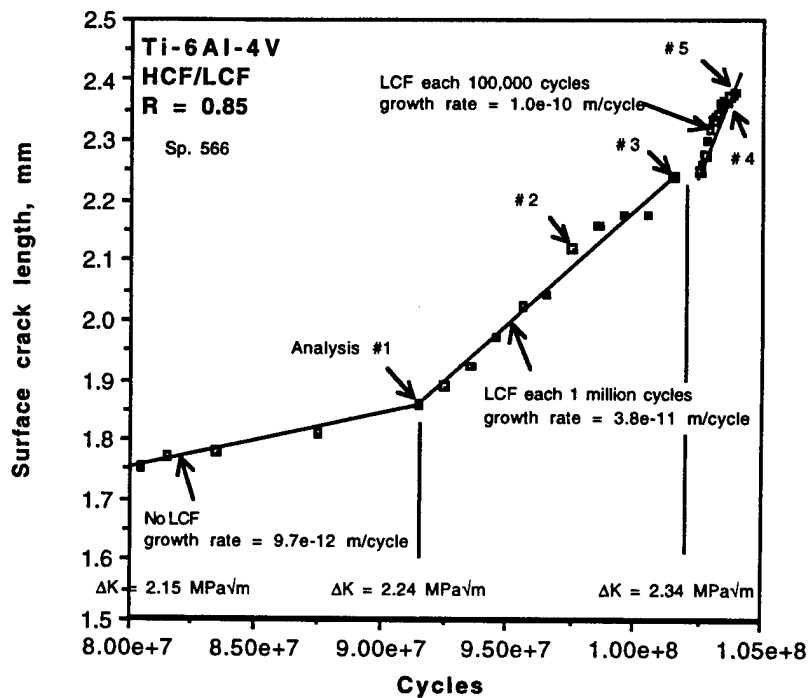


Fig. 1 A history of the crack length changes with and without the periodic removal of mean stress (LCF). Average fatigue crack growth rates and applied  $\Delta K$  are shown in the figure. An example of increasing crack growth rates with periodic LCF.

A loading sequence history is shown in Fig. 2 for one of the micromechanics analyses. The numbers indicate where photographs were made. Strains were determined from measuring the displacements that resulted from changes in stress. Just prior to the removal of mean load, the crack opening load and the strains caused by cyclic load amplitude were determined. Next, the strains that resulted from mean stress removal was determined. Third, the strains related to reimposition of mean stress were measured, as was the opening load on the first cycle after mean stress removal. Finally, the strain due to cyclic load was determined after reimposition of mean

stress. Then, after application of some thousands of cycles, the crack opening load and crack tip strain response were again measured.

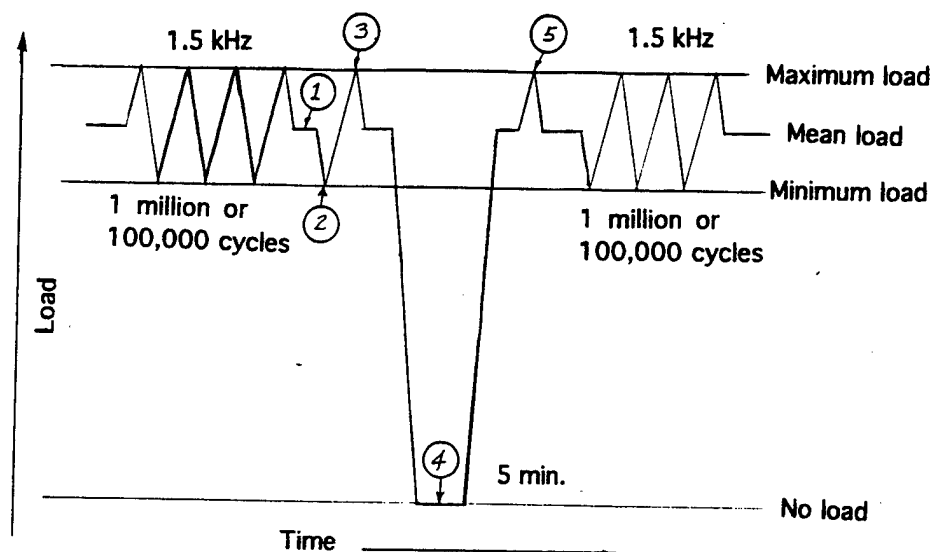


Fig. 2 Load history for the detailed measurement of crack tip micromechanics caused by removal of mean stress. Circled numbers indicate conditions at which photographs were made for analysis of strains.

Shown in **Fig. 3** are the results of analyzing the displacements in the crack tip region for strains. A cyclic stress strain curve under large strain conditions for this material has not been found, so measured crack tip strains are shown as a function of the remotely applied stresses, and the strains are listed in **Table 1**.

**Table 1**  
Crack tip response to LCF cycle

Loading condition	Crack growth rate m/cycle	Change in maximum shear strain
Cyclic	$3 \times 10^{-11}$	0.032
Unload (UL)	--	-0.030
UL + 1 cycle	--	0.033
UL + 20 kcycles	$10 \times 10^{-11}$	--
UL + 150 kcycles	$8.5 \times 10^{-11}$	0.026

The locations of the "start" and "end" of the analyses are shown to help guide the discussion of this result. The range of maximum shear strain (0.032) caused by cyclic loading at high mean stress prior to mean stress removal is shown between solid circles. This change in strain was assumed to be equally partitioned between tension and compression because the opening load was approximately half of the cyclic load. The effect of removing the mean stress is shown by the solid circle at "start" and that at zero applied stress. Reloading to the mean stress was

assumed to occur with a modulus of  $G$ , and the deformation that occurred returned the strain to approximately zero.

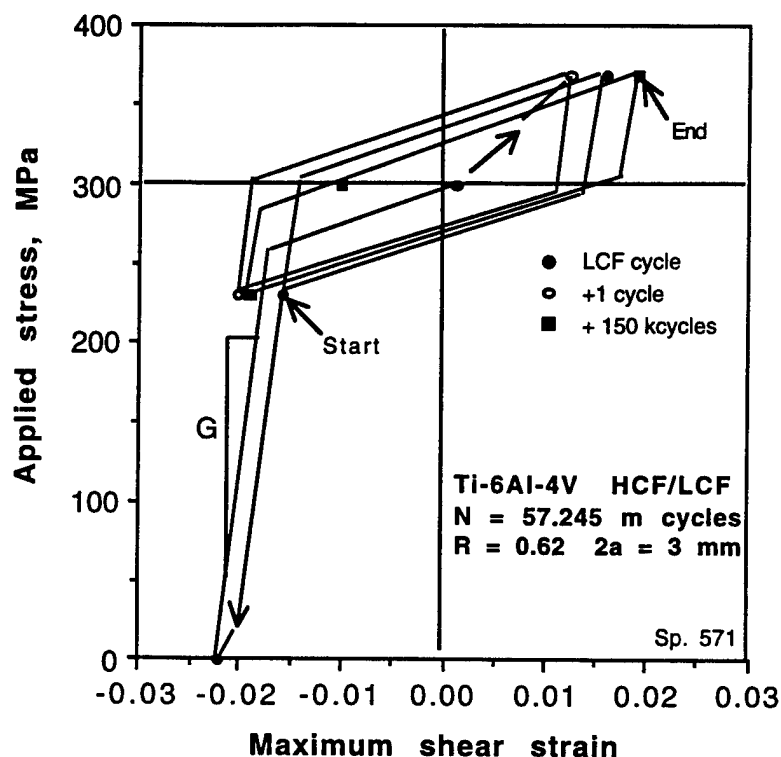


Fig. 3 Remotely applied stress vs. locally measured strains for loading before, during and after removal of mean stress.

The strain change on the initial loading cycle after reimposition of the mean stress (0.033) was very nearly equal to the strain range before removal of the mean load. After 150,000 loading cycles, the strain range (0.026) decreased, compared to the initial strain range (0.032).

Fatigue crack growth rates before the LCF, averaged over 20 kcycles after the LCF, and over another 150 kcycles are shown in the table. Compared to the crack growth rate before the LCF, the crack growth rate initially increased, but then decreased with subsequent cycling.

The crack growth rate history shown in the table indicates some increase caused by mean stress removal while the changes in strain at the crack tip indicate that little change in growth rates would be expected. A second record of crack length as a function of cycles is given in Fig. 4. This record shows crack growth rates decreasing after the LCF cycle, contrary to Fig. 1.

The results of another analysis of material response caused by mean stress removal is shown in Fig. 5. This history is more difficult to follow than that shown in Fig. 2, but the result is essentially the same, except that the growth rate after mean stress removal decreased contrary to expectations from the increase in crack tip strain range.

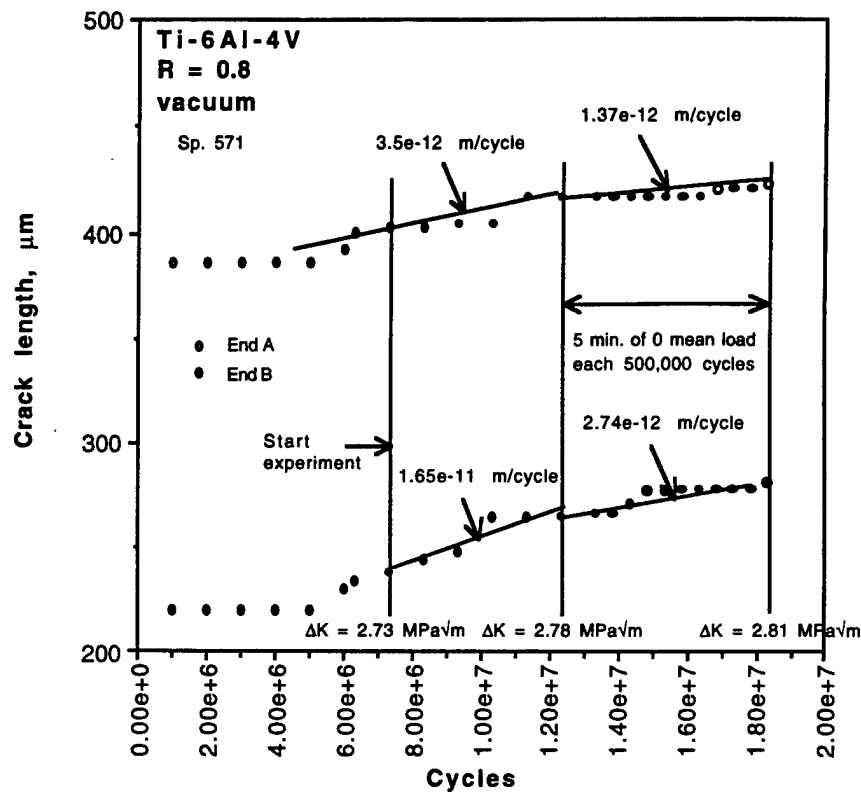


Fig. 4 A history of the crack length changes with and without removal of mean stress (LCF). An example of decreasing crack growth rates with periodic LCF. Compare to Fig. 1.

Stereoimaging of photographs made at minimum load vs. those made with increasing load showed that the crack at the tip was closed at minimum cyclic load, and that it took about half the cyclic load to peel it open to the tip at  $R = 0.6$ . At  $R = 0.85$ , crack opening loads were usually lower and sometimes the crack was fully open at minimum load. After the LCF cycle, measurement of crack opening load indicated that opening load sometimes decreased and sometimes increased. There was no systematic change in opening load level; thus  $\Delta K_{\text{effective}}$  and subsequent growth rates did not correlate, as was envisioned prior to these measurements.

A summary of the results of crack growth rates measured before and after removal of mean stress at various  $R$  ratios and  $\Delta K$  values is given in Fig. 6 for both ends of the crack. Open symbols indicate crack growth rate before the LCF cycle, closed symbols, the growth rate afterwards. These data show no systematic trend.

### Discussion

The lack of a systematic trend in the crack growth data and crack tip micromechanics analysis could be due to problems with experimental technique, variations in microstructure, or maybe there is just very little effect of the LCF cycle. Prior to the initiation of an extensive testing

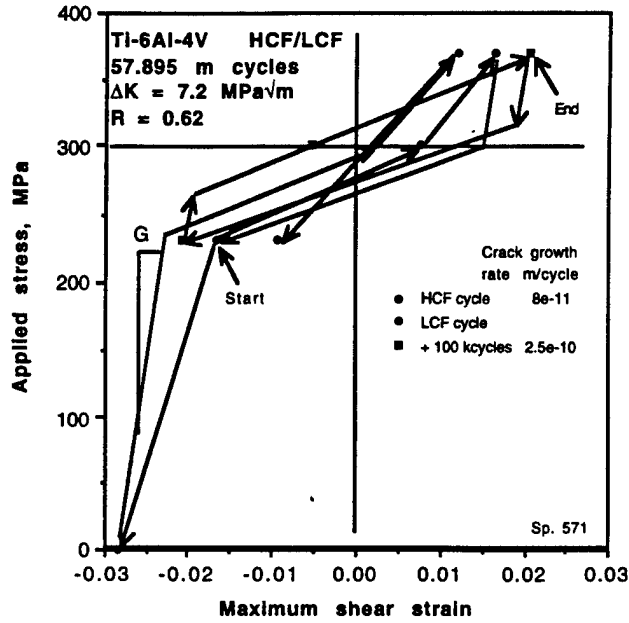


Fig. 5 Remotely applied stress vs. locally measured strains for loading before, during, and after removal of mean stress.

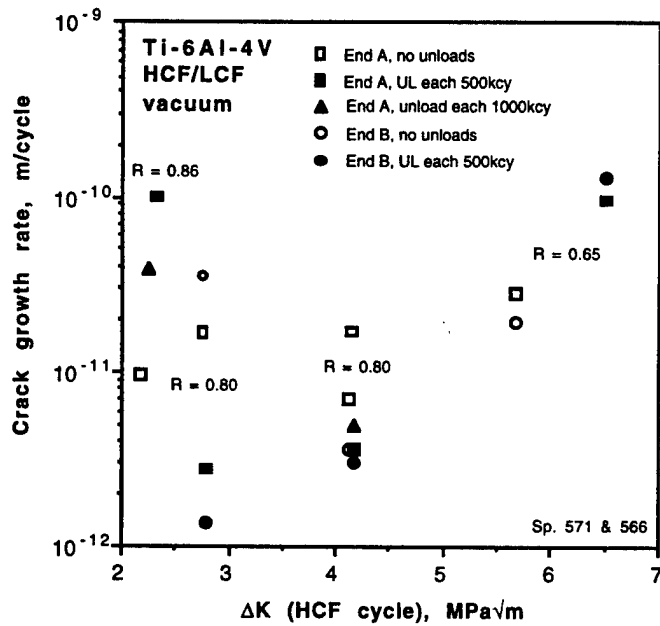


Fig. 6 A summary of the effects of mean stress removal on crack growth rates. The variables are:  $\Delta K$ , R-ratio, and frequency of unloading (UL) or mean stress removal.

program using standardized conditions to gather more data that might show a trend, the present data were compared to those taken previously by Powell, Duggan, and Jeal [5], the only other similar investigation known. Their data were not obtained using the same experimental protocols as used here, but their results are comparable. No data are provided for cracks grown without LCF cycles, so data taken with an LCF cycle each 1 million HCF cycles was taken as the "base line" for comparison to LCF cycles each 1000, 10,000, and 100,000 HCF cycles.

The results of Powell, et al., are shown in Fig. 7, and the data of Fig. 6 are added for comparison. The Powell data do not show a systematic change in crack growth rate resulting from LCF, which is similar to the results of the present experiments. At higher  $\Delta K$ , the Powell, et al., data show an increase in crack growth rates with a decrease in the number of cycles between LCF, which is in agreement with present results. At lower  $\Delta K$  values, the Powell, et al., data indicate little or no change in crack growth rate, while present data also show little or no change, or both an increase and decrease in crack growth rate, but small changes in both cases (perhaps as much as a factor of 10).

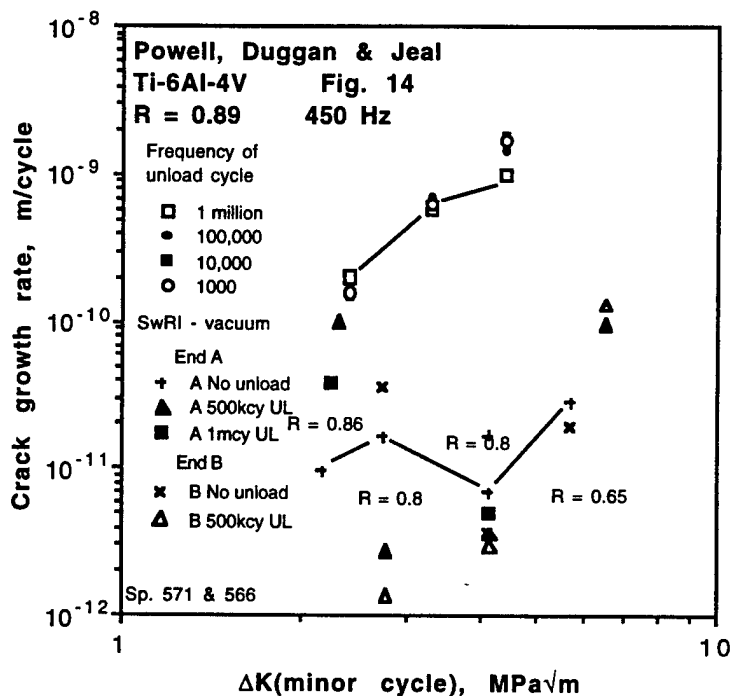


Fig. 7 The results of Powell, et al., for crack growth in air, graphed so that they may be compared to present results, for crack growth in vacuum.

Because the results are about the same in vacuum as in air, it can be concluded that the mechanism by which crack growth is increased by moist air has little effect on the crack tip micromechanics that describe the superimposed LCF effect.

## **Conclusions**

1. For fatigue crack growth at high R-ratio (high mean stress, low cyclic stress) in the near-threshold region of  $\Delta K$ , the periodic removal of mean stress (LCF) causes only a small change in subsequent crack growth rate.
2. Detailed crack tip micromechanics analysis of the effect of periodic LCF on HCF crack growth indicated that the effect would be expected to be small, in agreement with measurements of crack growth rate.
3. Although there is an effect of environment (air vs. vacuum) on the magnitudes of crack growth rate, imposition of LCF has about the same effect in both environments, as determined by comparison of present results with those of Powell, et al. [5].

## **Acknowledgements**

The technical assistance of Messrs. John Campbell and Jim Spencer in performing the experiments and analysis is gratefully acknowledged. This research was funded by Air Force Office of Scientific Research Contract F49620-96-C-0037, part of the initiative on High Cycle Fatigue, Capt. C.H. Ward, contract monitor.

## **References**

1. ASM Handbook, v.7, 8th Ed., 1972, p. 329.
2. D.L. Davidson, A. Nagy, and T.S. Owen, High Cycle Fatigue of Materials, W.O. Soboyejo, et al. eds., TMS, Warrendale, PA, 1997, pp. 263-268.
3. E.A. Franke, D. Wenzel and D.L. Davidson, Review of Scientific Instruments, 1991, v. 62, pp. 1270-1279.
4. D.L. Davidson and J. Lankford, Int. Materials Revs., 1992, v. 37 (2), pp. 45-76.
5. Powell, Duggan, and Jeal Int. J. Fatigue, 1986, v. 12, pp. 345-350.



## **FATIGUE CRACK GROWTH IN AN AEROENGINE DISK LUG DUE TO BLADE ATTACHMENT**

David L. Davidson  
Southwest Research Institute  
San Antonio, TX 78228

### **ABSTRACT**

Cracks that were found in the disk-blade attachment area of a titanium alloy aeroengine compressor disk were characterized metallographically and fractographically. A recently published analytical model of fretting fatigue based on fracture mechanics was used to estimate the number of cycles required for the growth of these cracks. The analytical model indicated that the crack initiated under low cycle conditions, but may have grown to a length of several mm under high cycle fatigue conditions. The low cycle fatigue was probably caused by sliding between the blade and disk due to large changes in engine speed. However, if the crack grew under high cycle conditions, it could only be due to blade-gas stream interactions, perhaps with the blade in a resonance condition. Fractography supported only crack growth under low cycle fatigue conditions. The complexity of determining the cause of disk lug cracks was highlighted by this research.

### **INTRODUCTION**

Fretting is a phenomenon that can cause cracks to form when two parts of a machine are contacting, but moving with small relative displacement relative to one another. Recently, an analytical model was published that approached fretting fatigue from a fracture mechanics perspective and tied that analysis to fretting fatigue cracks that had been grown in the field and in the laboratory [1]. As is well known, fretting fatigue cracks are characterized by initiation from the surface with growth at an angle of  $\approx 45^\circ$  to the surface to some depth where the angle of the crack changes to closer to  $90^\circ$ . Angled crack growth initially predominates because of surface tractions imposed by the mating part, and perpendicular crack growth dominates when the surface tractions have been sufficiently diminished with depth.

The purpose of the present paper is to apply the analytical model to an aeroengine disk - blade attachment that failed in service for the purpose of determining the number of cycles that were required to cause the failure. This assessment of cyclic lifetime is important because from the number of cycles required to grow the crack, it can be determined if the

cracking occurred under conditions that can be typified as either low cycle or high cycle fatigue, and this understanding can be used to guide laboratory experiments intended to help understand this gas turbine engine failure mode.

## CHARACTERIZATION OF CRACKS

The blade attachment to a typical aeroengine disk is shown in **Fig. 1(a)**. This drawing is similar to the diagram in Fig. 1 of ref. [2]. In **Fig. 1(b)** the disk side of the plane of contact between the disk and the blade (the attachment surface) is shown, and the location of a crack that was found is indicated. The crack was about 1 mm from the edge of the disk on the inlet side, but only about 10  $\mu\text{m}$  from the bottom edge of the attachment plane. Considerable wear was found to have occurred in the vicinity of the crack location. This wear was similar to that shown for the laboratory study of ref. [2], and may be seen in **Fig. 2**, which also shows a surface view of the entire crack.

Several cracks at similar locations were found in several aeroengine disks, but only two of the cracks were analyzed in some detail. Two metallurgical cross-sections of the disk attachment area were made at the locations shown in Fig. 2. Two cracks were found on the first cross-section, as seen in **Fig. 3(a)**, but only one crack was found on the second cross section, **Fig. 3(b)**. Multiple cracking is typical of fretting fatigue failures. These sections reveal the microstructure of the Ti-6242 titanium alloy (Ti-6Al-2Sn-4Zr-2Mo, wt.%) disk alloy. Spherical 5  $\mu\text{m}$  average diameter alpha grains are embedded in a matrix of alpha - beta lamellar material. Widths of the alpha laths and the separating beta are about the same. The average lath width, as measured at several locations, was 0.545  $\mu\text{m}$ . The mating blade was probably made from a similar titanium alloy.

The widely open, 28  $\mu\text{m}$  long crack in the first cross-section contained debris, while the other crack is tightly closed and about 46  $\mu\text{m}$  long. Debris was also found in the fretting fatigue cracks of ref. [2]. Careful examination of these sections indicated that the path of these cracks was independent of microstructure, traversing alpha and beta plates without preference. Thus, the hypothesis of [2] that fretting fatigue cracks initiated in material at the surface that was transformed entirely to alpha by the fretting action is not supported by present results. Examination of the cross-section showed that if that process had occurred, it would have to be within the deformation zone at the surface found to be about 1  $\mu\text{m}$  deep. Due to the effect of excess electron emission near an edge, the microstructure within one micrometer of the

surface has not been imaged with sufficient clarity to determine the microstructure at that location.

The laboratory produced cracks in [2] initiated at angles of 35 to 55° to the surface. Similarly, the cracks in cross-section 1 originated on the surface at an angle of 35° to the surface, but grew only 2.5  $\mu\text{m}$  on that plane before beginning the transition to a plane approximately perpendicular to the surface. That transition was complete at a depth of 7.5  $\mu\text{m}$  and subsequent growth averaged 80° to the surface plane. The longer crack seen in the second cross-section, grew at an angle of 55° to the surface to a depth of  $\approx 9 \mu\text{m}$  then turned and grew at an angle of about 77° to the surface to a depth of about 44  $\mu\text{m}$ .

From other aeroengine disks a crack, similar to that shown in Fig. 2, but longer, was found in one of the attachments. Since surfaces of this crack were undisturbed, it was possible that fractography might reveal the mechanism of fracture. Thus, the attachment was separated from the disk by abrasive water knife, and metal was carefully cut away from the remaining part of the attachment. Ultimately, the surface farthest from the crack was ground until the presence of the crack was observed. The remaining ligaments were broken and the fracture surface revealed. Only one of the fracture surfaces was examined.

A light microscopy image of the fracture surface is shown in Fig. 4. All the crack arrest marks lead to one location where the crack initiated. The number of crack arrest marks were measured from this figure and it was determined that the spacing averaged 24  $\mu\text{m}$  per arrest, independent of the distance from the origin. However, a dark band is apparent along the attachment surface. Examination by secondary electron imaging showed that this dark band consisted of the debris seen in the cross-sectional views of similar cracks, Fig. 3. The material appeared similar to the geological description of material often found along stream beds. It consisted of a "conglomerate" of particles embedded in an amorphous-looking background. Clearly, this was debris from the galling process shown in Fig. 2. Energy dispersive x-ray microprobe showed that the debris consisted of Ti, Al and O and small amounts of Zr, Mo, Sn, and Fe, indicating the debris was mostly titanium oxide.

Most of the debris found on the fracture surface was removed by cyclic cooling and heating of the fractured specimen. It was alternately cooled in liquid nitrogen and allowed to heat to ambient temperature 20 times. The theory evoked was that differences in coefficient of thermal expansion between the debris and the metallic fracture surface would cause the oxide to spall from the metal. Once cleaned of oxide, the fracture surface appeared as shown in Fig. 5. This photograph was made

0.41 mm from the origin of the crack at the surface. The parallel bands shown on the right side of figure average  $0.4\text{ }\mu\text{m}$  per band and are probably not fatigue striations; i.e., crack arrest markings, because the lamellar matrix of this microstructure, Fig. 3, had a spacing of  $0.54\text{ }\mu\text{m}$ , and the spacing is highly regular, as are the lamellae spacing. However, more "striation-like" topographic features may be seen in the center of this figure. The average spacing of these bands is  $8\text{ }\mu\text{m}$ , and the spacing is less regular, as is typical of fatigue striations.

## ANALYSIS

Loading on contact surface between blade and disk is a complex matter and not easily analyzed. Contact surface loading comes from two sources: (1) the forces required to resist the centrifugal forces on the blade caused by rotation of the disk, and (2) blade vibrations, particularly under resonance conditions. The forces required to retain the blade are only cyclic when engine speed is changed, so the frequency is low, but the vibrational forces caused by blade interaction with a nonuniform gas stream are cyclic at roughly 1 kHz under steady turbine speed conditions.

The contact surface is  $45^\circ$  from the direction of the radial centrifugal force on the blade. The attachment region of the disk is not constrained by hoop stresses, because of the blade slots. Thus, the disk attachment slots expand when the turbine speed increases, with the result that the blades slide outward along the contact surface. Conversely, when the rotational speed of the turbine decreases, slot width contracts, and the blade is forced to slide in the reverse direction relative to the disk. The magnitude of the sliding is estimated as approximately  $50\text{ }\mu\text{m}$ . The normal and tangential forces acting on the contact surface are thus cyclic as the engine speed increases and decreases. Complicating analysis of the stresses acting on the contact surface is the friction between blade and disk. The friction coefficient is not well known even when the blade and disk have just been assembled because of various surface treatments and lubricants that are used in the assembly process. Friction also changes with time due to wear of both blade and disk.

The number of loading cycles caused by increases and decreases in engine speed are relatively small compared with the number of cycles that might result from gas-blade excitation. Thus, when a disk cracks, it is worthwhile to determine whether it was caused by the relatively low cycle conditions of turbine speed change or the high cycle conditions of gas-blade interactions and resonances.

The factors listed above make stress analysis of the disk blade-

interaction quite difficult and imprecise. However, it is clear that both normal and tangential forces are acting on the contact surface, and that it is this biaxial field that causes cracks to initiate and then grow, initially, at an angle to the contact surface.

The analysis of [1] starts by computing the Mode I and Mode II stress intensity factors for a crack growing at an angle  $\phi$  to the surface. It is then assumed that the crack will grow normal to the Mode I stress, making the Mode II stress intensity factor zero. This result links the ratio between the tangential and normal stress to the angle between the crack plane and the contact surface.

As the crack grows away from the surface, the effect of the tangential surface force decreases, so the crack will reorient itself more normal to the tensile stress that acts parallel to the contact surface. The analysis [1] then asserts that "If at the critical distance  $l_c$ , the tensile opening stress intensity factor due to the applied loads is larger than the effective Mode I threshold stress intensity factor range,  $\Delta K_{th}$ , the crack would reorient itself normal to the uniform applied stress and would continue to advance into the substrate in Mode I. Otherwise, the crack would arrest completely." This assumption provides a way to use  $l_c$ , the length of the crack at the location where it changes direction, as measured from Fig. 1, together with  $\Delta K_{th}$  for the Ti-6242 alloy, to derive the magnitude of the (implied) uniform applied stress range,  $\Delta\sigma_{app}$ , using eqs. 40 of the analysis [1]. The stress intensity factor for the crack, which is assumed to be a microstructurally small crack, can then be computed using the equation

$$\Delta K = 1.12 \Delta\sigma_{app} \sqrt{(\pi l)} \quad (1)$$

where  $l$  = actual length of the crack. The assumption of a microstructurally small crack appears to be fully justified by the cracks found in one of the disks examined, Fig. 3.

The number of cycles required for growth of the crack from surface to depth  $l_c$  is then easily computed by integration of the  $da/dN$  (crack growth rate) -  $\Delta K$  curve. It should be noted that the  $da/dN$  -  $\Delta K$  curves for small (surface) cracks do not have a  $\Delta K_{th}$ , while the curve for a crack large relative to the microstructure does exhibit a  $\Delta K_{th}$ . Therefore, the angled crack growing from the surface is a small crack, but once the crack reaches a depth of  $l_c$ , it becomes a large fatigue crack and exhibits a  $\Delta K_{th}$ .

This use of different  $da/dN - \Delta K$  curves for small and large fatigue cracks is required to be consistent with the analysis, and the inclusion of a  $\Delta K_{th}$  affects the results considerably, as will be seen. In this regard, the present analysis differs with that of [1] where the number of cycles can be determined analytically when the  $da/dN - \Delta K$  curve has no value of  $\Delta K_{th}$ .

The present analysis makes use of the fact that an effective value of the cyclic stress intensity factor,  $\Delta K_{eff}$ , can be used to describe the growth of large fatigue cracks, where

$$\Delta K_{eff} = \Delta K - \Delta K_{th} \quad (2)$$

Numerical integration was performed in 20 steps between  $l_c$  and the final crack length,  $h_c$ . To determine the difference in not assuming that the  $da/dN - \Delta K$  curve has a  $\Delta K_{th}$ , the crack growth rate curve excluding  $\Delta K_{th}$  was also integrated.

The largest unknown in computing the number of cycles for crack growth is the magnitude of the normal stress. The experiments of [2] used a value of 160 MPa for this stress, but for the disk design of the present aeroengine, this stress is thought to be closer to 350 MPa. These estimates were derived for disk-blade interactions due to speed change and do not include any blade-gas interaction forces.

## RESULTS

Measurements of crack lengths and angles from the metallographic analysis were rounded in making the analysis. Values used in computing the number of cycles to form the crack shown in Figs 1 and 2 are given in **Table 1**.

**Table 1**  
Parameters used in the calculation

Angle of initial crack to surface, $\phi = 55^\circ$
Critical crack length, $l_c = 20 \mu m$
Final crack length, $h_c = 50 \mu m$
Small crack: $da/dN$ (m/cycle) $= 1 \times 10^{-7} \Delta K^{1.35}$
Large crack: $da/dN$ (m/cycle) $= 1 \times 10^{-14} \Delta K^{6.22}$
$R = 0.1$ $\Delta K_{th} = 3.7 \text{ MPa}\sqrt{m}$

Analysis reveals that  $R$  (min. stress/max. stress)  $\approx 0$ , so the large crack growth rate curve for  $R = 0.1$  was chosen from [3] for a Ti-6Al-4V alloy of

microstructure similar to that seen in Fig. 1. The value of  $\Delta K_{th}$  was estimated from various recent results [4], but is assumed to be in error by  $\pm 0.2 \text{ MPa}\sqrt{\text{m}}$  to determine the sensitivity of this key parameter.

A crack growth rate curve for small cracks through material with the same composition and microstructure was not found, so data from a similar microstructure in the Ti alloy IMI 318 was used [4]. Other data on Ti-alloys was also considered, and there does not seem to be much effect of alloy or microstructure when it is a fine grained alpha - beta structure.

The results of the calculation are shown in **Table 2**.

**Table 2**  
Computed cycles to form crack

Assumed values		$N_1$ (sm. crack)	$N_2$ (lg. crack)	
$\Delta K_{th}$	Normal stress		with $\Delta K_{th}$	without $\Delta K_{th}$
$\text{MPa}\sqrt{\text{m}}$	MPa	cycles	cycles	cycles
3.7	160	20	$2.4 \times 10^7$	$2.6 \times 10^5$
3.7	350	7	$2.4 \times 10^8$	$2.6 \times 10^5$
3.5	160	20	$1.2 \times 10^8$	$3.6 \times 10^5$
3.5	350	7	$2.0 \times 10^8$	$1.3 \times 10^6$
3.9	160	20	$4.5 \times 10^6$	$9.5 \times 10^5$
3.9	350	7	$7.6 \times 10^7$	$2.4 \times 10^7$

In Table 2,  $N_1$  represents the number of cycles to form the angled crack from attachment surface to  $l_c$ , while  $N_2$  is the number of cycles required to grow the crack from  $l_c$  to  $h_c$ . The calculation is made for two values of the normal stress across the contact zone. The higher value represents the stress change caused by going from engine off to full power, while the lower value might represent a blade resonance condition.

## DISCUSSION

The results shown in Table 2 indicate that the angled crack was grown under low cycle fatigue conditions, while the deeper, straight part of the crack was grown under conditions that could be considered as high cycle. As expected, the magnitude of the normal load affected the number of cycles to grow the angled crack, while the magnitude of  $\Delta K_{th}$  has a major

impact on the number of cycles to grow the large crack. The number of cycles required for crack initiation were not estimated in this analysis.

Changing the  $da/dN-\Delta K$  curves for both large and small cracks within the bounds of likelihood for this alloy changes the numerical result, but does not alter the conclusions regarding the conditions under which crack growth occurred.

The roughness of the surface from which the crack started is apparent in Fig. 2. An oblique view of the contact surface, shown in Fig. 6, which was taken from the cross-section of Fig. 3 shows that considerable material was removed from the contact area, leaving the roughness apparent in Fig. 2. Measurements indicated that the contact surface had receded about 50  $\mu\text{m}$  by this wear process. Measurements of the lengths of gouges in the attachment surface, see Fig. 7, indicates that the relative movement between disk and blade was 100 to 200  $\mu\text{m}$ , and that the direction was approximately parallel to the plane of the disk. A relative motion of this magnitude could only have come from the blade-disk interactions that occur during engine speed changes, and not from gas-blade or resonant condition loadings.

The magnitude of material removal found, about 50  $\mu\text{m}$ , was not caused by fretting. The mechanism for this level of material removal was abrasive wear, or galling.

The large magnitude of the surface roughness and the evidence of material removal supports the result from the analysis that the crack initiated under low cycle fatigue conditions. It is hypothesized that the crack initiated due to the stress concentration caused by increased surface roughness or from the increase in stress that resulted from material removal, or both. However, cracks nucleating from the attachment surface may have been removed periodically by the wear process; thus, the initiation phase of cracking may have been delayed significantly by attachment wear.

The analysis indicated that a large number of cycles ( $\approx 10^7$ ) were required for the crack to grow from the critical depth (20  $\mu\text{m}$ ) to the final depth (50  $\mu\text{m}$ ). This large number of cycles could only have come from blade-gas interactions, possibly under resonance conditions.

Fractography of the disk crack supports crack growth under low cycle fatigue conditions. Due to debris crammed into the crack that covered the fracture surface and could not be removed, it was not possible to examine the fracture surface closer than 0.5 mm from the origin, so the



fractography was not conclusive. However, the fractography of fatigue cracks through Ti-6Al-4V grown under high cycle fatigue conditions in the laboratory under Mode I loading look nothing like the fractography from this lug. Fracture of the alpha phase is quite clear in the laboratory grown specimens, but are not seen in fractography from the lug, even though from the metallurgical cross-section it is clear that they should have been.

In the region between 0.5 mm and 2.7 mm from the origin, arrest marks were spaced about 24  $\mu\text{m}$ , and from the higher magnification fractography, it was estimated that there were about 8  $\mu\text{m}$  per striation. Using these growth increments in the equation that describes large crack growth, Table 1, gives  $\Delta K \approx 22 \text{ MPa}\sqrt{\text{m}}$ . For the number of striations measured, less than 1000 cycle were required to grow the crack 3 mm. Thus, growth would have been under low cycle fatigue conditions, in agreement with the analytical model in only the very early stages of crack growth.

## SUMMARY AND CONCLUSIONS

1. The analytical model of [1] was applied to a cracked aeroengine fan disk.
2. The angled part of the crack near the surface was determined from the analysis to have grown under low cycle fatigue conditions.
3. Fractography indicated that the crack grew under low cycle fatigue conditions from about 0.4 mm to the origin to a depth of about 3 mm.
4. The angled crack may have initiated and been grown under the influence of major turbine speed changes, i.e., under low cycle fatigue conditions.
5. At a depth of  $\approx 20 \mu\text{m}$ , the angled crack turned to grow perpendicular to the contact surface, and it grew to a depth of 50  $\mu\text{m}$  when the disk was removed from service.
6. Application of the analytical model indicated that the number of cycles required for the growth of this latter stage of cracking was  $\approx 10^7$  cycles.
7. The surface from which the crack grew was very rough, the result of wear that had removed  $\approx 50 \mu\text{m}$  of material from the disk-blade contact area. This failure mechanism should be termed galling rather than fretting. This level of wear may have removed crack nuclei, or it may have initiated the crack.

## ACKNOWLEDGEMENT

Application of the analysis and preparation of this manuscript was done under contract from Air Force Office of Scientific Research Contract F49620-95-C-0037. Metallurgical analysis of the aeroengine disk was accomplished under Air Force Contract F33615-96-C-5196. The estimate of the disk-blade cyclic stress from major turbine speed changes was made by Mr. Harold Simmons. The careful metallographic and microscope work of Byron Chapa was also an essential contribution to this work. Dr. O. Rader at U. Cal. Berkeley opened the crack from which the fractographic analysis was made. Prof. C. Briant of Brown U. suggested the cyclic cooling as the method for removing the fracture surface oxide. Jim Spencer performed the EDX analysis. Helpful discussions were held with Drs. A. Giannakopoulos and T. Lindley about their model.

## REFERENCES

1. Giannakopoulos, A.E., Lindley, T.C., and Suresh, S., *Acta mater.*, 1998, 46, 2955-2968.
2. Antoniou, R.A., and Radtke, T.C., *Mat. Sci. Eng.*, 1997, A237, 229-240.
3. Chesnutt, J.C., Thompson, A.W., and Williams, J.C, "Influence of metallurgical factors on the fatigue crack growth rate in alpha-beta titanium alloys" Report AFML-TR-78-68, May 1978.
4. Bolingbroke, R.K., and King, J.E., *Small Fatigue Cracks*, R.O. Ritchie and J. Lankford, eds., The Metallurgical Society, Warrendale, PA, 1986, pp. 129-144.

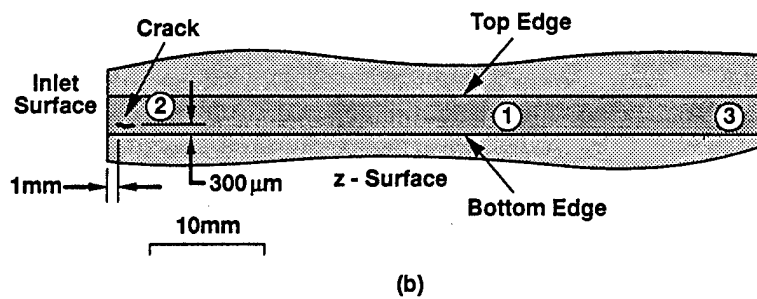
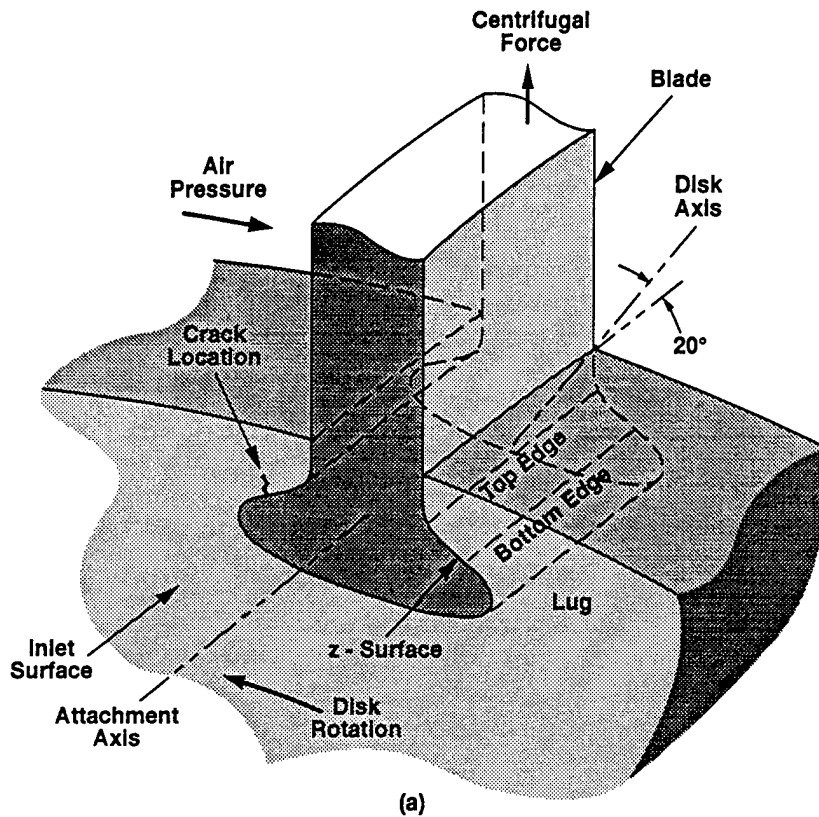


Fig. 1 (a) Illustration of the blade containment slot in the disk. (b) View of the contact area between blade and disk showing location of the crack.

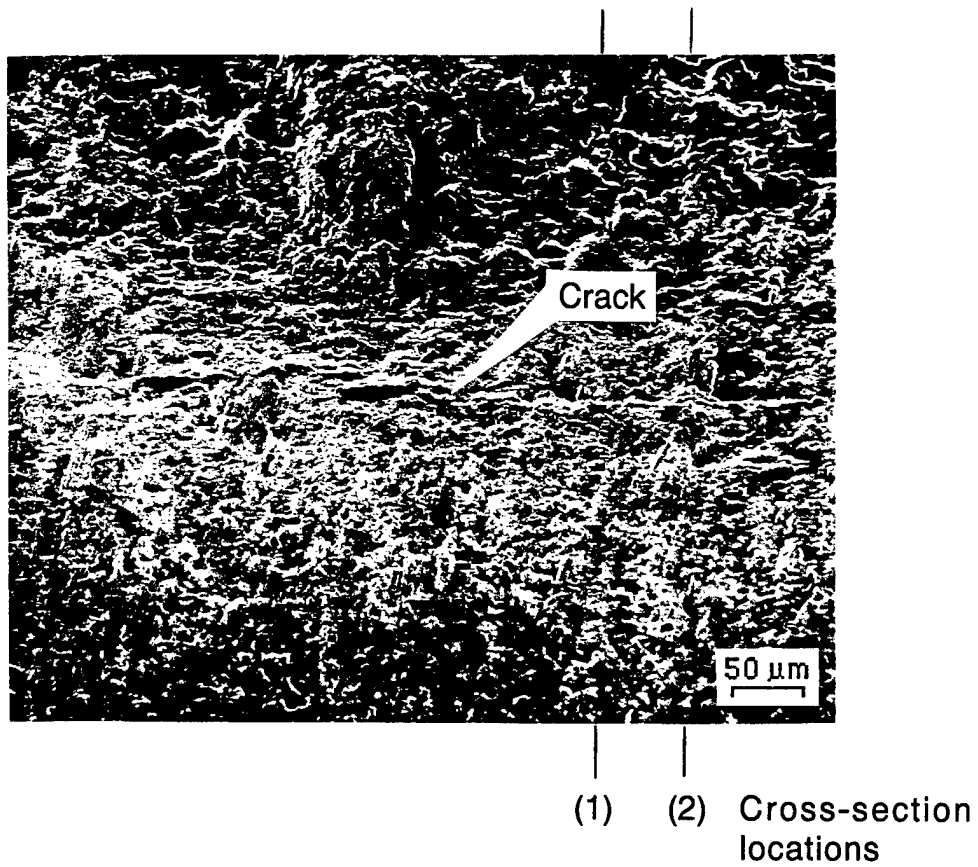


Fig. 2 View of the surface region of the contact surface containing the crack. The entire crack, although difficult to see, is shown in this photograph. Locations of the metallographic cross-sections of the crack are shown.

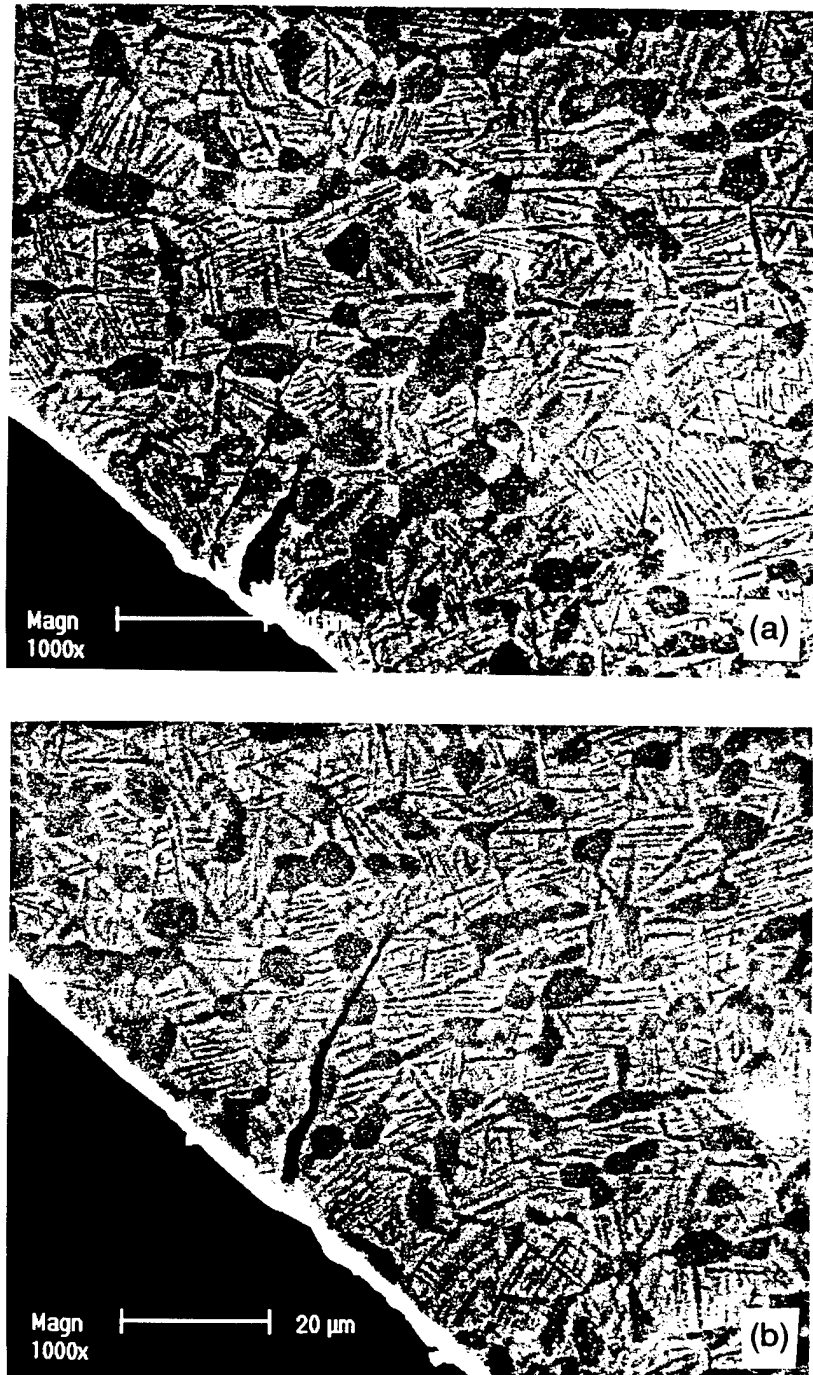


Fig. 3 Cross sections of the crack from the two locations shown in Fig. 2. (a) First cross-section, showing two cracks. The open crack is full of debris from the wear process. (b) Second cross-section with only one crack that also contains debris near the surface.

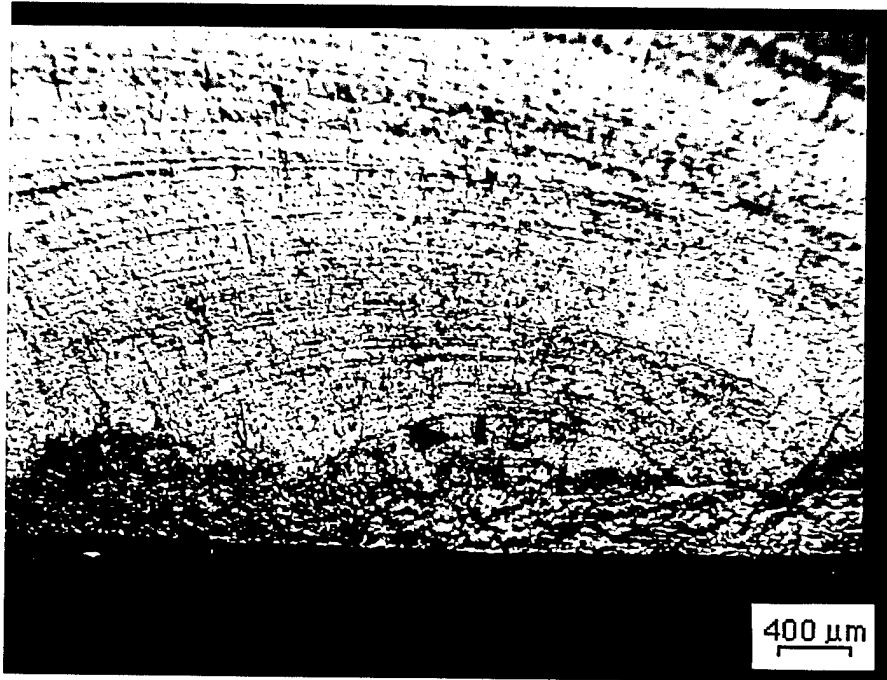


Fig. 4. Light optical view of an attachment disk crack fracture surface. The crack arrest lines are seen, as is the dark oxide covering the region near the crack origin (before cleaning).



Fig. 5 Secondary electron image of the fracture surface shown in Fig. 4 about 0.4 mm from the origin. The parallel lines on the right are probably not crack arrest marks (striations), because they are regular and scale approximately with the lath width of the microstructure ( $0.4\text{ }\mu\text{m}$ ). However, the irregular parallel marks in the upper center probably are striations that have a spacing of about  $8\text{ }\mu\text{m}$ .

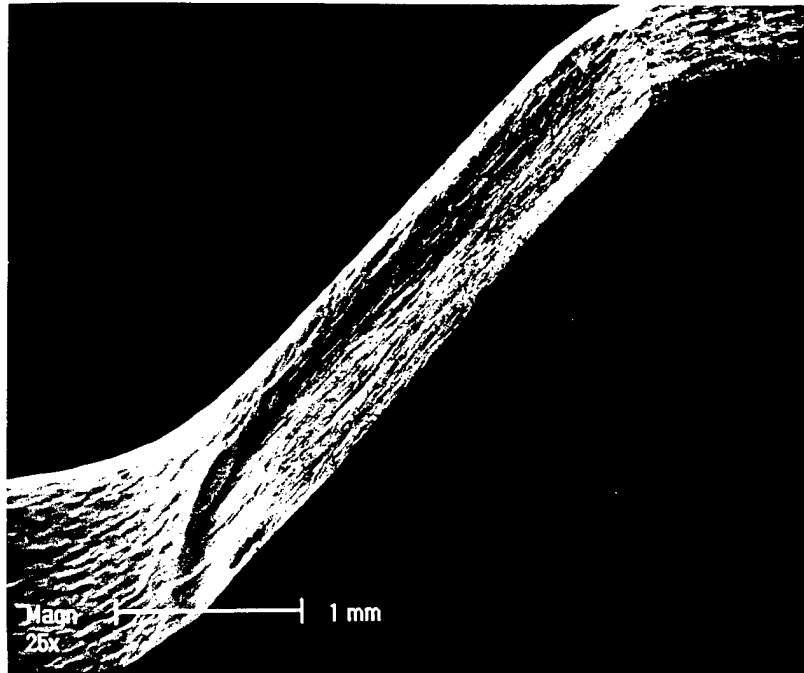


Fig. 6 Low angle view of the contact surface from the cross-section that shows the extent and depth of the wear scar. The crack is located near the point where the magnification bar crosses the edge of the cross-section.

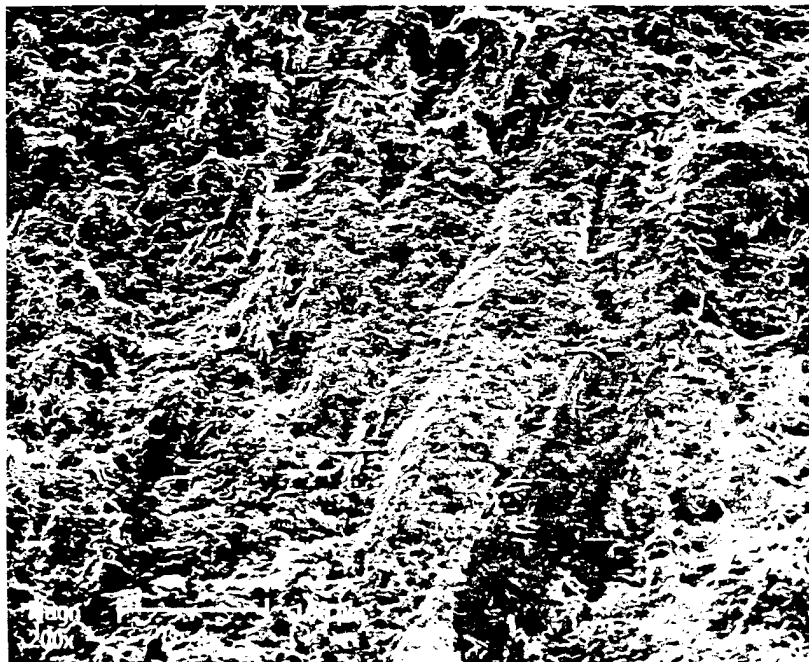


Fig. 7 Wear marks in the disk contact zone adjacent to the cracked area. The axis of the crack is horizontal, so the direction of the wear marks is approximately 80° to the axis of the crack and the blade containment slot.



## **ANALYSIS OF THE FORCES IN THE DISK-BLADE ATTACHMENT OF A GAS TURBINE AEROENGINE**

Harold Simmons and D.L. Davidson  
Southwest Research Institute  
San Antonio, TX 78228

### **ABSTRACT**

The forces on the disk-blade attachment in the fan part of a gas turbine aeroengine have been estimated using engineering analysis to assist in evaluating attachment failure processes. The static centrifugal forces that arise from increasing turbine speed actually increase as speed is reduced. Dynamic forces arise from blade resonances that might be excited by distortions in the axial airflow to the turbine inlet, such as could occur due to nacelle design or high speed aircraft maneuvers. The analysis shows that the dynamic forces could be a significant fraction the static forces caused by centrifugal loading.

### **INTRODUCTION**

Many gas turbine engines use a bladed disk type of construction. The fan, compressor and turbine sections of the engine consist of stages, where a number of disks are connected together to form rotors. Each disk holds 20 or more blades in the gas stream. The larger fan blades are attached to the disk by being inserted into a slot, or dove tail, in the disk as shown in **Fig. 1**. The axis of the slot, or attachment, is not necessarily coincident with the axis of the shaft that connects the disks. The angle between the shaft and slot is about  $20^\circ$  so that the plane of the airfoil and the slot have better alignment. The slot is slightly larger than the blade, and the sizing is such that when the disk is completely bladed, a slight motion of the blades is still possible. The disk has two flat bearing surfaces that engage the blade and counteract the centrifugal force of disk rotation. These bearing surfaces are frequently at an angle of  $45^\circ$  to the radial direction.

Although this method of blade-disk manufacture has been used successfully in gas turbine engines, one of the damage mechanisms that limits the lifetimes of the engines by producing cracks (**Fig. 1**) occurs

within the blade-disk attachments. Small relative motions occur between the disk and the blade that have two origins: (1) changes in turbine speed, and (2) blade vibrations excited by interrupted and non-axially symmetric gas flow through the turbine. The purpose of this paper is to present an analysis of the forces that are developed in the attachment. These forces may then be used in analyses of the failure mechanisms associated with the attachment for the accurate prediction of lifetimes.

## ANALYSIS

The blade-disk attachment shown in Fig. 1 is typical of those found in the fan and compressor sections of a military engine. The speed of the engine was assumed to be 7000 rpm when the aircraft is maneuvering prior to take off. During take off, the engine speed goes to full throttle  $\approx 10,400$  rpm and remains there during the climb part of the flight. Once at altitude, it is throttled back to cruising speed.

Changes in forces on the attachment are caused by increases in disk rotational rate due to start up and take off, and decreases in rotational rate to cruising speed. In the attachment, these forces are large, and the variations with rotational rate are large and would be the only forces if the blades were not also vibrating due to variations in air flow caused by the vane-wake disturbances and non-axisymmetric air flow.

The magnitude of blade vibrations is strongly dependent on the difference between the resonant frequency of the blade and the frequencies of vibration from excitation sources within the engine, such as the wakes of the stationary vanes. This difference is termed the frequency margin. Blades are designed to have large frequency margins for uniform air flow into the turbine. However, non-axisymmetric flow distortions often occur in aircraft gas turbine engines.

Normally blade vibrations are controlled by maintaining an adequate frequency margin; however, the margin may decrease during the life of the engine due to wear at the blade part-span shroud dampers and in the dove tail attachment, or due to changes in aircraft maneuvers that cause unexpected turbine temperatures and operating speeds.

Distortions in engine inlet air flow could occur from several sources.

Possible causes for variation in air flow are the shape of the engine nacelle and the relative position of the engine to the fuselage. For commercial aircraft, variations in inlet flow are small when the engines are remote to the fuselage, but military engines are usually integral to the fuselage which causes the intakes to be non-cylindrically symmetric. Also, the maneuvers of the aircraft can cause variations in the air flow pattern at the inlet. Military aircraft are designed to be highly maneuverable, so considerable variations in inlet air flow are expected.

## I. FORCES ON ATTACHMENT DUE TO ENGINE SPEED CHANGES

The outer edge, or rim, of the disk is cut to form the blade attachment slots; therefore, this part of the disk does not support tangential (hoop) stresses. Thus, centrifugal forces exerted on the disk by rotational speed increases cause the slot width to increase, which allows the blade to slip out a little. The magnitude of the rim growth per blade is shown in **Fig. 2**. Also, disk/blade temperature in the fan section of the engine changes from about 50 to nearly 800°F during a typical flight, but blade slippage will be dependent on the difference in temperature between blade and slot. The temperature difference would probably cause slippage of no more than about 0.00025 in.

Slippage of the blade in the disk is shown in **Fig. 3** for two conditions:  $\mu = 0$  (free-slip) and  $\mu = 0.5$ . As engine speed increases, the blade motion is envisioned to follow the lower curve until static friction is overcome, then to slip approximately to the center line in the figure ( $\mu = 0$ ), and this process would repeat itself, not quite reaching the center line because of dynamic friction  $> 0$ . As the engine speed decreases slippage would be reversed, but at higher values, as shown for the stick-slip condition between the upper line and the dynamic friction line, estimated to be near the line for  $\mu = 0$ . The magnitudes shown in the figure for slippage are estimates; values could be two to three times the values shown.

The forces on the disk, which are both normal and shear, as shown in **Fig. 4**, are altered by the movement of the blade because there is friction between the two. Also, the disk slot is essentially a wedge-shaped cantilever beam with distributed loads that exerts bending forces at the root of the slot. These bending stresses are shown in **Fig. 5** as a function of turbine speed. The blade and disk characteristics used for this calculation are given in **Table 1**.

**Table 1**  
Blade and Disk Characteristics

<u>Blade</u>	
Weight (lbs.)	0.45
Length (including attachment) (in.)	6.75
Chord (ave., in.)	2.62
Distance from tip to shroud (mm)	3.0
<u>Disk</u>	
Diameter (in.)	19
Blades per disk	40

Calculation of the normal and shear forces acting on the disk is inexact because the coefficient of friction ( $\mu$ ) between blade and disk is unknown. Free slip is the condition when  $\mu = 0$ , and when  $\mu = 1$ , the sliding force equals the normal force, which is usually considered as the upper limit of the friction coefficient unless galling occurs. The problem is made more complex by the fact that the coefficient of friction changes as the contact surfaces wear throughout the life of the engine. The contact surfaces are machined and then are often shot peened prior to assembly. Shot peening results in rough surfaces for both blade and disk that does not allow a uniform stress over the contact area. Thus, it has been necessary to estimate the coefficients of friction to perform the analysis.

The analysis computes the normal ( $F_n$ ) and shear ( $F_s$ ) forces on the attachment bearing surface in the disk as a function of the rotational speed of the turbine. For changes in engine speed, with  $\mu = 0$  and  $\mu = 0.5$ , the normal force on the disk attachment surface increases and decreases as shown in **Fig. 6**. The center line depicts the increase in  $F_n$  for the free-slip condition,  $\mu = 0$ . When  $\mu = 0.5$ ,  $F_n$  increases more slowly, as shown by the lower line. But the most likely condition is for the force to increase until the static friction coefficient is overcome, then for the blade to slip under a dynamic friction coefficient. This stick-slip mode is shown by the zig-zag line with arrows connecting the (lower) line for  $\mu = 0.5$  almost to the (center) line for  $\mu < 0.5$ , which is the dynamic value. Vibrations within the engine make it more likely that the blade will slip to the equilibrium location near the  $\mu = 0$  line.

When the engine decreases in speed, the maximum force on the disk attachment is shown by the upper line in Fig. 6. Force for a decreasing rotational speed is greater than for increasing speed because the blade is forced to slide back within the disk against the resistance of the centrifugal force. Changes in  $F_n$  as the engine decreases in speed from 10400 rpm under stick-slip conditions is depicted by the lines with arrows shown above the central line. Force would increase until static friction was overcome in the shrinking disk slot, then the blade would slip, and  $F_n$  would be relieved, somewhat as depicted by the arrows in Figure 6.

Changes in the sliding force  $F_s$  on the disk attachment surface are shown in Fig. 7 for increases and decreases in engine speed. The explanation for changes in  $F_s$  with increasing and decreasing turbine speed is similar to that given for  $F_n$  in Figure 6. Note that the lower line is an estimate for the slippage with a dynamic friction coefficient. Arrows show the changes in  $F_s$  under stick-slip conditions as engine speed changes.

The effect of friction on the normal and shear forces are shown for two turbine speeds, 7000 and 10,400 rpm, in Figs. 8 and 9. These speeds represent a typical speed range expected during operation. The two extremes are shown: with and without slip. Forces during operation under stick-slip conditions will fall between these extremes.

## II. FORCES ON ATTACHMENT DUE TO BLADE RESONANCES

The average air velocity through the engine being considered in this analysis is 400 - 500 ft/sec, and the axial flow throughout the engine remains the same. With a typical blade geometry, the tangential flow across the blade face is about 1400 ft/sec. The velocity distortion that could cause blade resonance has been assumed to be in the region shown in Fig. 10. This disturbance in the inlet gas stream, which is highly idealized, is assumed to have been caused by the geometry of the engine nacelle and airplane fuselage. The change in gas stream force on a blade due to the pressure variation caused by the inlet flow distortion is as shown in Fig. 11.

An axial flow distortion of 10 to 15% around the flow intake is typical of aircraft gas turbines. Some distortions due to the wakes of vanes

upstream from the blades occur, but a variation in dynamic pressure of only 1 to 2 percent is expected from this source.

The frequency content of the excitation depends on the nature of the flow distortion. For the condition shown in Figs. 10 and 11, the Fourier transform shown in **Fig. 12** provides the magnitude of excitation level at various multiples of running speed known as excitation orders. The blade experiences an oscillating load maxima at the third order, with smaller maxima at the 6th and 9th, etc., order.

In the analysis, maximum in the forcing function for blade oscillation of 66 lbs. was chosen, which corresponds to the sixth order term in the Fourier transform. The blade was designed to have a resonance at a frequency approximately 6 times the natural frequency of oscillation caused by vane wake distortions in air flow through the turbine without an inlet perturbation.

The frequency of blade vibration at different engine speeds is shown in **Fig. 13**, the Campbell diagram. Each line represents one of the multiples of the fundamental blade vibration frequency. From the Campbell diagram, at the maximum engine speed of 10400 rpm, the sixth order blade vibrational frequency is about 1000 Hz. Thus, the sixth order term in the Fourier transform translates to a frequency of about 1000 Hz, and this is the frequency of the forcing function for blade resonance at an engine speed of 10400 rpm. These conditions amount to an approximately "worse case" condition for blade resonance loading of the disk attachment, which could possibly lead to fatigue crack initiation and growth in the disk lug.

Using the assumptions given above, the loads on the disk attachment surface caused by blade resonance can be computed if the damping factor is known, but this factor is rarely known with any degree of certainty. Damping depends on the effectiveness of the rubbing of part-span shrouds and in the attachment. The damping factor for blades of similar designs has been measured using the standard technique of measuring displacements in blade as a function of frequency and dividing the width of the highest displacement peak at  $\sqrt{2}/2$  of peak maximum by the frequency, which for a typical blade gives  $D$  (damping)  $\approx 0.005$ , or an amplification factor ( $Q$ ) of  $\approx 100$ . The disk attachment loads thus computed are shown in **Table 2**.

The loads given in Table 2 are not the same on both sides of the attachment because the blade is being loaded by the gas stream in one direction only. Thus, the loads in the attachment due to blade resonance are as shown in Fig. 14.

**Table 2**  
Disk attachment loads at the engine speed shown

Type of loading	Magnitude (lbs)	
	10400 rpm (blade resonance)	7000 rpm (non resonance)
Centrifugal - normal	10100	7600
Centrifugal - shear	5000	2000
Gas - normal (static)	2200	1480
Gas - shear (static)	1100	740
Gas -normal (dynamic)	$\pm 3200$	$\pm 32$
Gas - shear (dynamic)	$\pm 1600$	$\pm 16$

## DISCUSSION

Imagine the engines of an aircraft being started and the aircraft being taxied to the end of the runway where full power is generated as the aircraft lifts off. The analysis shows, Fig. 6, that when the turbine speed increases from 0 to 10400 rpm in one of the the fan stages, the static normal force on the blade-disk attachment ( $F_n^S$ ) increases to about 6800 lbs., but can increase further to 10100 lbs. with vibration. The static shear force ( $F_s^S$ ) increases to 8000 lbs., relaxing to about 5000 lbs. as the normal force increases. A static friction coefficient of 0.5 was assumed.

Now imagine that the aircraft makes a sharp turn that causes the intake air flow to the turbine to have the profile assumed in Fig. 10, and that blade resonance occurs, with minimal damping, at about 1 kHz. The combined loading on the attachment from centrifugal and blade resonance is shown in Fig. 14, where loads on the two sides of the attachment are seen to be different. The analysis predicts that the highest normal force ( $F_n$ ) could be  $12300 \pm 3200$  lbs. with the highest shear force ( $F_s$ ) of 6100

$\pm 1600$  lbs., when a friction coefficient of 0.5 is assumed.

With the engine at maximum turbine power, the aircraft has now reached the planned altitude, and the engine speed is decreased from 10400 rpm to 7000 rpm, the cruise speed. This decrease in turbine speed causes the static normal force ( $F_n^S$ ) on the blade-disk attachment first to increase to about 12000 lbs, and the shear force ( $F_s^S$ ) to 5400 lbs., then to decrease as blade slippage occurs, to the values shown in Table 2. Blade resonance should not occur at this speed, according to the assumptions, so the resulting normal and shear forces are shown in **Fig. 15**.

These analyses indicate that blade resonance can generate static and dynamic forces on the blade-disk attachment that are a significant fraction of the static loads caused by centrifugal force. For the worst case considered here, the dynamic normal loads could be  $\pm 0.41$  of the static normal load, and the dynamic shear could be  $\pm 0.26$  of the static shear load. Cyclic loads are applied with a relatively large mean loads. For the case illustrated, the static shear load was 6100 lbs. with a cyclic load of  $\pm 1600$  lbs. In terms of materials testing under fatigue loading, this means that for shear loading,  $R = 0.6$  ( $R$  ratio = min. load/max. load) is appropriate, while for the normal forces  $0.42 < R < 0.59$ .

## CONCLUSIONS

1. Centrifugal loads on the blade-disk attachment cause the lugs to dilate as speed increases, which allows the blades to slide out of the lug. Conversely, as rotational speed decreases, the lugs contract forcing the blade to slide in the opposite direction.
2. The magnitude of blade motion within the disk is 50 to 100  $\mu\text{m}$ .
3. The highest centrifugal forces are exerted on the attachment when turbine speed is being reduced.
4. Centrifugal forces on the blade-disk attachment can be as high as a normal force of 10100 lbs., with a shear force of 5000 lbs.
5. Under conditions that lead to blade resonance, the attachment normal force can be as high as high as  $12300 \pm 3200$  lbs., with a shear force of  $6100 \pm 3200$  lbs.



**ACKNOWLEDGEMENTS**

This analysis was conducted under Contract F49620-95-C-0037 from Air Force Office of Scientific Research. Discussions with Mr. Greg Massari of the turbine engine repair facility at Kelly Air Force Base were very helpful.

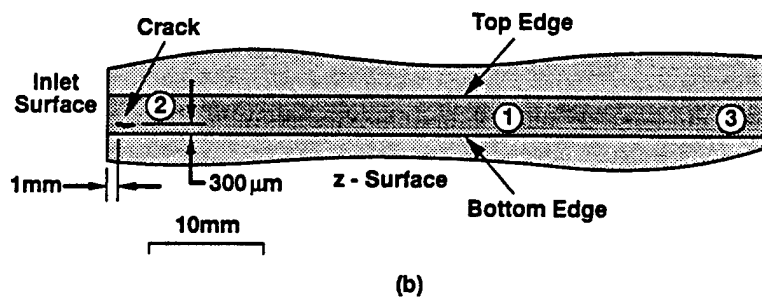
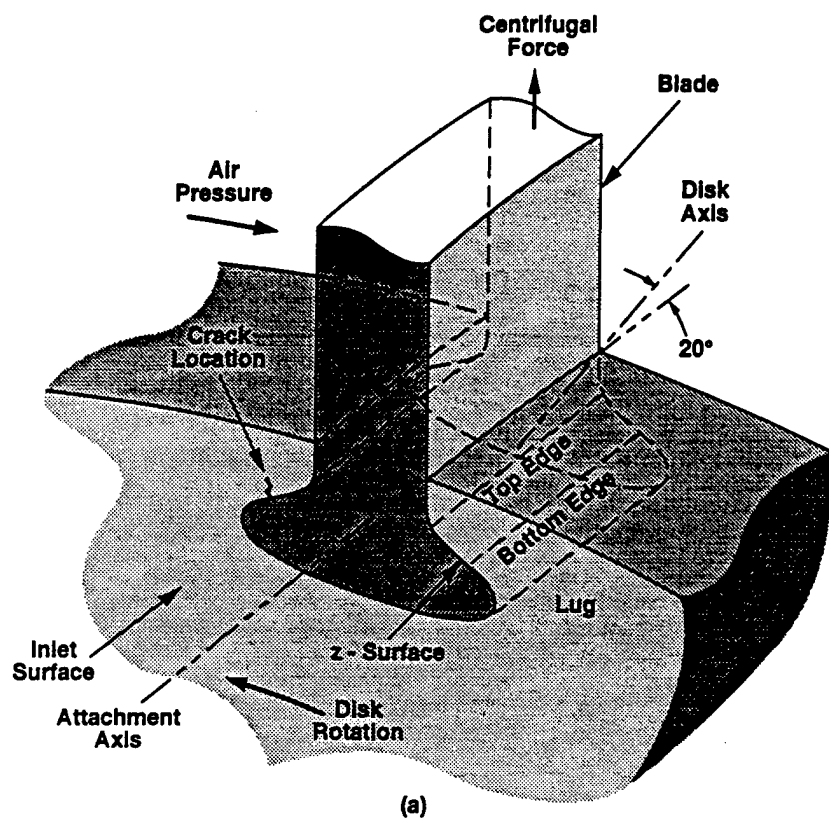


Fig. 1 Drawings of (a) blade/disk attachment portion of the disk, and (b) the attachment surface showing the location of cracking and typical dimensions of an attachment.

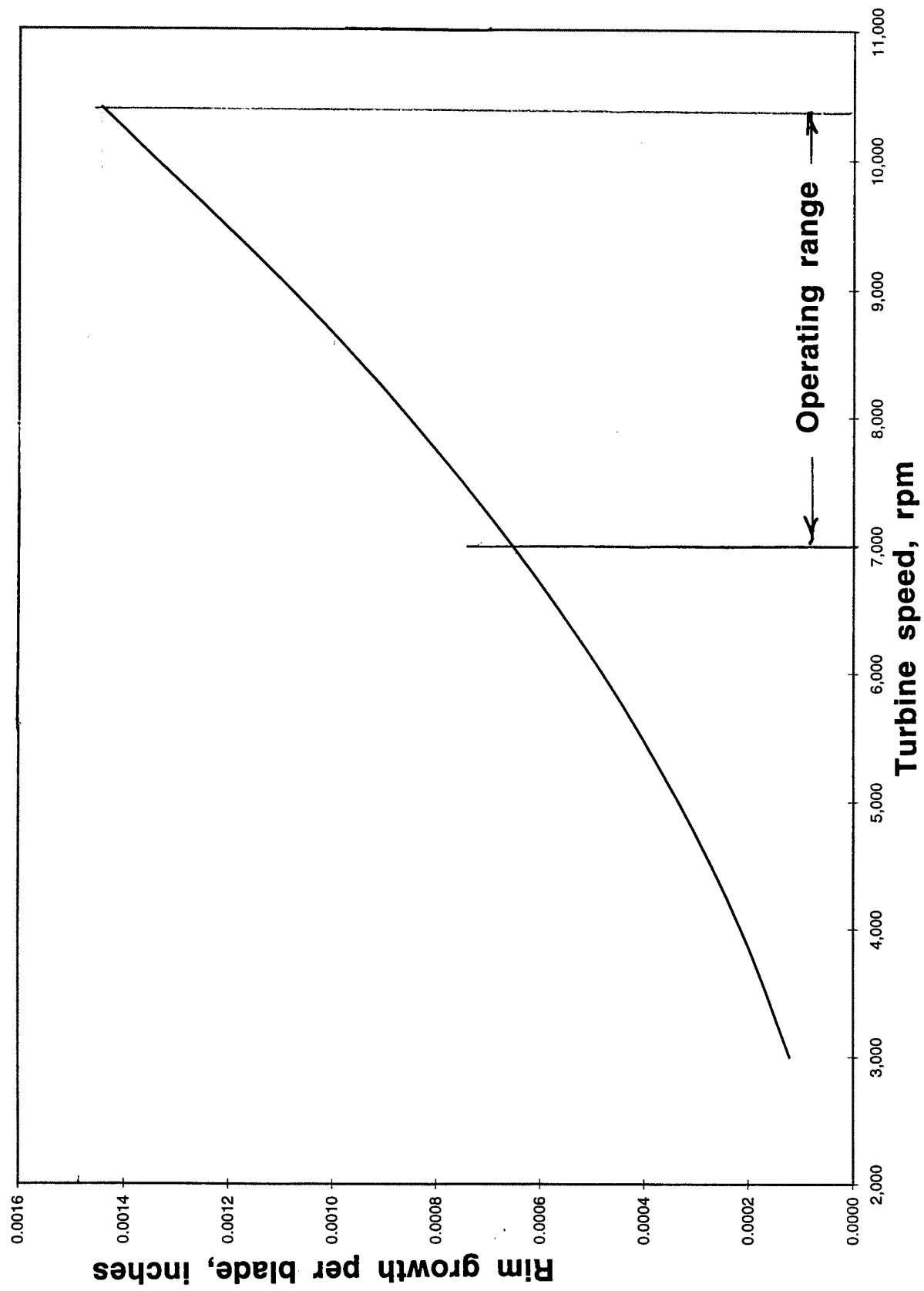


Fig. 2 Increases in slot width caused by turbine speed change.

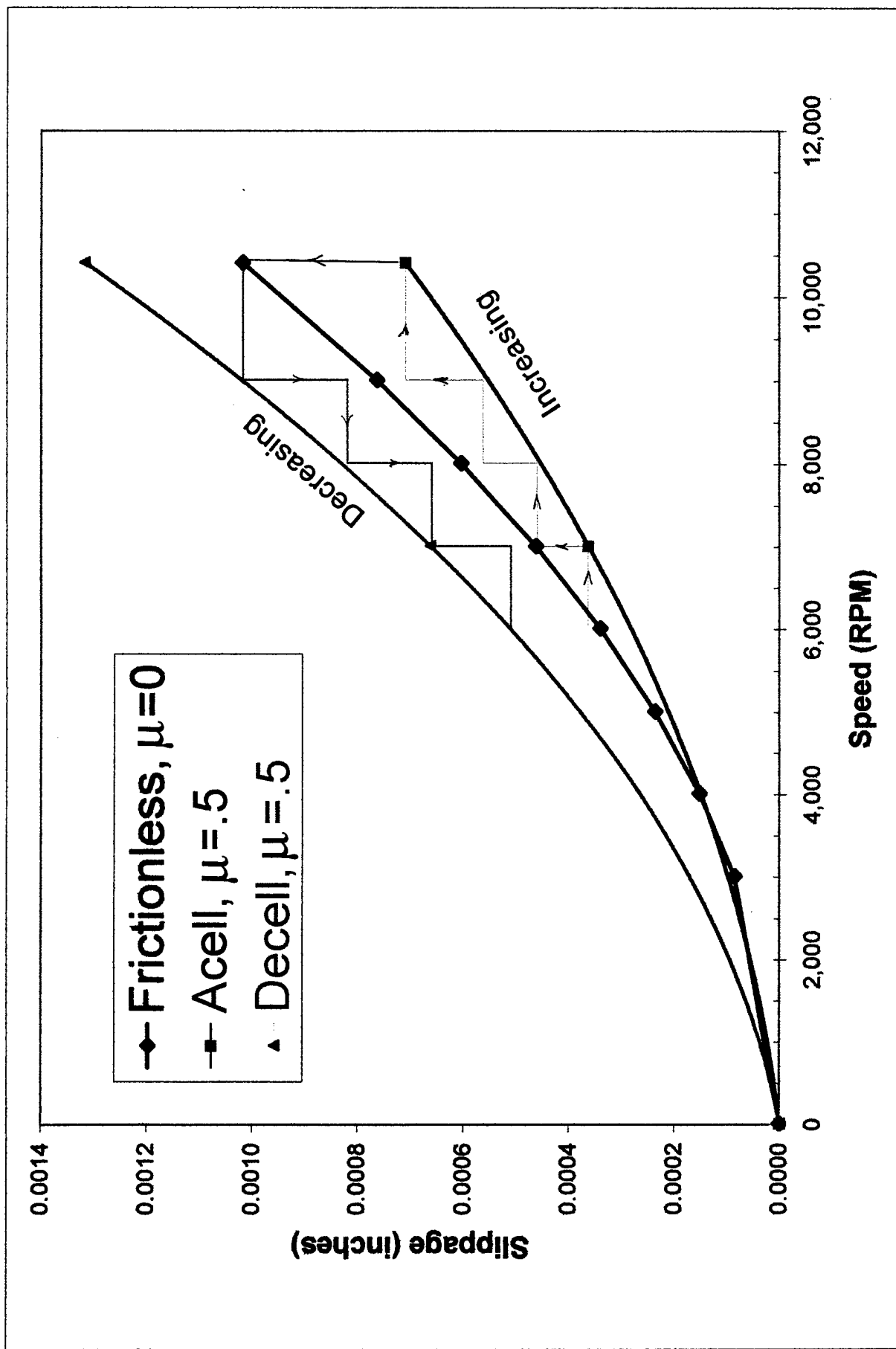


Fig. 3 Slippage of the blade within the disk for  $\mu = 0$  and  $\mu = 0.5$  under accelerating and decelerating engine speeds. Lines with arrows indicate the stick-slip condition as the blade moves within the attachment.

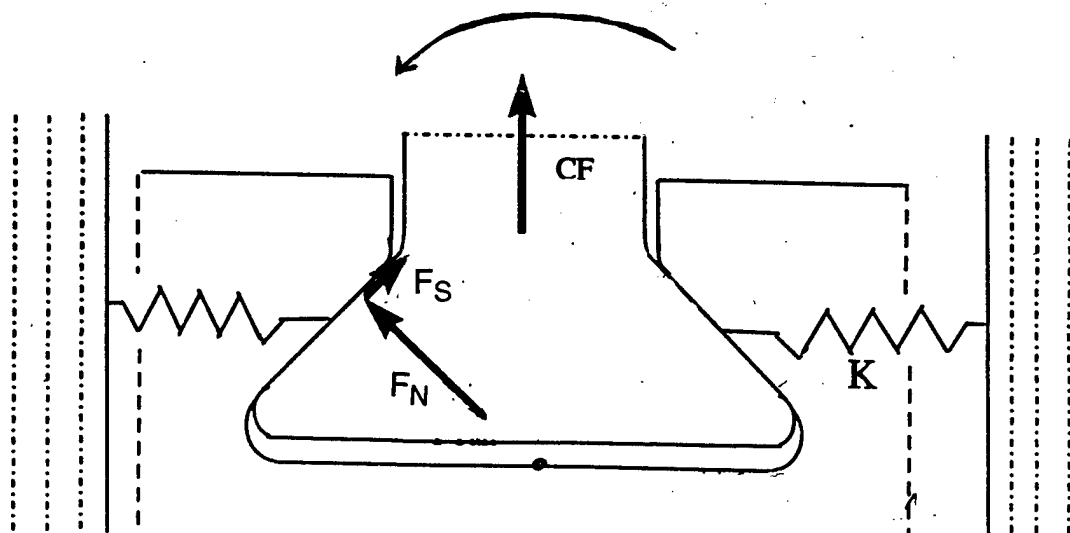


Fig. 4 Attachment slot with normal and shear forces ( $F_N$  and  $F_S$ ) on the attachment defined. The centrifugal force on the blade is  $CF$  and the spring constant  $K$  representing lug deformation are shown also.

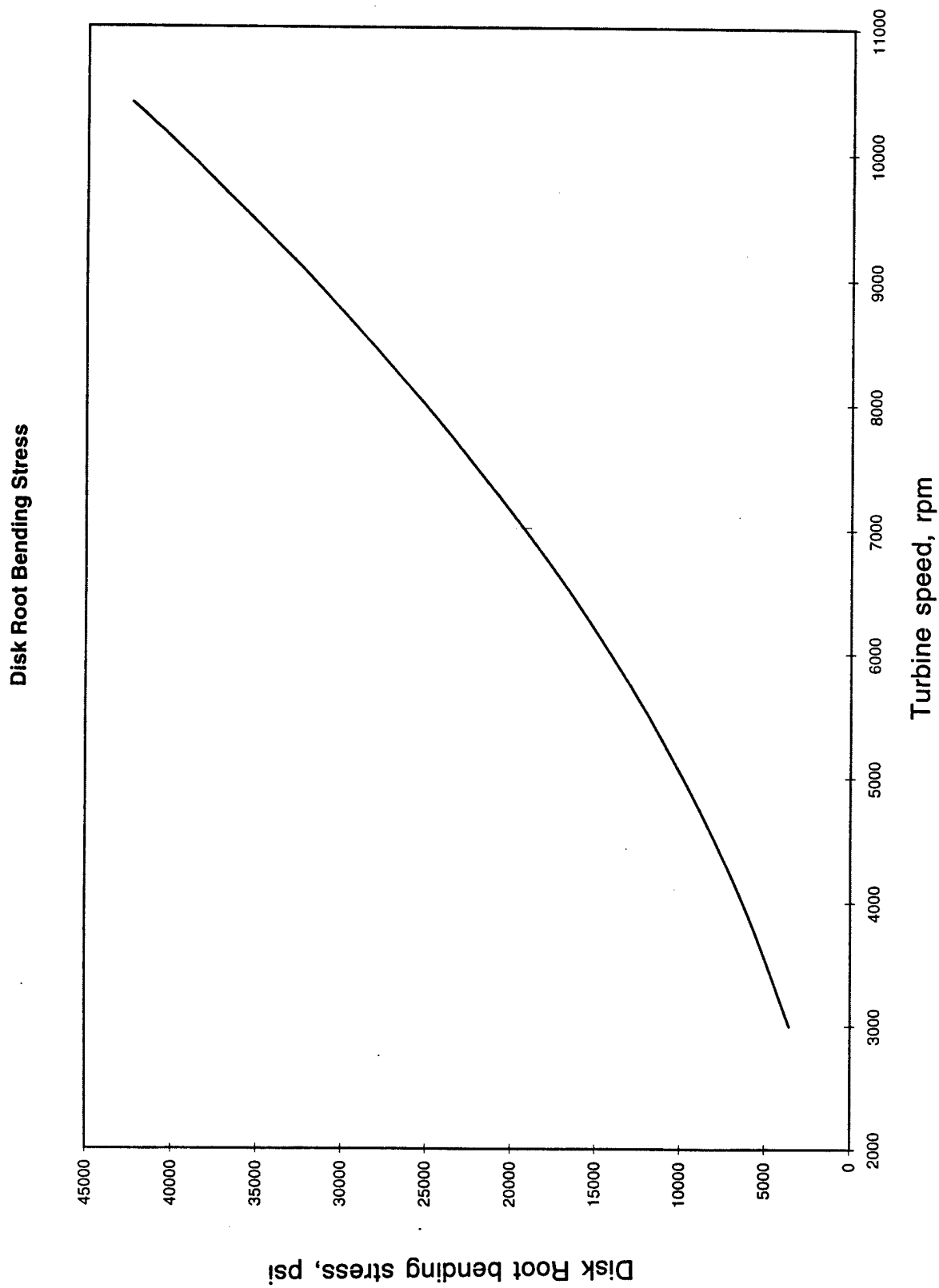


Fig. 5 Bending stress at disk root as a function of turbine speed.

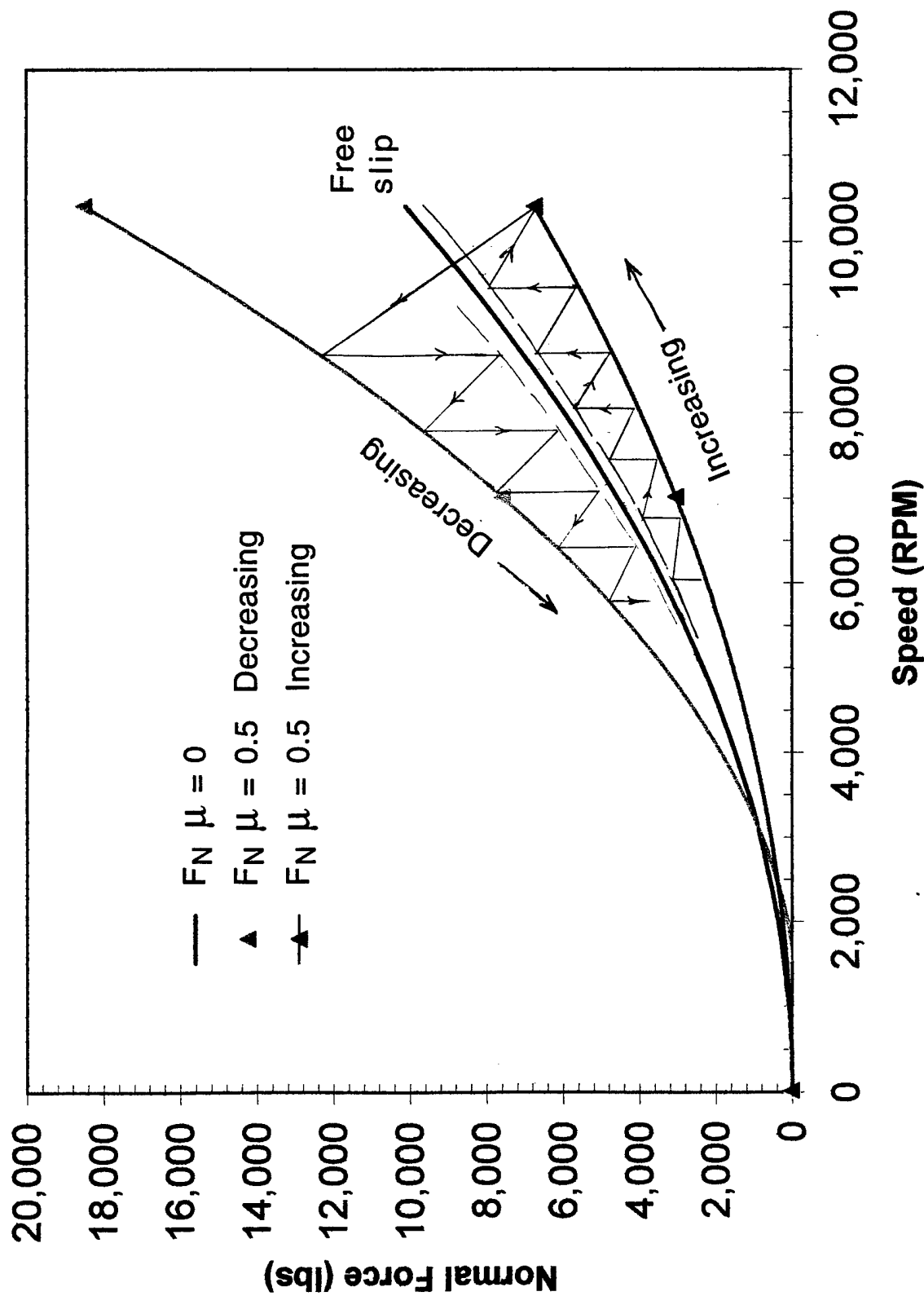


Fig. 6 Force normal ( $F_N$ ) to the attachment surface of the disk due to increases and decrease in engine speed for  $\mu = 0$  (free slip) and  $\mu = 0.5$ . Dashed lines represent dynamic friction. Lines with arrows indicate the stick-slip condition as the blade moves within the attachment.

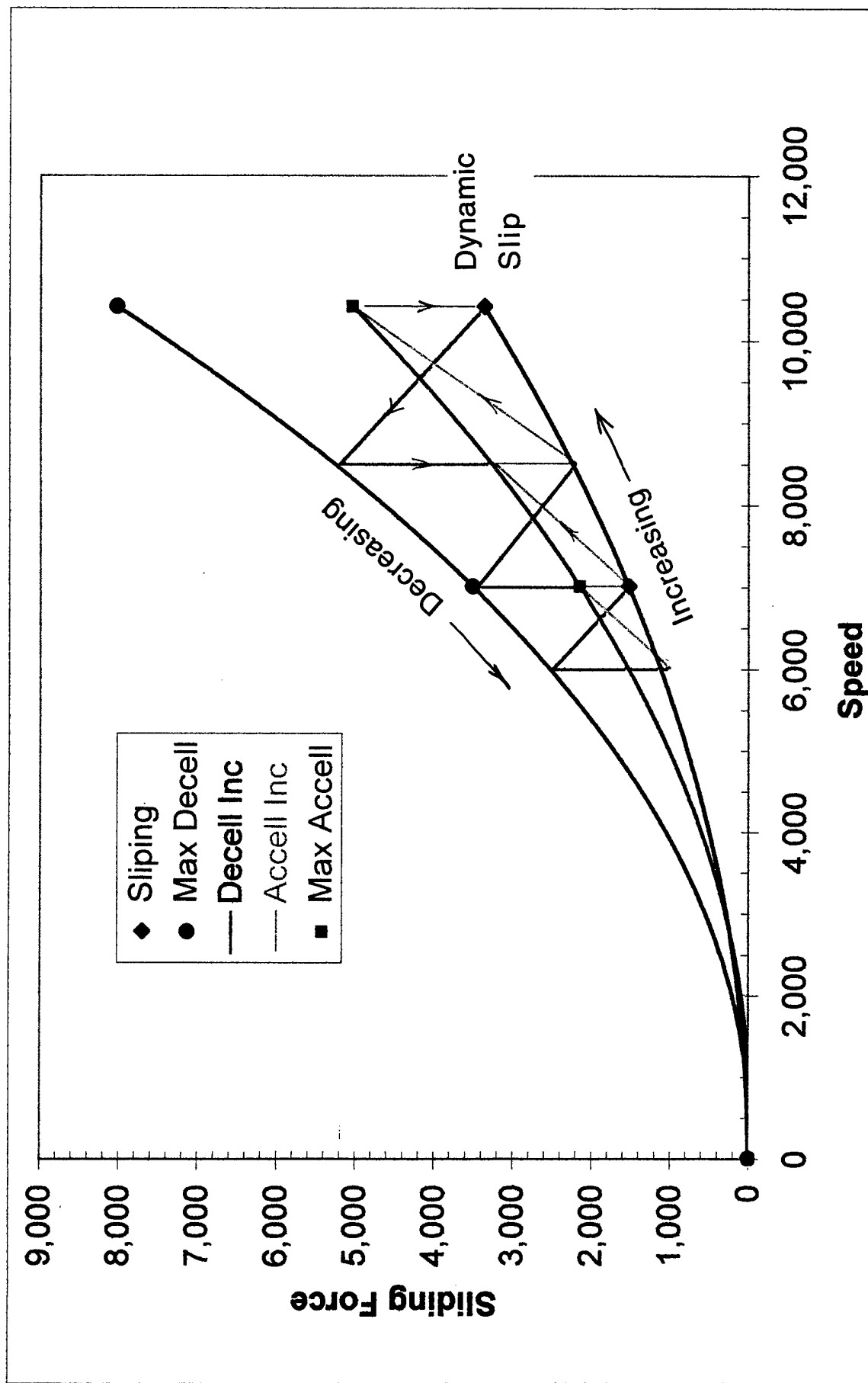


Fig. 7 Shear force ( $F_s$ ) on the attachment surface of the disk due to increase and decrease in engine speed for  $\mu = 0.5$  and dynamic friction. Lines with arrows indicate the stick-slip condition as the blade moves within the attachment.



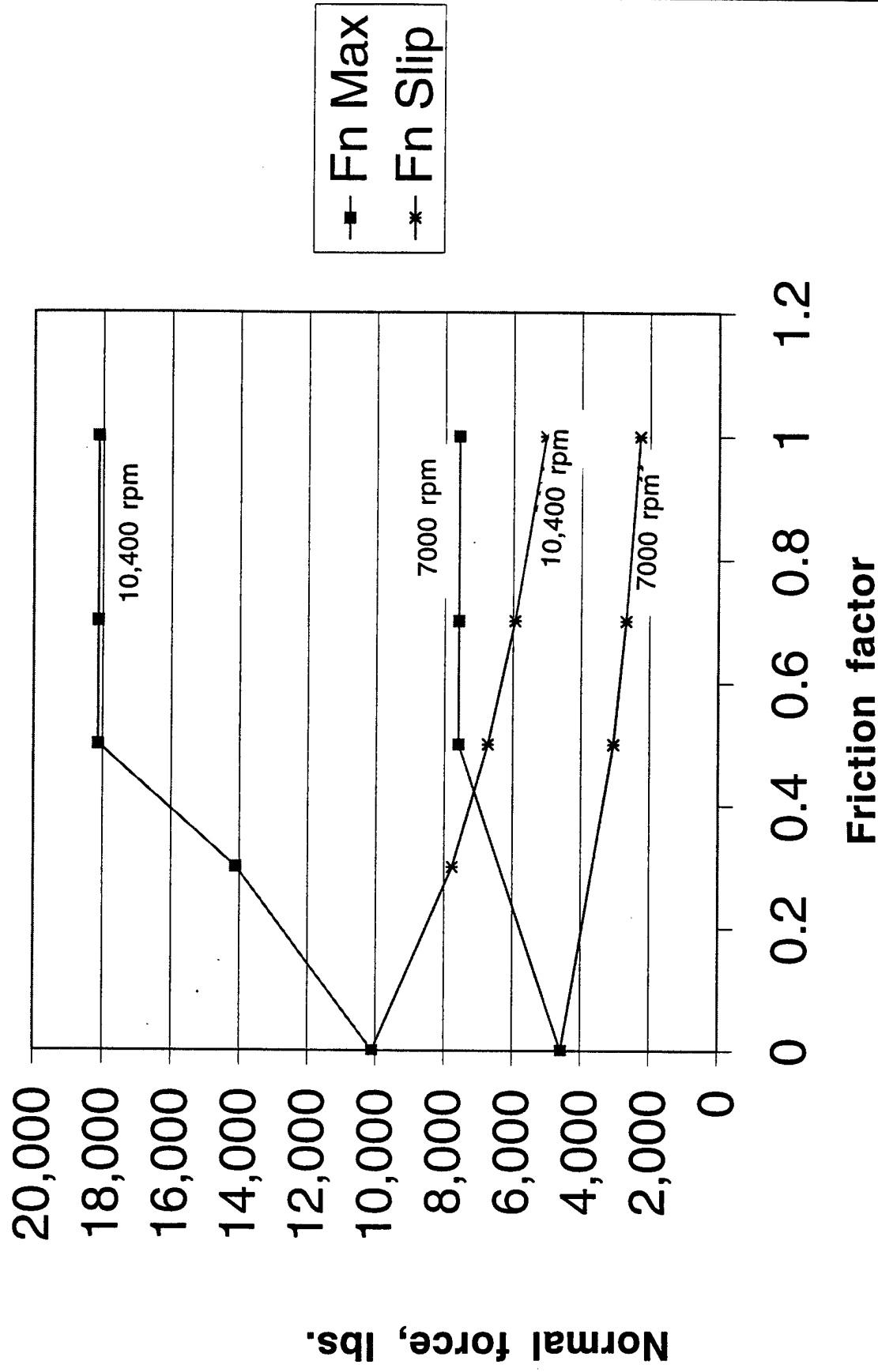


Fig. 8 The effect of friction coefficient on attachment normal force (Fn) at 7000 and 10400 rpm, as compared to the freely slipping condition (lower lines).

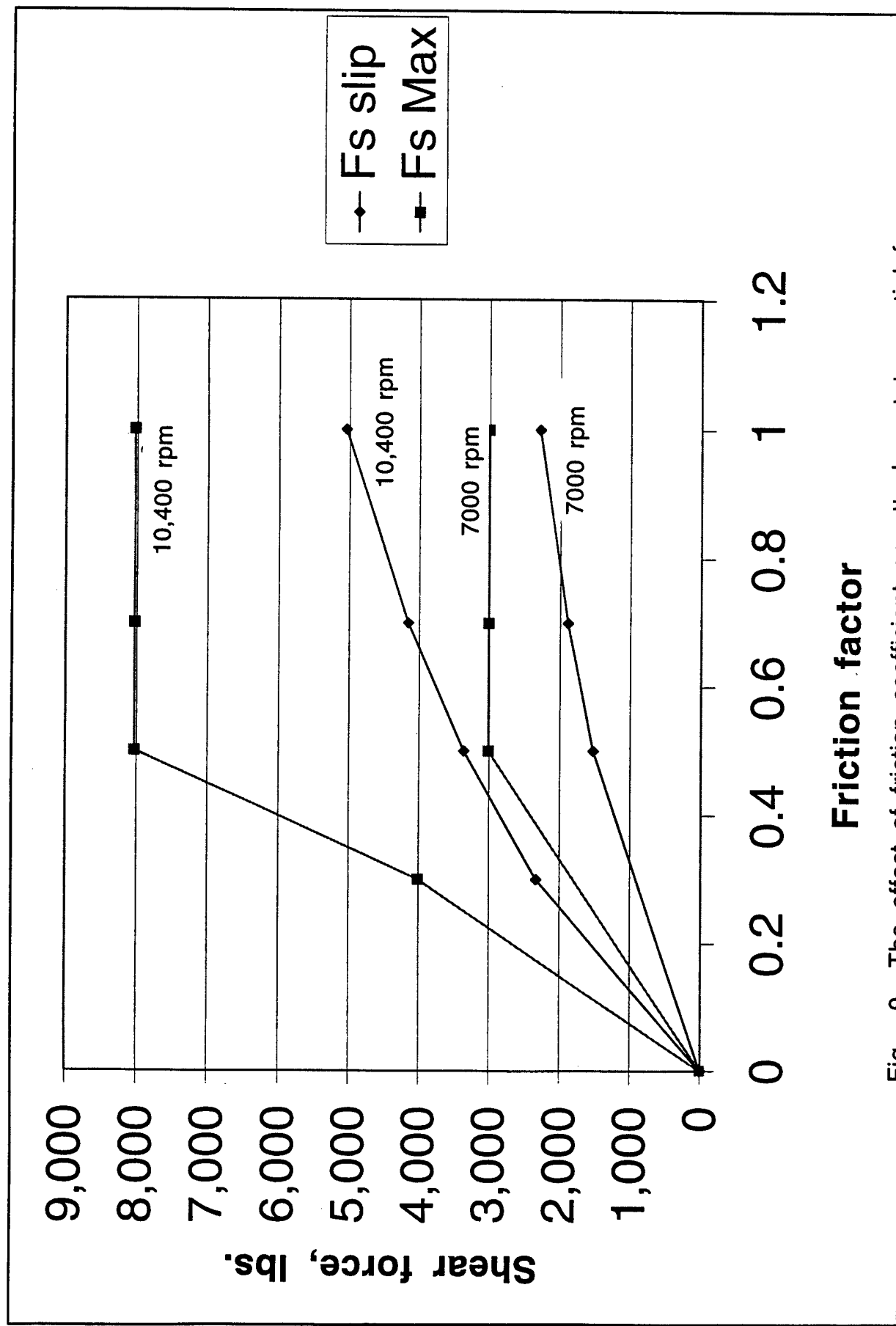


Fig. 9 The effect of friction coefficient on attachment tangential force (Fs) at 7000 and 10400 rpm, as compared to the freely slipping condition (lower lines).

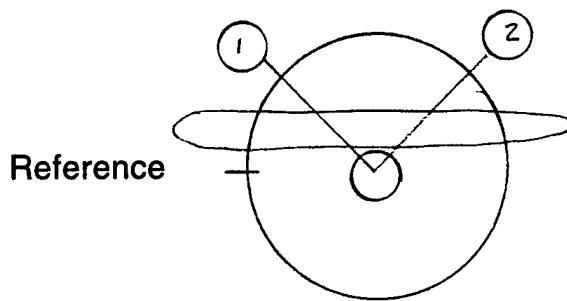


Fig. 10 View of the turbine engine inlet showing the region where the pressure has been lowered. Reference location is shown.

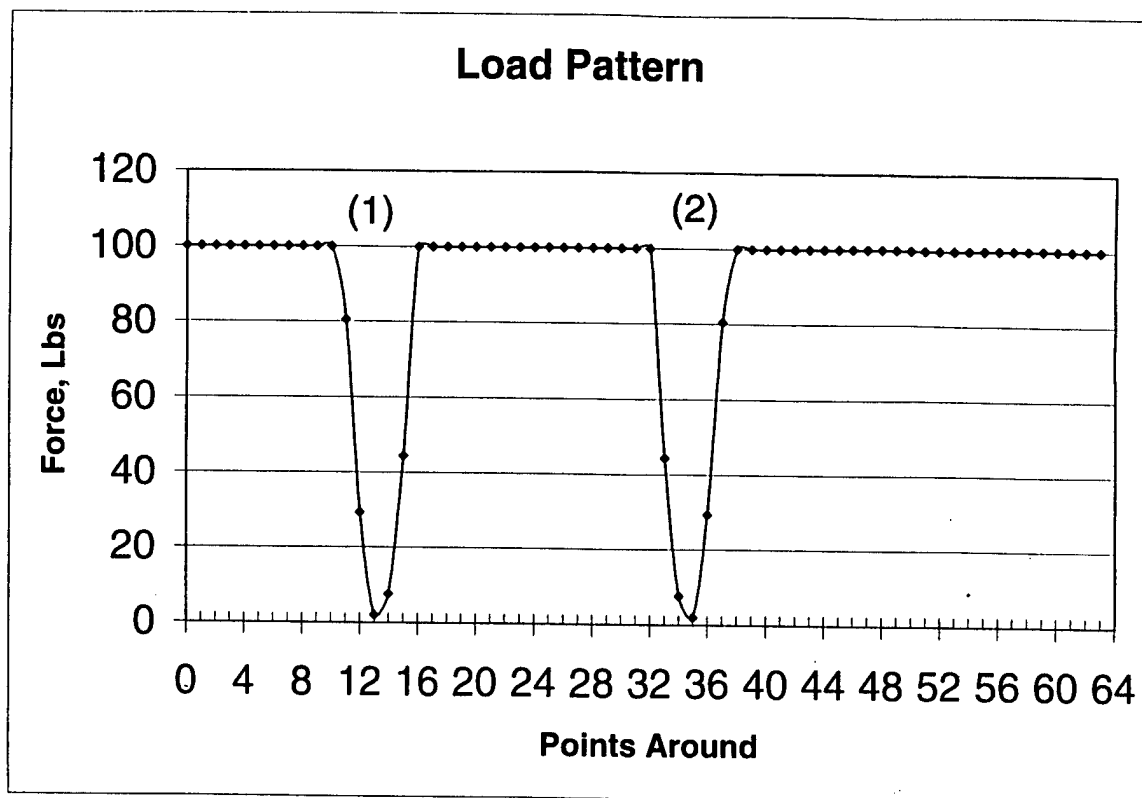


Fig. 11 Force on a blade due to loading by the gas stream as a function of the angular position in the engine relative to the reference. Blade loading due to perturbation of the gas stream has been assumed to drop to nearly zero at locations 1 and 2 and to be uniform elsewhere.

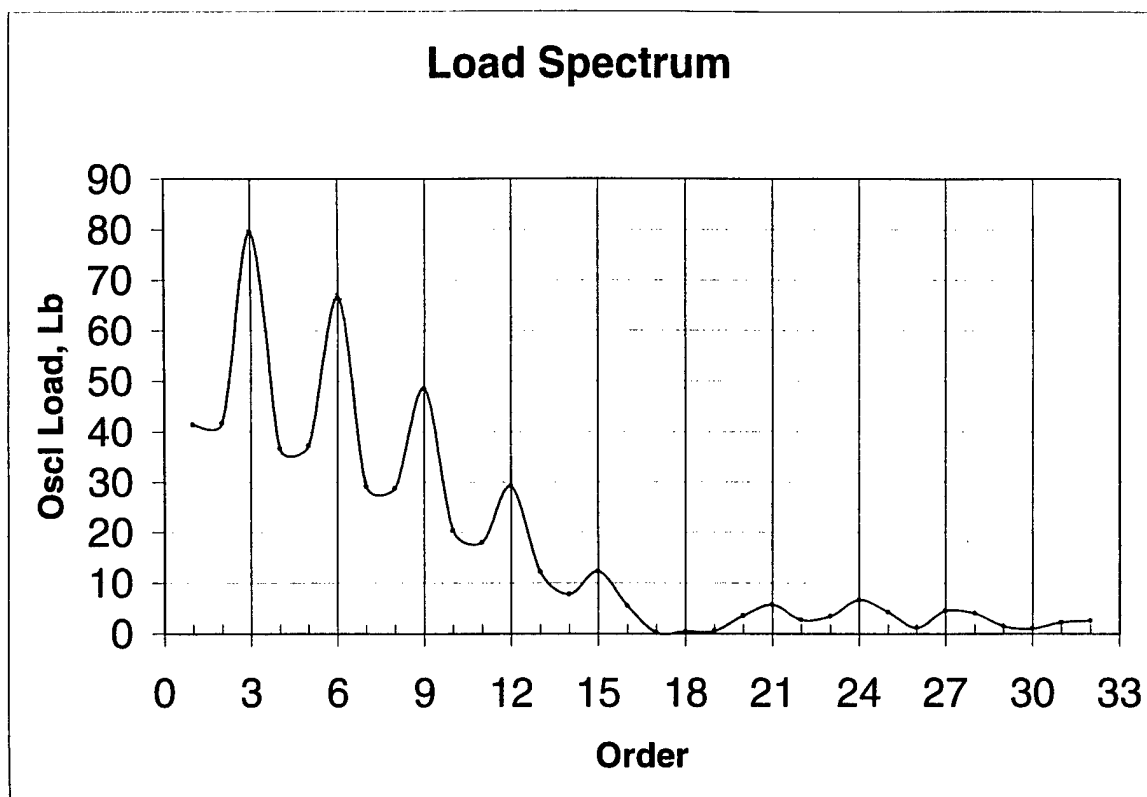


Fig. 12 Fourier transform of the blade loading shown in Fig. 12. The magnitude of the loading is shown as a function excitation order.

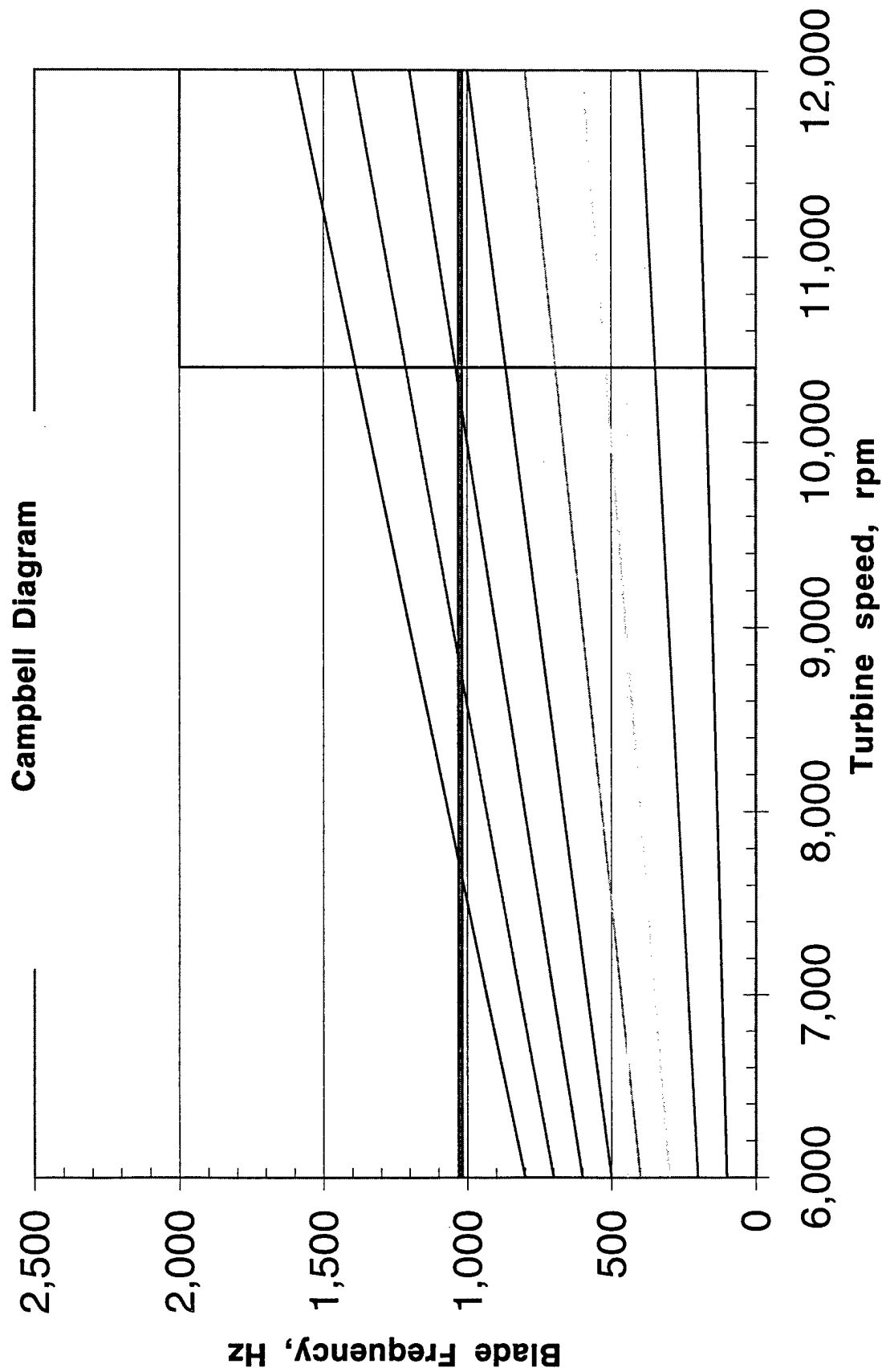


Fig. 13 Blade vibration frequency as a function of engine speed. Each line shown is a multiple of the fundamental blade vibration. At 10400 rpm, the sixth order vibration is about 1 kHz.

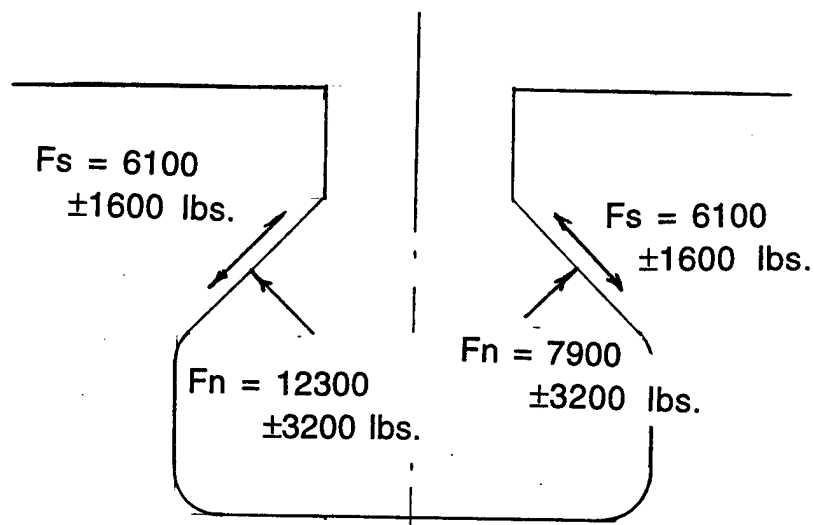


Fig. 14 Combined static and dynamic loads at 10400 rpm due to centrifugal and gas flow loadings, and the cyclic loading due to blade resonance.

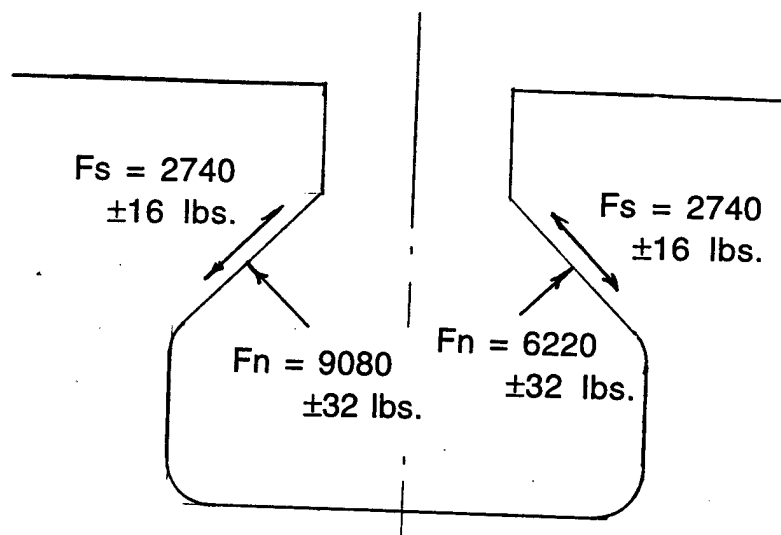


Fig. 15 Combined forces on the attachment after turbine speed is decreased from 10400 to 7000 rpm.

## FOREIGN OBJECT DAMAGE

An experiment was conducted on one specimen that had simulated foreign object damage (FOD). The specimen was designed to be blade-like, in that it was thin in cross-section (1 x 12.7 mm) and each side had an edge that tapered at 45°. The simulated FOD were two damage sites caused by impact of a steel sphere projected onto the specimen at a velocity of about 500 m/sec. using a gas gun at the University of Dayton Research Institute.

The angle between the projectile path and blade plane was 90° for one impact and 45° for the other. The 90° path resulted in removal of a piece of the edge of the specimen that resembled actual FOD found on many turbine blades in service. The 45° path resulted in a large bulge in the edge that had a small tear from one end of the bulge. These damage sites resulting from these impacts are shown in **Fig. 1**.

This specimen was cycled at stress levels that, according to analysis, should have resulted in crack initiation and arrest due to a notch effect. The basis of the analysis was a fatigue limit stress defined at 10 million cycles; thus, the specimen was cycled to 10 million cycles at each stress level.

No crack initiation or growth was observed after cycling at 4 stress levels, as shown in **Fig. 2**.

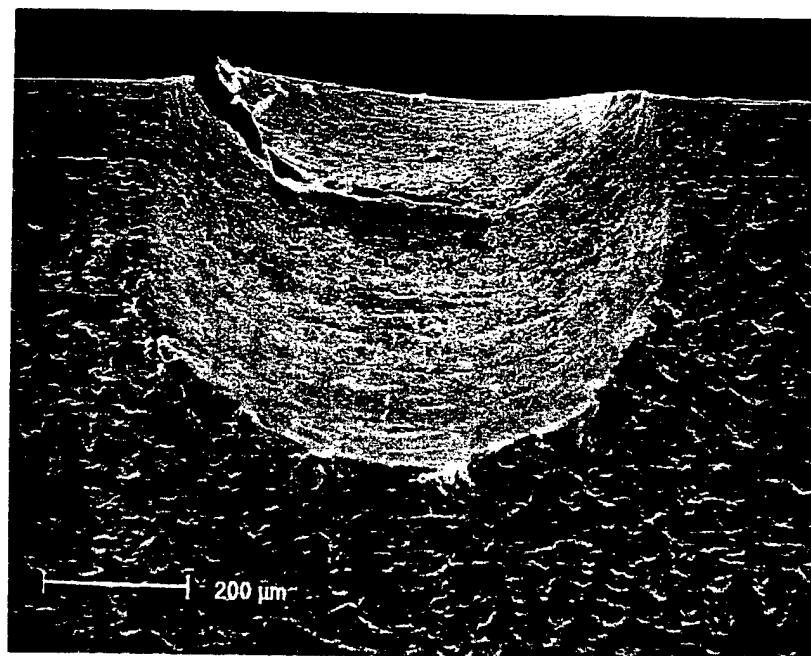
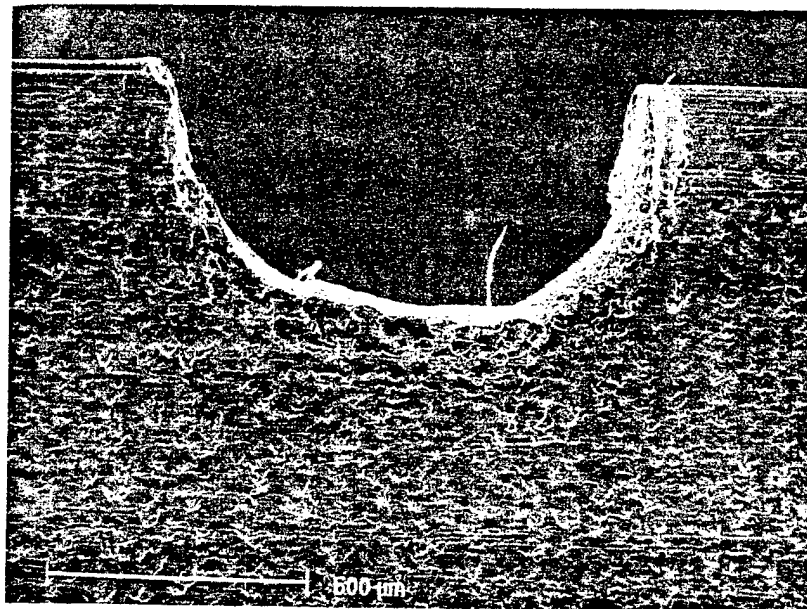


Fig. 1 Simulated Foreign Object Damage (FOD). A steel sphere approximately 0.7 mm in diameter was projected on the edge of a blade-like specimen at a velocity of 500 m/sec. at two sites. The specimen was 1 mm thick and the angle between the two faces at the edge was 45°. Top photograph: FOD shown was the result of a projectile trajectory 90° to the plane of the specimen. Lower photograph: FOD shown was the result of a projectile trajectory 45° to the plane of the specimen.



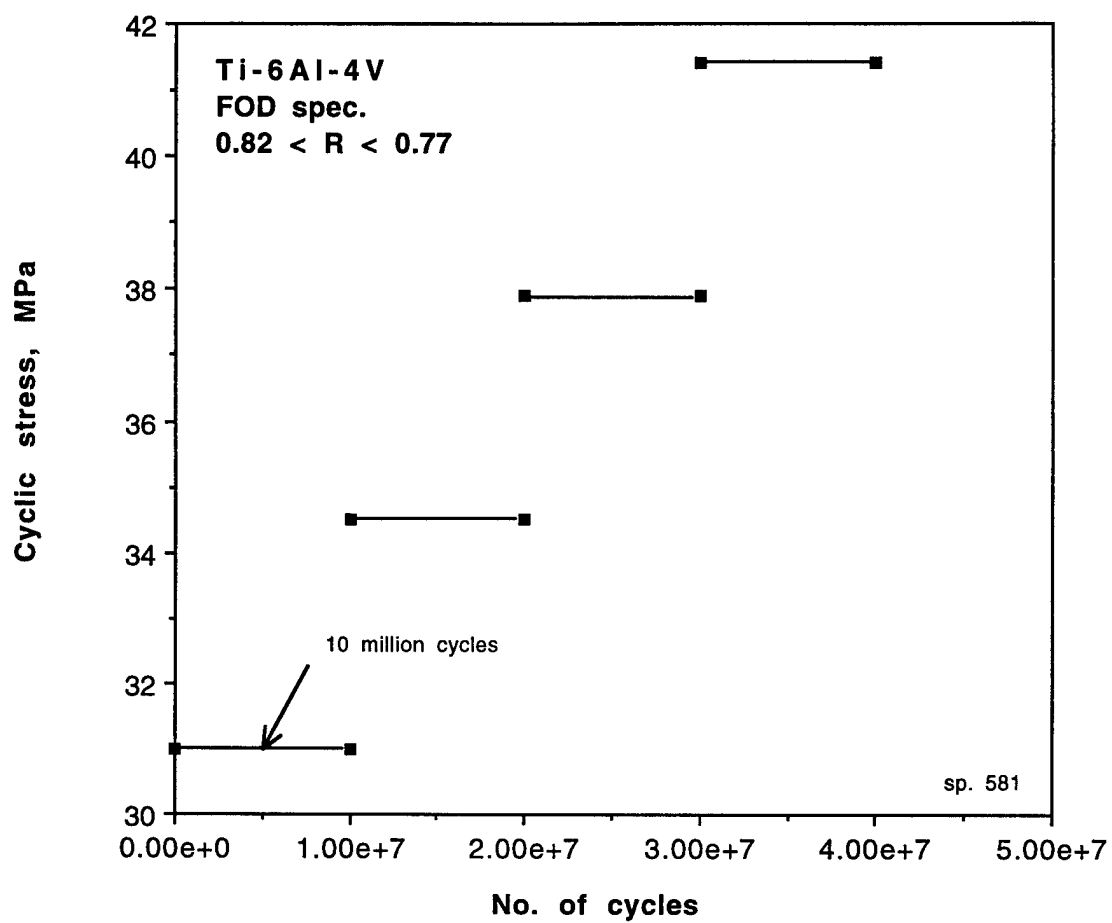


Fig. 2 Stress history for Foreign Object Damaged Specimen. No crack initiated during this experiment.

## CONCLUSIONS

Collaboration with the MURI program on High Cycle Fatigue was successful. Two students spent 10 days each at Southwest Research Institute using the 1.5 kHz SEM fatigue machine. Three MURI meetings were attended by the PI where data were presented and information was disseminated.

The SwRI Independent Research Program was successful, as measured by the number of topics pursued and the results obtained. The work done at SwRI complements research performed within the MURI and Industry High Cycle Fatigue Programs. Some specific conclusions from the Independent Program are as follows:

1. Fatigue crack growth through Ti-6Al-4V is about a thousand times faster in air than in vacuum for the alpha-beta microstructure.
2. The threshold for fatigue crack growth,  $\Delta K_{th}$ , for Ti-6Al-4V appears to be only slightly affected, if at all, by environment: vacuum vs. air.
3. For the Ti-6Al-4V with a slowly cooled, fully lamellar microstructure, fatigue crack growth was much slower, perhaps as much as 0.01 times, in both vacuum and in air, as compared to the alpha + beta microstructure.
4. Fatigue striation spacings found on fractured alpha facets of Ti-6Al-4V with the alpha-beta microstructure grown in vacuum were very small, approximately 50 nm, which is smaller than the known subgrain size for this microstructure.
5. Near  $\Delta K_{th}$ , approximately 40,000 loading cycles were required to produce one increment of crack growth (fatigue striation) through the alpha-beta Ti-6Al-4V microstructure.
6. Fatigue cracks growth (HCF), with periodic unloading from high mean stress (LCF), can slightly increase or decrease crack growth rates, depending on  $\Delta K$ .
7. Crack tip micromechanics measurements during HCF/LCF indicate that any effect of the LCF cycle would be expected over only a small number of cycles, and that the effect would be minimal. These

measurements agreed with the effect of LCF on measured crack growth rates.

8. For crack growth in air through Ti-6Al-4V with the alpha-beta microstructure, agreement in  $da/dN-\Delta K$  curves was found between 5 investigators using frequencies between 30 Hz and 20 kHz. Good agreement was found also at  $R \approx 0.85$  for  $\Delta K_{th} = 2.4 \pm 0.1 \text{ MPa}\sqrt{\text{m}}$  amongst these investigators.

9. An analysis was made that used a fretting fatigue model derived at MIT together with the geometric details of a crack found in the blade containment lug of an aeroengine fan disk. The crack initiated and grew at an angle to the surface. The model indicated that angled crack growth was under LCF, but probably grew under HCF once it turned to a perpendicular direction to the attachment surface. Fractography indicated, not conclusively, that all crack growth was LCF.

## **APPENDIX**

A description of experiments conducted using the 1.5 kHz SEM high cycle fatigue equipment is listed in this section. The Specimen Log gives the specimen number, dates of the experiment, a brief description of the conditions used, and some results. This log provides a key to more complete results in project files.

## HCF Specimen Log

Specimen number	Dates of experiment	Description of experiment/result
542	4 Jun 1997	EDM notch 790 $\mu\text{m}$ . Mean load = 3000 lbs.; cyclic load = $\pm 687$ lbs. Crack init. and grew to $2a \approx 3$ mm in 191,969 cycles.
543	13 Jun 1997	EDM notch 400 $\mu\text{m}$ . HCF+LCF resulted in faster crack growth than HCF alone. Replicas used to follow crack growth.
544	26 Jun 1997	10X microscope used to follow crack growth. Double edge notch, through crack configuration. Crack growth rates match Rockwell data at same R. $\Delta K_{th} = 2.62 \pm 0.15 \text{ MPa}\sqrt{\text{m}}$ .
547	Jul - Aug 1997	EDM notch 200 $\mu\text{m}$ in diameter and depth. Replicas used to follow cracks. Crack initiated after 18.36 m cycles on one side of notch. Mean load = 3000 lbs; cyclic load = $\pm 400$ lbs.
560	Sep 1997	EDM notch = 76 $\mu\text{m}$ dia. and deep. Cycled in air 11.69 m cycles before strain gage failed. With new gage, cycled $\approx 2$ m cycles in air until specimen broke in grips due to fretting. No crack at notch.
561	Sep 1997	EDM notch = 200 $\mu\text{m}$ dia. and deep. Crack initiated from scratch on radius blend; discovered after 3 m cycles. Decided to initiate future cracks in bending.
366	4 Dec 1997	Fretting experiment, air. Pad removed after 2 m cycles, no fretting. Spec. broke after 3.426 m cycles from galling-induced crack initiation.
566	23 Dec 1997 21 Jan 1998	Vacuum, HCF/LCF; analysis Sets 1187-1194. Increased crack growth due to LCF detected.

- 567    28 Jan -            HCF/LCF in vacuum; analysis Set 1195.  
        16 Feb 1998        Increased crack growth rates due to LCF were  
                              not detected in all cases; sometimes growth rates  
        were less and, sometimes greater. Similar conditions to Sp. 566 were  
        used. HCF/LCF interaction results may depend on crack length and  
        microstructural influences.
- 571    24 Feb -            HCF/LCF in vacuum,  $0.6 < R < 0.9$ ; analysis Sets  
        5 Mar 1998        1203-1226.  $\Delta K_{th} = 2.77 \text{ MPa}\sqrt{\text{m}}$ ; Compare with  
                               $\Delta K_{th} = 2.62 \pm 0.15 \text{ MPa}\sqrt{\text{m}}$  for Sp. 544 in air, and  
        with data from UC Berkeley,  $\Delta K_{th} = 2.48 \text{ MPa}\sqrt{\text{m}}$ . Crack growth data in  
        vacuum found to be 1000 times less than in air, but threshold was the  
        same in both.
- 575    16-21 Apr           EDM notch =  $250 \mu\text{m}$  in diameter. Crack initiated  
        1998                in bending. Difficulty growing crack in vacuum  
                              so went to air; specimen broke after 250,000  
        cycles in air. This number of cycles to failure was in agreement with the  
        crack growth rates measured at UC Berkeley at 1 kHz.
- 576    22-27 Apr           EDM notch =  $236 \mu\text{m}$ . Crack init. in bending. In  
        1998                SEM, the crack was grown in vacuum, then in air.  
                              Growth data were obtained, then specimen was  
        removed and etched. After reinstallation, it failed after about 500,000  
        cycles at a relatively high mean stress ( $470 \text{ MPa}$ ) used to induce crack  
        growth due to fretting in the grips. No analyzable images were obtained.
- 574    8 May and            Small crack specimen. Crack initiated from  
        14 June 1998         $30 \times 5 \times 30 \mu\text{m}$  deep FIB notch after a total of  
                              334,000 cycles; the last 2000 was at  $897 \text{ MPa}$ ,  
        which is above the approximate yield stress of  $830 \text{ MPa}$ , and the previous  
        10,000 cycles had been at  $870 \text{ MPa}$ . Cracks grew from each end of notch,  
        plus an extra crack initiated naturally in several contiguous alpha grains  
        near one end of the notch. In the SEM stage, the specimen was cycled 1.1  
        m cycles in vacuum and 1.2 m cycles in air with no crack growth. Loading  
        was below previously measured  $\Delta K_{th} = 2.77 \text{ MPa}\sqrt{\text{m}}$ . The experiment  
        stopped to modify the specimen. Area of cross-section reduced at Metal  
        Samples Co., where the machinist, despite warnings, destroyed the  
        surface containing the cracks. Examination showed that the crack  
        remained, so the specimen surface was repolished and etched, and the  
        experiment continued.

578    20 May 1998    Large beta grain specimen. Notch 475  $\mu\text{m}$ . In bending, a crack 127  $\mu\text{m}$  long appeared from the N end of notch after 20 kcy at 450 MPa. After an additional 9.5 kcy at 430 MPa, and in  $\Delta N = 2$  kcy, the crack grew to 175  $\mu\text{m}$ . After an additional 31 kcy ( $N_{\text{total}} = 62.5$  kcy), the crack was still 175  $\mu\text{m}$  long. An additional 5 kcy at 430 MPa produced a crack 413 on N end and 813 on S end, total  $2a = 1.701$  mm. In the SEM stage, cycled 8.2 mcy in vacuum  $275 < \text{mean stress} < 385$  MPa, 110 cyclic stress  $< 165$  MPa for 6.4  $\mu\text{m}$  total growth; switched to air and cycled 180 kcy at the same load level before 22  $\mu\text{m}$  of growth occurred. Lost loading capacity in machine, so the experiment was suspended.

581    2 - 11 Jun    FOD specimen. Two FOD were introduced at UDRI  
1998                dynamic facility. Design of the experiment was  
                     based on the analysis of Hudak and Chell, with an  
endurance limit at 10 million cycles. The specimen was cycled in 500 kcy increments and examined for cracking to 10 million cycles at each of 4 cyclic stress levels (31, 35, 38, and 41 MPa), mean stress = 620 MPa,  $R \approx 0.9$ . Most of the cycling was in air with examination by SEM (vacuum) at 400 to 2000X. No cracking was found, and the experiment was suspended after 40 million cycles pending analysis.